

A 3-DIMENSIONAL IN SILICO TEST BED FOR RADIOFREQUENCY ABLATION CATHETER DESIGN EVALUATION AND
OPTIMIZATION

A Thesis
presented to
the Faculty of California Polytechnic State University
San Luis Obispo

In Partial Fulfillment
Of the Requirements for the Degree
Master of Science in Biomedical Engineering

by
Carolyn Teng
June 2019

© 2019

Carolyn Teng

ALL RIGHTS RESERVED

COMMITTEE MEMBERSHIP

TITLE: A 3-Dimensional in Silico Test Bed for Radiofrequency
Ablation Catheter Design Evaluation and Optimization

AUTHOR: Carolyn Teng

DATE SUBMITTED: June 2019

COMMITTEE CHAIR: David Scott Clague, Ph.D.
Professor of Biomedical Engineering
California Polytechnic State University

COMMITTEE MEMBER: Scott Hazelwood, Ph.D.
Professor of Biomedical Engineering
California Polytechnic State University

COMMITTEE MEMBER: James Eason, Ph.D.
Professor of Biomedical Engineering
California Polytechnic State University

ABSTRACT

A 3-Dimensional in Silico Test Bed for Radiofrequency Ablation Catheter Design Evaluation and Optimization

Carolyn Teng

Atrial fibrillation (AF) is the disordered activation of the atrial myocardium, a major cause of thrombogenesis and stroke. Currently, the most effective minimally traumatic treatment for AF is percutaneous catheter ablation to isolate arrhythmogenic areas from the rest of the atrium. The standard *in vitro* evaluation of ablation catheters through lesion studies is a resource intensive effort due to ablation substrate tissue variability and visual measurement methods, necessitating large sample sizes and multiple prototype builds. To address this, a computational test bed for ablation catheter evaluation was built in SolidWorks® using morphology and dimensions of the left atrium and adjacent structures. From this geometry, the physical model was built in COMSOL Multiphysics®, where a combination of laminar fluid flow, electrical currents, and bioheat transfer were used to simulate irrigated radiofrequency (RF) tissue ablation. Simulations in simplified 3D geometries led to lesion sizes within reported ranges from an in-vivo ablation study; however, while the ellipsoid morphologies in the full atrial model were consistent with past lesion studies, there were sizeable differences in lesion sizes. Perpendicularly oriented catheter tips were associated with decreases of -91.3% and -70.0% in lesion depth and max diameter, while tangentially oriented catheter tips produced lesions that were off by -28.4% and +7.9% off for max depth and diameter. Preliminary investigation into the causes of the discrepancy were performed for fluid velocity, contact area, and other factors. Guided by the findings of these studies, suggestions for further investigation are provided to aid in root cause determination of this lesion discrepancy, such that the test bed may be verified for use for other ablation catheter evaluations.

Keywords: Radiofrequency ablation, atrial fibrillation, computational modeling, catheter design.

TABLE OF CONTENTS

	Page
LIST OF TABLES	ix
LIST OF FIGURES	x
CHAPTER	
1. INTRODUCTION	1
1.1. Radiofrequency Catheter Ablation of Atrial Arrhythmias	1
1.2. Medical and Economic Burden of Atrial Fibrillation.....	1
1.3. The Interventional Electrophysiology Device Market	3
1.4. Problem Statement	3
1.4.1. Current Methods of Ablation Catheter Lesion Evaluation	3
1.4.2. The Utility of Computational Models	4
1.4.3. Regulatory Stance on Computational Models	4
1.5. Previous RF Ablation Computational Studies	5
1.5.1. Literature Review	5
1.6. The Proposed Model.....	9
1.6.1. Thesis Aims.....	9
1.7. Summary of Contents.....	9
2. ANATOMY & PHYSIOLOGY OF THE LEFT ATRIUM AND ATRIAL FIBRILLATION.....	11
2.1. Normal Function of the Heart	11
2.2. Etiology of Atrial Fibrillation.....	13
2.2.1. Causes	13
2.2.2. Risk Factors.....	15
2.3. Pathophysiology of Atrial Fibrillation.....	15
2.3.1. Symptoms.....	15
2.3.2. Disease Progression	15
2.3.3. Prognosis.....	16
2.4. Treatments for Atrial Fibrillation	16
2.5. Anatomical Considerations for Atrial Fibrillation Ablation.....	17

2.5.1. Targets for Ablation: Pulmonary Veins	17
2.5.2. Targets for Ablation: Non-Pulmonary Vein Structures.....	18
2.5.3. Transmurality + The Importance of Atrial Wall Thickness	19
2.5.4. Collateral Damage Risks	20
3. BIOPHYSICS OF RADIOFREQUENCY ABLATION	22
3.1. Overview of Relevant Physics	22
3.2. Mathematical Models of Ablation Biophysics	24
3.2.1. Heat Transfer: Pennes' Bioheat Equation	24
3.2.2. Mass Transfer: Navier Stokes	25
3.3. Tissue Viability: The Arrhenius Damage Equation	26
4. MODEL DEVELOPMENT	27
4.1. Modeling the Catheter Tip of the Test Device.....	27
4.2. Physics and Material Properties Verification Through Simplified Models.....	27
4.3. Left Atrial Anatomical Model Geometry.....	30
4.3.1. Left Atrial Anatomic Modeling Approaches.....	30
4.3.2. Critical Anatomic Features of the Left Atrium	30
4.3.3. Left Atrial + Adjacent Structure Dimensions	32
4.3.4. Constructing the Full Left Atrial Model	35
4.4. Physical Model Definition.....	39
4.4.1. Assumptions.....	39
4.4.2. Boundary Conditions.....	39
4.5. Material Properties	42
4.6. Mesh Development	42
4.6.1. Geometry Subdivisions	43
4.6.2. Study Region Convergence.....	44
4.6.3. Element Quality Observations	49
4.7. Time Discretization	51
4.8. FEM Analysis Steps.....	52
4.8.1. Step 1: Stationary Study.....	53

4.8.2. Step 2: Frequency Transient Study	53
4.9. Validation Case Study.....	53
4.10. Damage Evaluation Methods.....	55
5. RESULTS.....	58
5.1. Multiphysics Verification with Simplified Models.....	58
5.2. Initial Simulations + Modification to the Full Atrial Model	61
5.3. Full Atrial Model vs Validation Case Lesion Comparison	62
5.4. Diagnostics to Determine Root Cause of Perpendicular lesion Size Discrepancy.....	65
5.4.1. Flow Velocity Distribution in the Full Atrial Model	65
5.5. Electric Field in the Full Atrial Mode	67
5.6. Contact Area Investigation: Removal of Tissue Tenting	69
6. DISCUSSION	70
6.1. Assessment of Multiphysics and Catheter Design Aspects in 2D and 3D Models	70
6.2. The Left Atrial Anatomical Model.....	70
6.3. Ablation Simulation Performance vs Experimental Studies.....	71
6.4. Associated Diagnostic Studies.....	72
6.4.1. Fluid Velocities and Blood Cooling.....	72
6.4.2. Contact Area Investigation	72
6.5. Limitations	73
6.6. Next Steps.....	74
6.7. Conclusions.....	76
REFERENCES.....	77
APPENDICES	
A. Convergence Testing on Tissue Depth of Simplified Verification Models.....	94
B. Fusion 360 Left Atrial Model	96
C. COMSOL Multiphysics® CAD Left Atrial Model	98
D. Early SolidWorks® Left Atrial Models	100
E. Final Left Atrial SolidWorks® Model	102

F. Protocol for Pre-processing and Transfer of Complex Geometric Models from SolidWorks to COMSOL.....	104
G. Material Domain Definitions in Left Atrial Model	105
H. Physics Verification Studies: Effect of Blood Flow, Saline Irrigation, and Temperature- Dependent Properties.....	108
I. Preliminary Flow Studies in the Left Atrial Model.....	112
J. Exploratory Characterization of Activation Energy Value Effect on Damage Quantification ...	114

LIST OF TABLES

Table	Page
1. Dimensions for Left Atrial Anatomy.....	33
2. Dimensions for Collateral Structures Near the Left Atrium	33
3. Dimensions of the Pulmonary Veins and Mitral Annulus.....	34
4. Overview of Boundary Conditions + Initial Values of the Left Atrial Ablation Model	40
5. Thermal and Electrical Material Properties, Temperature Independent	42
6. Biosense Webster Thermocool Ablation Procedural Parameters for In-Vivo 30W/60 sec Ablations in Porcine Models	54
7. Lesion Dimensions from Verification Studies in 2D and Simple 3D Ablation Models	58
8. Comparison of Lesion Dimensions from Left Atrial Simulations and Experimental Lesion Studies	64
9. Comparison of Blood Velocities in Doppler Echocardiography Study of AF Patients [89] vs the Left Atrial Model	66
10. Simulated Blood Flow vs Clinical Velocities from Doppler Echocardiography	112
11. Parametric Study on Inlet Velocities to Match Clinical Data for AF Patients.....	113
12. Lesion Dimension Comparison With Different PV Velocities.....	113

LIST OF FIGURES

Figure	Page
1. Schematic of (a) RF and (b) Cryoballoon Ablation Procedures to Treat Atrial Fibrillation.....	1
2. Measurement of Lesion Profiles After Tissue Ablation	3
3. 2D Axisymmetric Model of Epicardial RF Ablation	7
4. Anatomical Model to Study Esophageal Injury	8
5. Dissected 4 Chamber View of Cardiac Anatomy	11
6. Left Anterior View of Dissected Left and Right Atria	12
7. Theories on the Mechanisms of Atrial Fibrillation.....	14
8. Common Lesion Patterns in Catheter Ablation of Atrial Fibrillation	18
9. Heart Positioning Within the Thoracic Cavity.....	20
10. Heat Transfer Vectors in RF Ablation.....	23
11. Model of BioSense Webster Navistar Thermocool® 7.5 Fr Ablation Catheter, Created in SolidWorks®.....	27
12. Geometry of 2D Model Used for Physics and Properties Verification.....	28
13. Simple 3D Ablation Simulation Model.....	29
14. Posterior View of Left Atrium, Reconstructed from CT/MRI Data	31
15. Planes Used to Map Left Atrial Geometry from Anatomical Positioning to a Standard XYZ Configuration	32
16. Side View of Atrial Model.....	36
17. Left Atrial Assembly in COMSOL Multiphysics.....	38
18. Boundary Conditions of Full Left Atrial Model Space.	41
19. 37 °C and 37.1 °C Isotherms to Determine Ideal Study Region Diameter.....	43
20. Element Size Convergence Studies	44
21. Dimension Combinations from Element Sizing Convergence Studies	45
22. Mesh Convergence Plot: % Difference in Temperature at Tissue Depths of 3- and 5-mm vs the Degrees of Freedom in the Solution	46
23. Mesh Tissue Domains (Blue) and Blood Domain (Grey) in Full Model	47
24. Tetrahedral Mesh on Tissue (Blue) and Blood (Grey) Spherical Study Regions	48

25. Element Quality Plot, Medial View of Bisected Left Atrial Anatomy	50
26. Element Quality Plots of Aorta, Region of Interest, and Esophagus	51
27. Equilateral Tetrahedral Element (Left) Versus Flattened Tetrahedral Element (Right)	51
28. Convergence Plot of Time Dependent Solver.....	52
29. Comparison of Damage Criteria for Lesion Measurement in Ablation Studies	56
30. Temperature Distribution and Lesion Isotherms of Perpendicular Electrode Orientation Ablations in the 2D (Top) and Simplified 3D (Bottom) Models.....	59
31. Temperature Distribution and Lesion Isotherms After 60 Second Ablation With a Tangentially Oriented Electrode for the 2D (top) and Simplified 3D (Bottom) Preliminary Simulation	60
32. Temperature Plot, Medial View of Left Atrium Assembly.....	61
33. Lesion Morphology of 50 V, 60 s Ablation, Perpendicular Electrode Orientation	62
34. Temperature Distribution Following a 50 V, 60 Second Ablation, With Electrode Tip Oriented Perpendicularly to the Myocardial Surface.....	63
35. Temperature Distribution Following a 50 V, 60 Second Ablation, With Electrode Tip Oriented Tangentially to the Myocardial Surface.....	64
36. Streamlines of Blood Flow for Non-Irrigated (left) and Saline-Irrigated (right) Simulations in the Left Atrial Model.....	65
37. Blood Velocity Magnitude in the Left Atrial Model, Pulmonary Vein Inflow Velocity of 0.15 m/s.....	66
38. Flow Through the Left Atrium for Patients in AF and Sinus Rhythm	67
39. Electric Field With Overlaid Current Density Vector Field.....	68
40. Temperature Distributions in Full Atrial Model Following a 50 V, 60 Second Ablation With Tissue Tenting (Top) and Complete Insertion Contact (Bottom).....	69
41. Fusion 360 Left Atrial Model.....	96
42. “COMSOL CAD” Left Atrial Model.....	98
43. Mesh of COMSOL CAD Left Atrial Model	99
44. Early Atrial Models With 2 Planes of Symmetry	100
45. Early SolidWorks Model With 1 Plane of Symmetry.....	100

46. Interior View of Early Atrial Models With 2 Planes of Symmetry	101
47. Dimensioned Top View of Left Atrial Model	102
48. Alternate Views of Left Atrial Assembly	102
49. Posterior (Left) and Inferior (Right) Views of Left Atrial Assembly	103
50. “Generic Tissue” Domain in Full Model.....	105
51. Myocardium Domain in Full Model	105
52. Blood Domains in Full Model	106
53. Catheter Tip in COMSOL Model.....	107
54. Lesion Morphology in Simulations With and Without Blood Flow	108
55. Temperature Distribution after 60s of 50V Constant Voltage Ablation Without Irrigation (A), and With Irrigation of 30 mL/min (B).....	109
56. Damage Distribution after 60s of 50V Constant Voltage Ablation Without Irrigation (A), and With Irrigation of 30 mL/min (B).....	110
57. Effect of Temperature Dependent Properties on Lesion Production.....	111
58. Damage Evaluation Comparison, With Parametric Sweep of Activation Energy.....	114

1.1 Radiofrequency Catheter Ablation of Atrial Arrhythmias

Radiofrequency ablation catheters are minimally invasive medical devices used to electrically pace and ablate cardiac tissue to treat arrhythmias. Of these arrhythmias, atrial fibrillation (AF) is the most prevalent. AF is caused by disordered activation of the atrial myocardium which leads to non-coordinated contraction. Catheters for cardiovascular interventions are medical devices with steerable shafts made of flexible polymeric materials which are often structurally supported with wire coiling/braiding. They are used to deliver devices, drugs, fluids, or energy to treatment sites. Catheters enable physicians to perform interventions in locations that are difficult to access otherwise, with greater delicacy and precision. In ablation catheters, the distal end of the catheter is modified to have a tip that delivers thermal energy to the target tissues, as shown in [Figure 1].

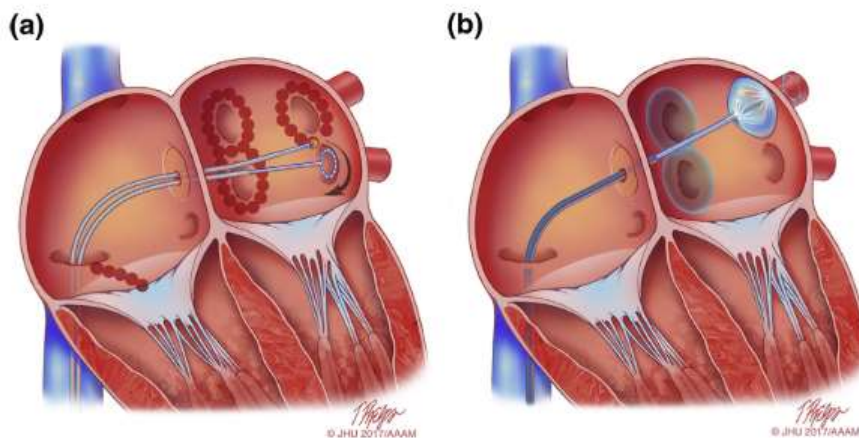


Figure 1. Schematic of (a) RF and (b) Cryoballoon Ablation Procedures to Treat Atrial Fibrillation.
Image Credit: Calkins et al 2017. Creative Commons Attribution 4.0 International License (<http://creativecommons.org/licenses/by/4.0/>)

This energy can take the form of laser, ultrasound, cryofreezing, MRI, radiofrequency or microwave electromagnetic waves. Creating patterns of scar tissue can isolate and/or terminate aberrant electrical activity in the heart, returning functionality.

1.2 Medical and Economic Burden of Atrial Fibrillation

Atrial fibrillation is a widespread cardiovascular pathology: estimates indicate anywhere from 2.7-6.1 million people in the United States have some stage of AF, with the prevalence expected to

rise to 12.1 million by 2030 [1]. This places a significant medical and economic burden on patients and the healthcare system, which already spends \$6 billion on the treatment and management of AF annually. These trends are not just limited to the US or developing countries either; observations of global populations also reflect rapidly growing incidence and economic burden of AF [2]. While AF alone is not acutely fatal, it impacts mortality rates, exacerbates other chronic health conditions, and drastically impairs quality of life.

Thromboembolism due to impaired contractile function of the atria is the major complication of AF [3], leading to a greatly increased stroke risk. Additionally, patients with AF tend to have worse outcomes (i.e. degree of disability, mortality rate) for ischemic strokes [4] [5]. In addition to stroke, this arrhythmia has also been linked with overall increases in mortality, risk of sudden death, heart failure, and the development of dementia [6], [7]. What makes this disease particularly pernicious is it's frequently asymptomatic in its early stages [5], when intervention is most effective. Studies have suggested that asymptomatic AF is associated with similar or worse prognostic outcome compared to patients with symptomatic AF [8]. Part of the reason for this is the progression of the disease: AF leads to structural and electrical remodeling of heart tissues [3]. This exacerbates existing cardiac conditions—i.e. through decreased contractility, increased heart wall fibrosis, increased left atrial volume, and decreased left ventricular ejection fraction [9]—which in turn contributes to the spread and maintenance of the disease.

1.3 The Interventional Electrophysiology Device Market

Given the medical and economic burden of this disease, it is not surprising that the electrophysiology (EP) device market is large and growing. In 2017, the EP device sector was valued at \$4.4 billion [10]. Additionally, this sector has maintained an impressive compound annual growth rate (CAGR) of 13% [11], ahead of many sectors in the medical device industry. With the aging of the population and ballooning number of AF patients in the next few decades, this field is expected to remain a critical area of investment and development for medical devices.

1.4 Problem Statement

The development of safe and effective ablation catheters increases the quality of patient outcomes while maintaining atrial functionality; however, ablation catheters can be difficult and expensive—in both time and resources—to research, design and test.

1.4.1 Current Methods of Ablation Catheter Lesion Evaluation

Most lesion evaluations consist of a tissue (or tissue substitute) placed in a heated bath of saline, then ablated with a catheter held in place with ~10-20 g of weight. The closest analogue to human cardiac tissue is porcine or bovine myocardium which is sliced apically to produce slabs of the ventricular myocardium for ablation studies. After ablation, the tissue is sectioned perpendicular to its surface and lesion dimensions are measured visually, with a ruler precision of ~0.5 mm, as illustrated in [Figure 2] [12].

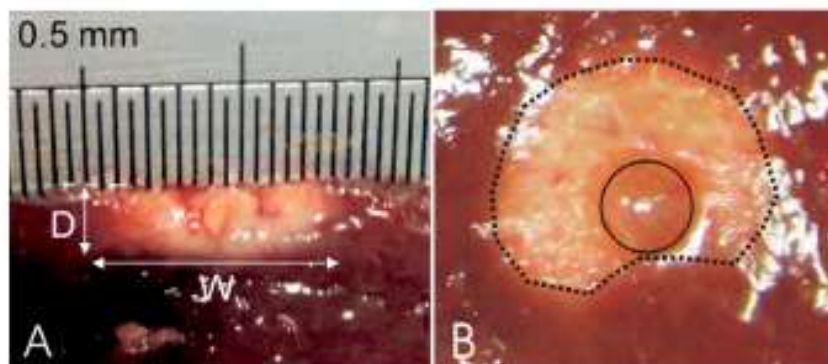


Figure 2. Measurement of Lesion Profiles After Tissue Ablation.
Lesion identified by paler zone of protein coagulation. Image credit: Arenas et al 2014 [48].
Published under Creative Commons Attribution License 4.0
(<http://creativecommons.org/licenses/by/4.0>)

These studies are used to characterize everything from catheter performance [13], temperature distributions, procedural factors influencing lesion formation [14], device quality, lesion geometry, control algorithms [15],[16], different electrode configurations [17] and much more. As expected, there is a lot of inherent variability in this testing procedure due to tissue inhomogeneity and visual assessment; therefore, to produce any statistically meaningful results, the sample size of studies needs to be large.

Gel phantoms made from agarose or polyacrylamide are an alternative ablation substrate used to reduce experimental variability [18]-[20]. These hydrogels typically contain a protein component that turns from translucent to opaque [21] or shifts colors [22] once it is denatured by the application of heat. In some gels, the electrical properties can be tuned with the titration of ionic compounds like sodium chloride. These gels are great tools for basic comparative experiments and catheter performance characterization, but while convection of blood across the ablation substrate surface can be mimicked with saline, there has yet to be a good way to recapitulate the perfusion effect present in living tissues.

1.4.2 The Utility of Computational Models

An alternative approach is the use of numerical methods like Finite Element Analysis (FEA) to simulate the physical situation. Variability in results are minimal, and many different metrics can be measured at a much finer resolution throughout the entire simulation space. These models aid in understanding the underlying physics of the ablation procedure physics; moreover, these simulations be helpful for device development and design, teaching tools or for procedural planning.

1.4.3 Regulatory Stance on Computational Models

In the past, the FDA relegated such numerical studies as purely research and design tools; however, their viewpoint has recently shifted. Computational models may support medical device regulatory submissions, so long as they are accompanied by relevant validation studies [23]. Therefore, many individuals in the AF treatment pipeline—from researchers to design engineers to regulators and clinicians—can benefit from these *in silico* simulations.

1.5 Previous RF Ablation Computational Studies

1.5.1 Literature Review

Computational models are developed to bridge the gap between bioheat transfer theory and empirical experience with RF ablation devices. These simulations provide valuable insight into device design, procedural aspects, parameter selection for procedural planning [24], and other facets of RF ablation *in silico*. Early modelers primarily used FEA to verify the Pennes's Bioheat transfer model in a 1D single domain [25]. Simple scenarios such as these are still used to test different models of Bioheat transfer, such as hyperbolic heat transfer [26]. With growing computing capability, experimental validation, and empirical data on material properties and device performance, 2D, 2D axisymmetric [27], [28], and 3D geometries [29] have also come into use.

One of the key developments in intracardiac ablation modelling was in assessing the cooling effect of blood on RF ablation. In early models, researchers chose to omit the blood volume, or treated it as a static blood pool [30]. Likewise, many neglected heat loss due to blood perfusion of tissues [14], [31], with the rationale that the heat losses were not significant. This assumption might not be appropriate for highly vascularized tissues like the myocardium. Jain and Wolf produced several papers on the FEA analysis and validation experiments, finding the effect of convective blood cooling significant enough to necessitate inclusion when building RF ablation models [32]-[36]. In these models, temperature rose faster and reached a greater magnitude with higher blood flow rates [39], [41], demonstrating lesion variability due to flow velocity. Further studies—both computational and experimental—went on to support these findings [38]. While not complex in theory, the coupled multi-physics effect of heat transfer due to nearby fluid flow in multiple domains is computationally expensive to solve with numerical methods. Thus, many studies chose to approximate heat loss due to blood flow with a convective heat transfer boundary condition at the blood/electrode and blood/tissue interfaces.

Early uses of this convective heat transfer boundary condition include Min and Mehra [39], who applied Newton's Law of Cooling ($Q = h(T_{ext} - T)$) to solve for the heat flux between the tissue and blood. T_{ext} represented arterial blood temperature (i.e. 37 °C), T represented local temperature, and Q was the heat flux across the boundary [W/m²]. Values for h were determined experimentally

[41], [42], and included simple constant values as well as more complex versions of h . For example, h values were specialized for short ablation times [43], or for different blood velocities, vessel compositions and sizes [44]. Use of this boundary condition was tested against fluid flow in studies by Gonzalez-Suarez, Cao, and others; these studies found that the difference in lesion results were insignificant and mainly differed in asymmetry of lesion profile due to directional cooling [35], [37], [45], [46]. While use of this boundary condition didn't overtly affect lesion performance, accurate estimation of blood temperatures during ablation was not possible [47]. Therefore, a convective boundary condition was adequate for lesion studies (e.g. [14], [41], [42], [44], [48], [49], [50]), but inadequate for predicting aspects like blood temperature distribution [51] or thrombus formation [47]. With the introduction of saline irrigation of catheter tips, modeling conjugate convective flow—the flow interaction of blood with structures—became even more necessary in numerical models of RF ablation [49], [45], [46], [52].

Energy delivery methods have also varied across ablation studies. In clinical RF generators, electrical energy is output as a 500 kHz oscillating wave, with output power of up to 200 W. To facilitate solution of the electromagnetic heating in FEA simulations, physical approximations are made. The operating frequency range for RF devices means that the magnetic component of tissue heating is typically negligible; therefore, the resistive heating can be solved for quasi-statically. This is done by applying a constant voltage to the electrode surface, equivalent to the root-mean square (RMS) of the RF wave peak voltage (e.g. [14]). Furthermore, modelers like Haemmerich 2005 and 2010 and Lai 2004 implemented control algorithms to mimic the function of commercial RF generators. These algorithms utilized proportional-integral-derivative (PID) programming feedback mechanisms to titrate power output based on intra-procedurally measurable factors such as temperature [15], [16], and impedance [53], [54].

Although many models use constant electrical and thermal property values, tissue properties during ablation can change as a result of temperature, tissue inflammatory response, coagulation/desiccation, and water phase changes. As such, further studies examined the effect of parametric material properties during RF ablation. Tungjitkusolmun implemented temperature change using % change / °C like relationships [55]. Lai et al 2004 and Cao and Paul et al also utilized temperature-dependent properties in their models [42], [37]. Arenas et al and Chen and Sidel made

use of damage-dependent perfusion to reproduce the local increase in perfusion over a temperature interval of 37 – 45 °C, with a complete cessation of flow at 50 °C due to tissue coagulations [44], [49]. Others like Gonzalez-Suarez et al 2015 and Watanabe 2010 used piecewise equations to model tissue electrical conductivity [46], [56]. Enthalpy methods have also been employed (e.g. [49], [46], [57]) to model liquid and gas phases of water; however, most other models terminated when temperatures exceeded 100 °C.

An aspect of RF ablation simulations that has seen little development in the past decade has been the incorporation of more realistic anatomical geometries. Almost all models utilize a simple tissue block with an adjacent blood volume. The catheter is placed orthogonal and inset into the tissue surface, while fluid flow (if included) runs parallel to the tissue surface. An example of this geometry is shown in the figure below [Figure 3].

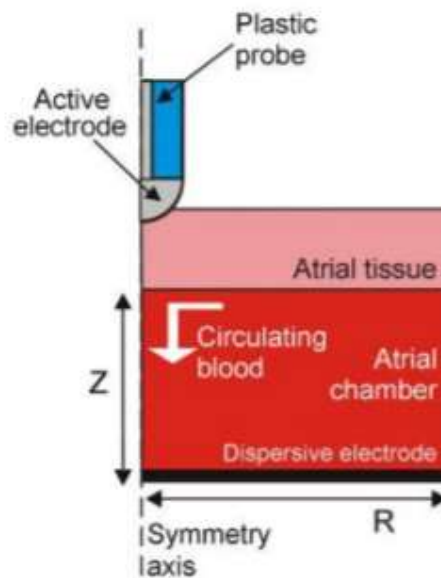


Figure 3. 2D Axisymmetric Model of Epicardial RF Ablation

Image credit: Review article by Enrique Berjano, 2006. Image published under Creative Commons Attribution License 2.0 (<http://creativecommons.org/licenses/by/2.0>)

For simple comparative and optimization studies for device design, this methodology is adequate to get meaningful results. One of the few published models that included more geometric complexity were the works of Berjano and Hornero, who studied esophageal damage during left atrial intracardiac ablation [59], [60]. Their 3D model included a chunk of the thoracic cavity around the left

atrium with bits of collateral tissues (i.e. lung, esophagus, aorta), as depicted in the image below [Figure 4].

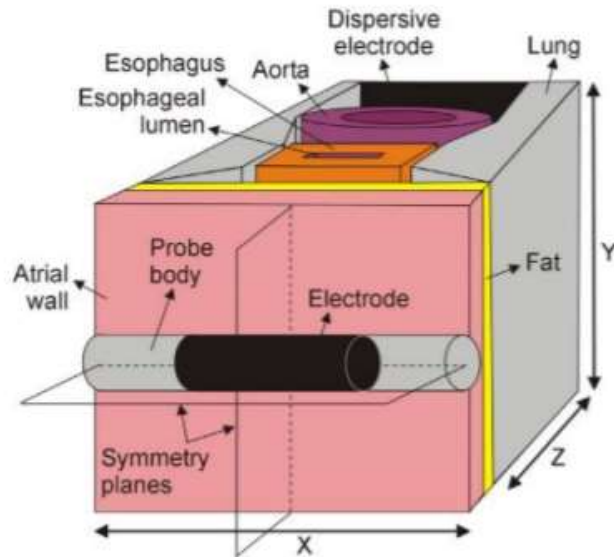


Figure 4. Anatomical Model to Study Esophageal Injury

Image credit: Berjano and Hornero, 2005 [59]. Published under Creative Commons Attribution License 2.0 (<http://creativecommons.org/licenses/by/2.0>).

This enabled them to study power titration strategies to prevent thermal damage of the esophagus. In-clinic, esophageal burns often leads to atri-esophageal fistula, a severe and frequently fatal adverse event.

Anatomical realism in left atrial ablation models has not progressed much since then; however, studies for other RF ablation scenarios have adopted more morphologically realistic geometries as a means for procedural planning, preclinical testing, and patient personalization. Audigier et al reported on a hepatic tumor ablation model that utilized segmented image stacks and magnetic resonance imaging (MRI) flow studies to build a replica of the patient's liver and associated major vasculature. This model was used to determine lesion formations in various regions of the liver, and validated by *in vivo* studies with adult pigs [61]. A particularly interesting outcome was the workflow that this group developed to allow for quick and personalized pre-procedural planning in clinic.

Although simplification of geometry is a necessary aspect of all FEA studies for reasons of practicality, Berjano et al and Audigier et al demonstrated that much could be gained from developing more anatomically relevant geometries for simulations. The bulk of realistic LA models are used in electrophysiology studies, where tissue composition and morphology are important to producing accurate activation and arrhythmia patterns of the atrial myocardium. Morphology is derived from segmented images of computed tomography (CT) or MRI, as well as histologic studies of fiber orientation [62], [63]. These models provide a great deal of insight into the initiation and termination of AF; yet for electrical and thermal studies, that level of realism is not necessary or practical to users like catheter design engineers. Thus, a balance between the simplicity of the tissue block and life-like atrial models, coupled with accurate electrical and thermal properties (i.e. parametric behavior) as well as a realistic blood cooling effect could provide a valuable tool in evaluating atrial ablations.

1.6 The Proposed Model

In this thesis, an anatomically relevant multi-physics computational model of left atrial ablation is presented. The intended use is as *in silico* test bed for catheter designs, allowing for evaluation of catheter performance and procedural aspects like collateral damage.

1.6.1 Thesis Aims

This thesis addresses the following questions:

- 1) Can a biophysical model of AF ablation be developed in COMSOL Multiphysics?
- 2) Can relevant metrics of RF ablation be evaluated from this model and compared to literature?
- 3) Can an anatomically relevant 3D model of the left atrium be developed using solid-modeling software/computer-aided design (CAD)?
- 4) Can the biophysical model for AF ablation be applied to the expanded anatomical model?

1.7 Summary of Contents

First, Chapter 2 provides an overview of the anatomy, pathophysiology, and medical management of atrial fibrillation. Chapter 3 lays out the theory behind the Bioheat transfer used to develop the multi-physics model. Chapter 4 presents the model development process, including: geometry, applied boundary conditions, material models, etc. In Chapter 5, the results of the

simulations are reported, including mesh convergence and model validation versus literature. Chapter 6 discusses the significance of these results, limitations, and future directions. Finally, Chapter 7 summarizes major conclusions and recommendations based on the findings of this thesis.

2.1 Normal Function of the Heart

The left atrium is a chamber of the heart located above the left ventricle which receives oxygenated blood from the lungs via a set of 4-5 pulmonary veins. While blood flows from the left atrium to the left ventricle, it through the mitral valve. The mitral valve is seated in elliptical ring of tissue call the mitral annulus (~ 3 cm major axis; 2 cm minor axis). For the majority of the cardiac atrial activation cycle, blood flows passively through the atria to the ventricles. The atria are only active for 15% of the atria cycle [64]—which encompasses depolarization by the sinoatrial node—providing ~20% of the total blood volume into the ventricles prior to the closure of the mitral valve [3]. During systolic contraction, the blood back pressure of the ventricles closes the mitral valve, and the blood is ejected out through the aortic valve into the systemic circulation. This circuit is illustrated in [Figure 5].

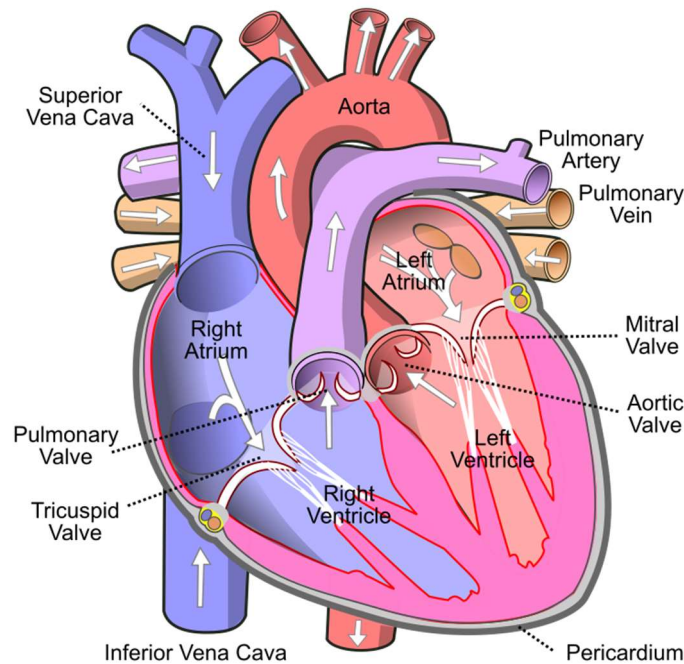


Figure 5. Dissected 4 Chamber View of Cardiac Anatomy.

Arrows indicate the direction of blood flow. Image credit: Wapcaplet. Graphic published under the Creative Commons Attribution-Share Alike 3.0 Unported license (<https://creativecommons.org/licenses/by-sa/3.0/deed.en>).

The pulmonary veins are located on the posterior wall of the left atrium, and are identified by their direction relative to the atria as they connect from the lungs. In most individuals, there are four main pulmonary veins—the right superior (RSPV), the right inferior (RIPV), the left superior (LSPV), and the left inferior (LIPV)—with several frequently observed variations. For example, the ipsilateral veins may share a common trunk, or there may be a third middle vein between the superior and inferior branches. Typical diameters for the PVs are ~13 mm, with the superior PVs having a larger diameter than that of the inferior PVs. Wall thickness of PVs proximal to the atria is ~0.50 mm [65]. Each set of right and left pulmonary veins is usually joined by a thickened ridge of tissue known as the pulmonary sinus. The tissue surrounding the pulmonary vein openings is called the PV ostium. Major anatomic landmarks of the left atrium are depicted in [Figure 6].

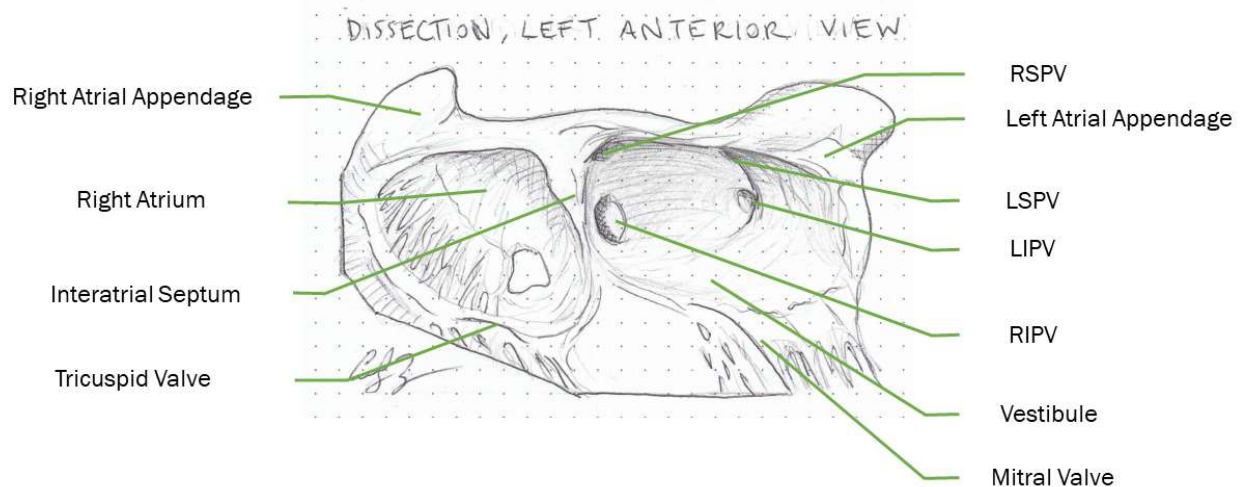


Figure 6. Left Anterior View of Dissected Left and Right Atria.

Image credit: Carolyn Teng. Resources referenced: [66], [67], [68].

During normal sinus rhythm, excitation of the heart originates in the cells of the sinoatrial node located at the apex of the right atrium. The depolarization of contractile cells spreads through the right and left atria, then converges on the atrioventricular node. Activation of the atria causes their walls to contract, pumping blood into their respective ventricles. The conduction velocity of the depolarization wave is slightly delayed at the AV node, after which it races down the Bundle of His, then out to the Purkinje fibers which activate the ventricular myocardium.

2.2 Etiology of Atrial Fibrillation

Atrial fibrillation (AF) is the uncoordinated activation of the atrial myocardium which leads to impaired atrial contractility. The exact initiation of AF is still the subject of debate; however, what is generally agreed upon are the conditions necessary for its initiation and maintenance. That is, the triggering event must also be accompanied by a pro-fibrillatory tissue substrate for AF and other arrhythmias to occur. Contributing factors include the histological makeup of the atrial walls, the innervation and/or automaticity of anatomical structures, and the function of the transmembrane ion channels that govern conduction and contraction of the heart [3], [69].

2.2.1 Causes

Abnormal spontaneous activity (a.k.a. focal ectopic firing) and reentry currents are the two major causes of arrhythmia [3], [70]. The predominant source of aberrant potentials in AF comes from the muscular sleeves of the PVs. These muscle cells are responsible for the dilation and contraction of the PVs to control flow, as a throttle valve might in a mechanical fluid transport system. However, because they are self-activating, the depolarization waves they generate can escape from the PVs into the greater atria, as depicted in [Figure 7].

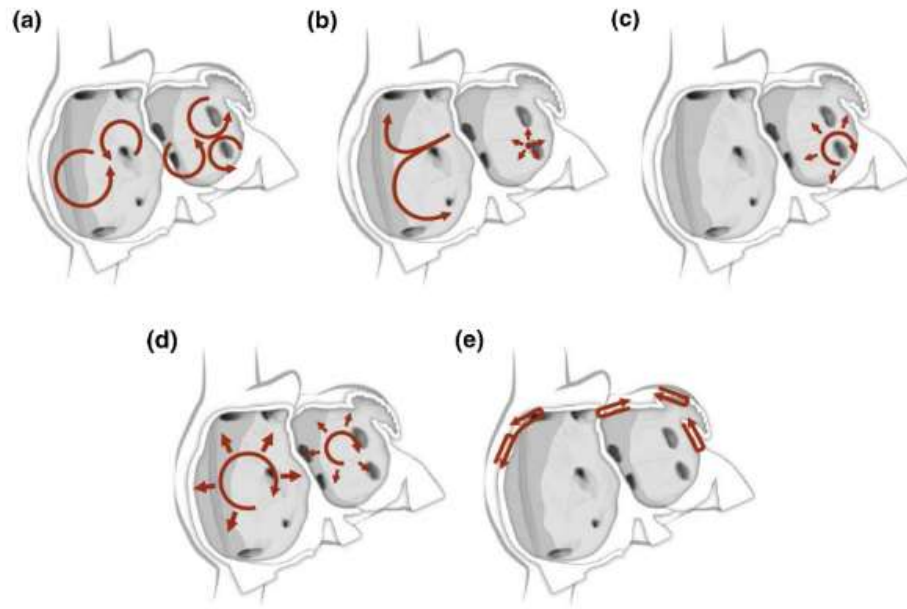


Figure 7. Theories on the Mechanisms of Atrial Fibrillation.

a) Multiple wavelets hypothesis, b) automatic foci, c) single reentrant circuit with fibrillatory conduction, d) functional reentry, and e) AF maintenance due to dissociation between epicardial and endocardial layers. Image credit: Calkins et al 2017 [69]. Published under Creative Commons Attribution 4.0 International License (<http://creativecommons.org/licenses/by/4.0/>).

As these potentials occur at a much higher frequency than those generated by the sinus node, they can interfere with normal activation of the atrial myocardium. For example, they might collide with and terminate the depolarization wavefronts from the SA node, or prematurely excite the tissues ahead of these wavefronts, blocking normal conduction. Alternatively, if the gap between potentials during sinus rhythm is long enough, these potentials may cause early and/or off-beat atrial activation. Thus, different sections of the tissue in the atrium could be activated out of sync with adjacent tissues.

A separate but sometimes concurrent arrhythmogenic phenomenon are re-entry currents. Cardiomyocyte depolarization is mediated by a sequence of voltage-gated and active transmembrane channels, which facilitate the flow of ions across the cell membrane to generate an electric current. This current propagates through the cells to adjoining cells. Once depolarized, the cell requires a period of time for ion pumps to return the cardiomyocyte back to its resting electrical potential. This is known as the refractory period. During this period, further stimulus to the cell does not trigger depolarization. Re-entries typically arise when there is a difference in conduction rates through

adjacent tissues. After the passage of the “fast” wave of depolarization, the “slow” wave of depolarization is blocked from further progression by the resetting of the cells activated by the “fast” wave. If the originating tissues have sufficient time to repolarize, the wavefront loops back around instead of terminating. This forms what is known as a circus reentry or rotor [Figure 7a, 7c, 7d]. Additional factors that lead to arrhythmia formation include decreased conduction velocity, decreased atrial refractoriness, unidirectional block, or increased dispersion [7]. [69]. Re-entry currents sometimes “anchor” themselves around an anatomical structure; in the left atrium, a common anchor structure is the pulmonary vein opening.

2.2.2 Risk Factors

There are multiple congenital, pathological and lifestyle factors that contribute to increased AF risk. Incidences of AF tend to crop up after cardiovascular events and diseases, such as myocardial infarction, high blood pressure, valve disease, sick sinus syndrome, or congenital heart defects. Other health conditions that contribute to AF include endocrine diseases (e.g. diabetes or hyperthyroidism), pulmonary disorders (e.g. chronic obstructive pulmonary disease, obstructive sleep apnea), and lifestyle choices like excess alcohol and caffeine consumption [3],[7], [69]. Many of these risk factors are associated with an increased cardiac burden (i.e. higher preload, hypertension, etc.), which leads to progressive structural and electrical remodeling, fibrosis, and atrial enlargement [3]. Because of this, most AF patients (~90%) have some form of concurrent cardiovascular disease, such as hypertension, coronary heart disease, valvular heart disease, dilated cardiomyopathy, pericarditis or heart failure [69]. These conditions primarily lead to an increase in fibrosis, which obstructs or complicates conductivity of the myocardium.

2.3 Pathophysiology of Atrial Fibrillation

2.3.1 Symptoms

Symptoms for AF include: irregular heartbeat, heart palpitations, dizziness / lightheadedness, shortness of breath, fatigue, angina, syncope, and confusion. Many of these symptoms are linked to reduced stroke volume and/or increased pulmonary circuit load.

2.3.2 Disease Progression

The classifications for severity of AF are outlined by the AHA/EHS consensus statement [1] as follows:

- First detected: 1 diagnosed episode
- Recurrent: 2+ diagnosed episodes
- Paroxysmal: Self-terminating in <7 days
- Persistent: Fibrillatory episodes last > 7 days
- Permanent: long-term or chronic fibrillation

While these classifications are primarily for diagnostic purposes, they loosely correlate with the progression of the disease. Fibrillation leads to structural and electrical remodeling (slowed conduction, fibrosis, unidirectional block, etc.), which begets longer and more frequent fibrillatory episodes [7]. As the disease progresses, the tissues making up the atria become more histologically and electrically complex [3], [7], making it difficult for the natural termination of fibrillation and reestablishment of sinus rhythm.

2.3.3 Prognosis

With proper rhythm and thromboembolism management, AF alone is not usually fatal. Progression of AF to later stages—in which fibrillatory episodes are more frequent and sustained—poses a greater risk of thrombus generation. One study found that ~25% of patients with paroxysmal or persistent AF developed more severe forms of AF within a 1.5 year follow up period [72]. AF dramatically increases the risk of ischemic stroke: up to 5x that of non-AF patients [7]. The strokes caused by AF tend to be more severe than typical strokes, with the risk of serious disability and death 3-months following the ischemic event estimated at 50% and 60%, respectively [5]. AF is also associated with up to a 30% higher risk of cardiovascular events (i.e. congestive heart failure, left ventricular dysfunction, mortality, myocardial infarctions) compared to patients in sinus rhythm [7], [64], [73]. Therefore, proper treatment in earlier stages can help mitigate these risks.

2.4 Treatments for Atrial Fibrillation

Treatments for AF include both pharmacological and surgical interventions. The anti-arrhythmic drugs (AADs) are broken up into rate and rhythm control drugs. Rate control therapy is a ventricular -focused approach that limits sinus activation rates (<100 BPM) to decrease the burden on the heart. This method aims to preserve heart tissue and slow the destructive progression of cardiovascular disease [74], and are also used in the management of other arrhythmias as well as

myocardial and coronary diseases. Still, these drugs only treat the functional consequences rather than the source of AF [3]. The objective of rhythm control drugs is to restore and maintain a normal sinus rhythm. Meta-analyses of rhythm versus rate control drugs have found no significant difference between the efficacy of these drugs [75], [76], but there has been evidence of increased risk of adverse events with rhythm-control drugs versus rate control drugs [75], [77]. Moreover, efficacy of these drugs is low, with one meta-analysis reporting AF free survival at 12 months of 18.8% vs 75.7% for surgical intervention [77]. The lack of efficacy coupled with the risk of severe side effects means that patients unresponsive to the drugs are referred for more direct interventions.

In the 1980's, the Cox-Maze procedure was developed to help isolate the rogue stimuli causing AF. This open-chest procedure involved cutting the atria into sections, then suturing them back together. The resulting scar tissue at each of the joins formed insulative lesion lines. Though invasive, the Cox-Maze procedure had remarkably high rates of success. Some studies reported long-term freedom from AF rates at 75-85%, depending on the lesion pattern used [67]. Over the past 3 decades, the focus has largely shifted to recapitulating the success of the Cox-Maze procedure with minimally invasive interventions. Instead of open surgery, lesions are created via ablation using specialized percutaneous catheters. The Cox-Maze procedure is still being used—sometimes in concert with RF ablations—to treat persistent and more advanced stages of AF.

These steerable catheters are inserted into the patient's vasculature via the femoral or axillary vein and navigated through either the inferior vena cava or superior vena cava to the heart (respectively). To access the left atrium, a puncture is made in the interatrial septum at the location of the foramen ovale. Through this port, electrical mapping and ablation catheters can be passed through. Upon deployment to the target tissues, the catheters deliver energy to the atrial wall. This causes local tissue death via hyper- or hypothermia—depending upon the technology used—and the formation of insulating lesions, isolating arrhythmogenic areas such as the pulmonary veins [71], [78].

2.5 Anatomical Considerations for Atrial Fibrillation Ablation

2.5.1 Targets for Ablation: Pulmonary Veins

PVs are a key arrhythmogenic anatomical feature in the left atrium and are the primary target for ablation during intracardiac catheter ablation of AF. There are several lesion sets employed for

isolation of the PVs (i.e. segmental/ostial, circumferential, circumferential/antral) [71], [78] [Figure 8]; however, the ultimate goal of all of these patterns is to form a continuous transmural lesion around the PV openings to prevent propagation of the pulmonary vein potentials (PVPs) from spreading. Direct ablation of the PV opening is not ideal, as it has the potential to cause PV stenosis. This narrowing of the PV diameter can lead to pulmonary hypertension and ventricular decompensation [3]. Hence, the isolation patterns can cross large portions of the atrial myocardium, as shown in the following figure [Figure 8].

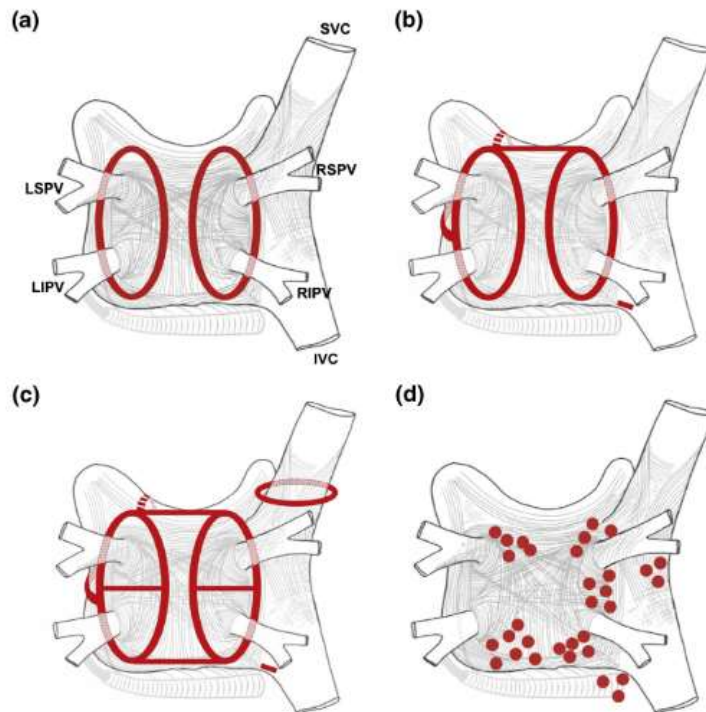


Figure 8. Common Lesion Patterns in Catheter Ablation of Atrial Fibrillation.

(a) Circumferential, (b) circumferential + antral, (c) circumferential, ipsilateral, roofline, mitral isthmus, and (d) focal electrogram guided ablation patterns. Image Credit: Calkins et al 2017. Creative Commons Attribution 4.0 International License (<http://creativecommons.org/licenses/by/4.0/>)

2.5.2 Targets for Ablation: Non-Pulmonary Vein Structures

Depending on the stage and complexity of the AF, other aspects of the atrial anatomy might be targeted during catheter ablation. Generally, these take the form of linear lesions across the lateral atrial posterior free wall, the posterolateral left atrial ridge and the mitral isthmus. Some surgeons may

also isolate the left atrial appendage and the superior vena cava. If remaining aberrant potentials persist, the electrogram (a spatially correlated measure of intracardiac electrical activity, like an ECG) is referenced to try to locate the source of the focal potentials and eliminate them [78]. Examples of these lesion sets are depicted in [Figure 8b, Figure 8c]. Choice of additional ablation is guided by physician experience and mapping catheter capabilities.

2.5.3 Transmurality + The Importance of Atrial Wall Thickness

Successful electrical isolation requires transmural lesions—lesions that cross the entirety of the atrial wall thickness. Problematically, wall thickness is not uniform and can vary greatly within patients, between patients, and between measurement modalities (i.e. ex vivo, CT, MRI). For example, in a LaPlacian assisted segmentation of CT left atrial wall thickness, one group found an average wall thickness of 0.6 -1.0 mm, although values ranged from 0.5 – 5.0 mm [79]. Another study which relied on dissection and manual measurement of excised hearts found that for patients >50 years of age whose primary cause of death was not due to cardiac pathology, average wall thickness was 2.09 ± 0.89 mm for the anterior LA, 1.25 ± 0.31 mm for the posterior LA, 1.33 ± 1.46 mm for the LAA, 1.75 ± 0.29 mm for RA, and 1.31 ± 0.36 mm for RAA. There was up to $\pm 50\%$ standard deviation spread from mean measurements. In this study, researchers proposed that the high degree of inter-donor variability could be attributed to both anthropomorphic variability as well as concurrent illnesses which could alter anatomical structures [80].

In the cases of PV reconnection (unsuccessful isolation), the most common culprits are the PV-left anterior appendage ridge on the left roof and the intervenous ridge [81]. These thick muscular ridges pose an issue because they require more power to achieve transmural and make it difficult for the physician to place the catheter flush with the tissue. On the other hand, overestimating the thickness of the atrial wall has its own issues. Thin atrial walls are especially susceptible to intracardiac trauma, such as cardiac tamponade or perforation by the catheter tip. These adverse events may require open surgery to fix, further increasing the health risk for the patient. While guidewire-assisted navigation and placement of catheters can mediate some of this risk, the delicate anatomy is still at risk due to the potential for over-deposition of RF power, which could cause excessive damage to collateral tissues.

2.5.4 Collateral Damage Risks

Thermal damage to adjacent anatomical structures is of critical concern in left atrial ablations, as there are many structures in close proximity to the target area. Structures including the esophagus, descending aorta, phrenic nerve, and vagal nerve all pass within close proximity to the posterior wall of the left atrium, as shown in [Figure 9].

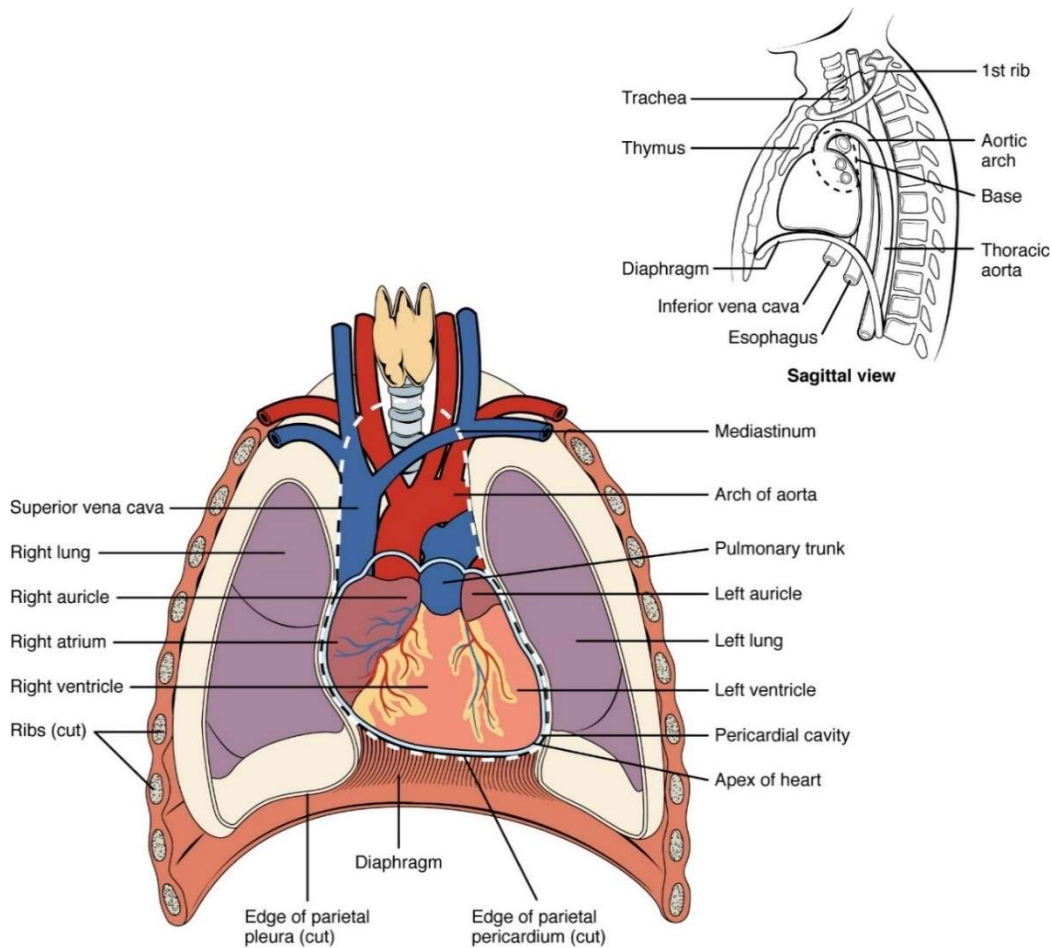


Figure 9. Heart Positioning Within the Thoracic Cavity.

Sagittal view depicts proximity of the esophagus thoracic aorta to the posterior wall of the left atrium. Image credit: Dongho Kim [82]. Licensed as Creative Commons Attribution-Non-Commercial-ShareAlike 4.0 International. (<https://www.oercommons.org/authoring/18546-heart-anatomy/view#>).

This area of the atrium has particularly thin walls compared with the rest of the chamber. The phrenic nerve innervates the diaphragm, while the vagal nerve innervates the heart, lungs, and digestive tract down to the colon. Although these neurons are primarily sensory and communicate the status of organs to and from the brain, damage to the phrenic nerve could result in rapid or labored breathing,

coughing, or hiccups. Damage to the vagal nerve can result in heartburn, difficulty swallowing, nausea, bloating, and constipation [83]. While these injuries are relatively minor and may resolve on their own, there are more severe consequences to collateral damage during ablations that are often debilitating and/or fatal.

For example, a major and lethal complication of ablation procedures is the atrioesophageal fistula. The esophagus descends close to the posterior wall of the left atrium. During ablation of the PVs and posterior wall, heat can propagate to the esophagus, causing trauma and an unnatural connection between the esophagus and left atrium. This opening leads to air embolism, pericardial effusion, hemorrhaging, bacterial infection leading to rapid sepsis, and death. Current practice is to minimize power on the posterior wall of the atria to minimize risk of esophageal damage or atrioesophageal fistula formation [84]. Researchers and clinicians suspect that a small endocardium/esophageal distance and the absence of fibrofatty connective tissue between the myocardium and the esophageal wall may increase the risk of this complication [85]. As such, pre-procedural planning must consider BMI on top of age, thromboembolic risk, and concomitant cardiovascular diseases.

3.1 Overview of Relevant Physics

Radiofrequency lesions in tissue are formed when alternating electrical current at ~500 kHz (range: 10 – 2000 kHz) is transmitted from a metal tipped electrode to a dispersive ground electrode adhered on the patient's back or leg. As power transits from the ablation site to the grounding electrode, it transfers energy to the intermediary tissues through the process of Joule (resistive) heating. Due to the high surface area mismatch between the dispersive electrode and the active electrode, the current density and consequently the power deposition is high adjacent to the catheter tip. The electrical potential drops rapidly—proportional to $1/r$ where r is the radial distance from the electrode surface—therefore, only a thin section of tissue adjacent to the electrode is heated directly. This heat then propagates to surrounding tissues via thermal conduction.

Tissues experience irreversible damage (i.e. protein coagulation, desiccation, and char) at $\geq 50^\circ\text{C}$, resulting in the formation of a lesion (i.e. injury). The type of damage is temperature dependent: coagulation dominates from $35\text{--}60^\circ\text{C}$, desiccation occurs from $60\text{--}100^\circ\text{C}$, and char/carbonization of tissue happens at temperatures above 100°C [86]. The necrotic tissue of the lesion—and later the fibrotic scar tissue—lacks the excitability and conductivity of muscle or nerve cells, hence terminating any activation waves that hit it. By insulating the healthy tissues from the aberrant currents, normal rhythm can be restored with minimal loss of function to the overall cardiac chamber.

There are several effluxes of heat from the system, as illustrated in [Figure 10]. A portion of the heating during ablation is lost to perfusion of the tissues, whether via capillary bed or through adjacent vessels. Additionally, convective heat loss occurs at the blood/tissue and blood/electrode interfaces. The degree to which heat is lost to either blood volume, be it intracardiac or epicardial/intramuscular is dependent on the catheter location within the heart and the blood velocity at the ablation site.

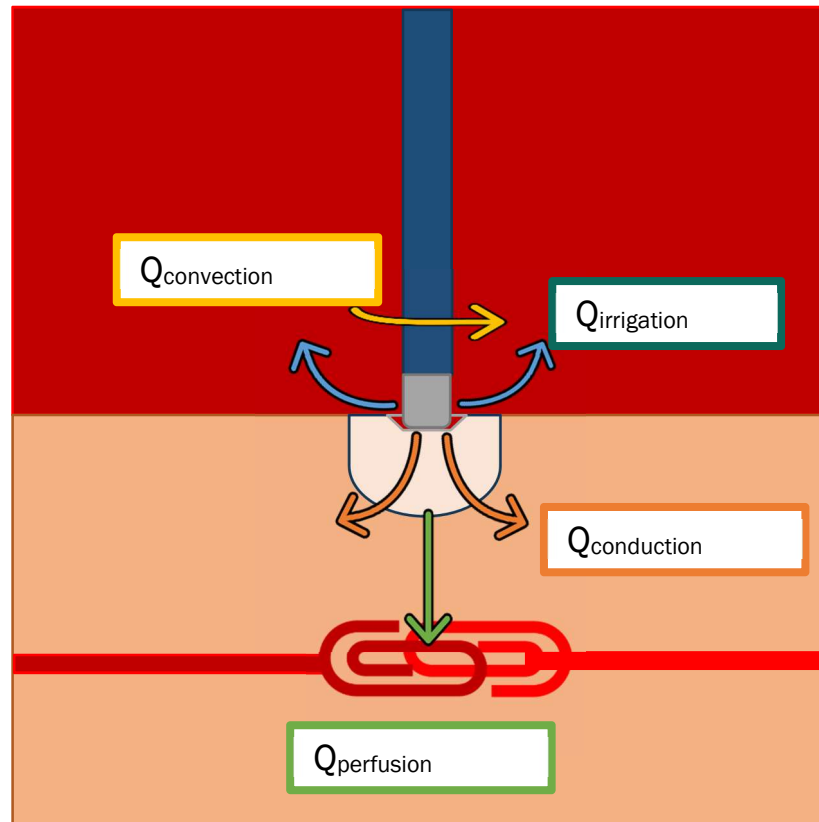


Figure 10. Heat Transfer Vectors in RF Ablation.

Green = heat efflux due to capillary perfusion. Blue = heat efflux due to 20 °C saline irrigation. Yellow = heat efflux due to blood convection over the tissue surface. Orange = heat transfer due to conduction to adjacent media.

To prolong RF deposition for the creation of larger lesions and to avoid adverse events, many catheter designs include irrigation of the tip. There are two types of irrigated catheters: closed loop irrigation, and open irrigation. Open-irrigated catheters contain several irrigation port holes located in the electrode tip through which room temperature heparinized saline is pumped to cool the tip. The fluid motion and cooling effect of this saline fluid flow prevents coagulum formation and steam pops, and enables further current deposition [87]. These events are of concern due to the associated thromboembolic and cardiac perforation risk, respectively. Moreover, they tend to be self-exacerbating: insulating coagulum decreases the usable surface area of the electrode, resulting in higher current densities which lead to more intense local heating. Local temperatures may exceed 100 °C, which results in the liquid-to-gas transition of water vapor in the blood and in tissues, producing tiny explosions that can be heard as an audible pop. If this expansion happens within the tissues, this could lead to perforation. Deposition of RF current can be halted by a rapid impedance

rise induced by insulative material on either the catheter tip (coagulum) or tissue (char) surfaces, or the formation of water vapor.

3.2 Mathematical Models of Ablation Biophysics

3.2.1 Heat Transfer: Pennes' Bioheat Equation

Heat transfer in biological tissues is often described by the Pennes' bioheat transfer equation: a derivation of Fourier's law of thermal conduction where the rate of heat transfer through a material as a function of the thermal conductivity of the material and the negative gradient in the temperature, as shown below

$$\vec{q} = -k\vec{\nabla}T$$

where \vec{q} is the heat transfer, k is the thermal conductivity of the participating material, and $\vec{\nabla}T$ is the gradient of temperature normal to the isotherms within the material. Each expression within the Pennes' bioheat equation represents the individual components of heat flux due to blood convection and tissue perfusion and heat sources, as shown in the equation below.

$$\rho_T C_{p,T} \frac{\partial T}{\partial t} + \rho_B C_{p,B} \vec{u} \cdot \nabla T = \nabla \cdot \vec{q} + Q_e + q_0 + Q_{bio}$$

The left hand side (l.h.s.) expressions represent the time-varying heat distribution of the tissue (1st term, l.h.s.), the heat flux due to blood flow (2nd term, l.h.s.), where ρ_T is the density of tissue [kg/m³], $C_{p,T}$ is the specific heat of tissue [J/kg · K], $\frac{\partial T}{\partial t}$ is the time-varying temperature gradient [K/s], \vec{u} is the velocity field, ρ_B is blood density, $C_{p,B}$ is the specific heat of blood and T is the local temperature. On the right-hand side (r.h.s.) the expressions represent the conductive heat flux (1st term, r.h.s.), resistive heat flux (2nd term, r.h.s.), any initial heat fluxes (3rd term, r.h.s.), and the biologic heat flux in living tissue substrates (4th term, r.h.s.). Q_{bio} is a combination of heat flux due to perfusion and the metabolic heat generation, given by the following equation:

$$Q_{bio} = -\rho_b \omega_b c_b \cdot (T_b - T) + Q_{met}$$

where ρ_B is the density of blood [kg/m³], $C_{p,B}$ is the specific heat of blood [J/kg · K], ω_T is the perfusion rate of tissue, and $T_b - T$ is the temperature difference between arterial blood temperature (37 °C) and local tissue temperature in [K]. The metabolic heat generation Q_{met} is usually neglected,

as it is much smaller in magnitude than the other terms [16], [23], [26], [34], [35], [41], [43], [45], [46], [79], [80]–[82].

3.2.1.1 Joule (Resistive) Heating

Resistive losses of the tissue when exposed to RF electromagnetic energy causes heating during RF ablation. The heat flux due to EM fields is given by

$$Q_e = Q_{rh} + Q_{ml}$$

where Q_{rh} and Q_{ml} represent the resistive and magnetic heating components respectively. At frequencies of 500 kHz, the contribution of magnetic heating is negligible, thus Q_e becomes solely a function of resistive losses. This allows for a quasi-static approximation of the electrical heating. The magnitude of the resistive heating is given by

$$Q_{rh} = \frac{1}{2} R c (\vec{J} \cdot \vec{E})$$

where Q_{rh} is the distributed heat source [W], R is the universal gas constant [J/mol · K], c is the speed of light in a vacuum [m/s], \vec{J} is the current density [A/m²], and \vec{E} is the electric field [V/m]. The current density and electric field are calculated as $\vec{J} = (\sigma + j\omega\epsilon_0\epsilon_r)\vec{E} + \vec{J}_e$ and $\vec{E} = -\nabla V$, where σ is the electrical conductivity [S/m], ω is the frequency of the EM wave [Hz], $\epsilon_0\epsilon_r$ is the permittivity of free space multiplied by the relative permittivity, and V is the electrical potential. The Laplace equation is used to solve for the voltage and is given by $\nabla \cdot \sigma \nabla V = 0$. Additionally, the current through a system is solved for using the integral form of Ampere's Law $I = \oint \vec{J} \cdot d\vec{s}$.

3.2.2 Mass Transfer: Navier Stokes

The Navier-Stokes equation for an incompressible Newtonian fluid is used to solve for the velocity field in the convective heat loss term, and is defined as by the momentum and conservation of mass equations:

$$\rho \frac{\partial \vec{u}}{\partial t} + \rho \vec{u} \cdot \nabla \vec{u} = -\nabla P + \mu \nabla^2 \vec{u} + \vec{F}$$

$$\nabla \cdot \vec{u} = 0$$

where \vec{u} is the velocity field [m/s], ρ is the density of the fluid [kg/m³], $-\nabla P$ is the pressure gradient, μ is the viscosity [Pa · s], and \vec{F} is the body force due to gravity. This equation describes flow as a function of convection, gravity, pressure, and viscous drag.

3.3 Tissue Viability: The Arrhenius Damage Equation

Most models of hyperthermic therapies employ a 50 °C isotherm as the estimated lesion area, which is roughly the temperature that induces visible injury in tissue during lesion studies. In COMSOL Multiphysics®, there are two methods of time-dependent damage characterization methods: the (1) temperature-threshold, and the (2) Arrhenius damage integral. The temperature-based method specifies damage onset and necrosis temperatures, as well as an exposure time to full irreversible damage. The preset thresholds for hyperthermia ablations are coagulation at 50 °C, full necrosis at 100 °C, and the time to full damage is 50 seconds over the 50 °C threshold. The Arrhenius damage integral calculates damage as a function of energy absorption, and is based on the activation energy of the damage processes (i.e. protein coagulation) and energy absorption of the biological tissue. The equation is as follows:

$$\Omega(\tau) = \ln \left[\frac{C(0)}{C(\tau)} \right] = \int_0^\tau A e^{\left(-\frac{E}{RT(t)}\right)} dt$$

where Ω is the total damage, E is the activation energy of the target process (in this case, protein coagulation), $\frac{C(0)}{C(\tau)}$ is the fraction of undamaged tissue, R is the universal gas constant, and $T(t)$ is the temperature as a function of time. Activation energy is tissue-dependent, with the value for myocardium reported as 1.62 E 6 J/mol [88]. In both modalities, damage is computed as a fraction of necrotic tissue and is represented by the symbol Ω . Damage values run from 0 to 1, where a value of 0 represents no necrosis (i.e. 100% healthy tissue), and 1 represents total, irreversible tissue damage.

4.1 Modeling the Catheter Tip of the Test Device

For this study, a catheter tip modeled based on BioSense Webster's Navistar Thermocool® 7.5 Fr RF ablation catheter was drafted using SolidWorks® solid modeling software. The tip has a barrel diameter of 2.5 mm, and a length of 3.5 mm. This catheter model features six (6) irrigation ports, with a diameter of 0.5 mm [Figure 11].

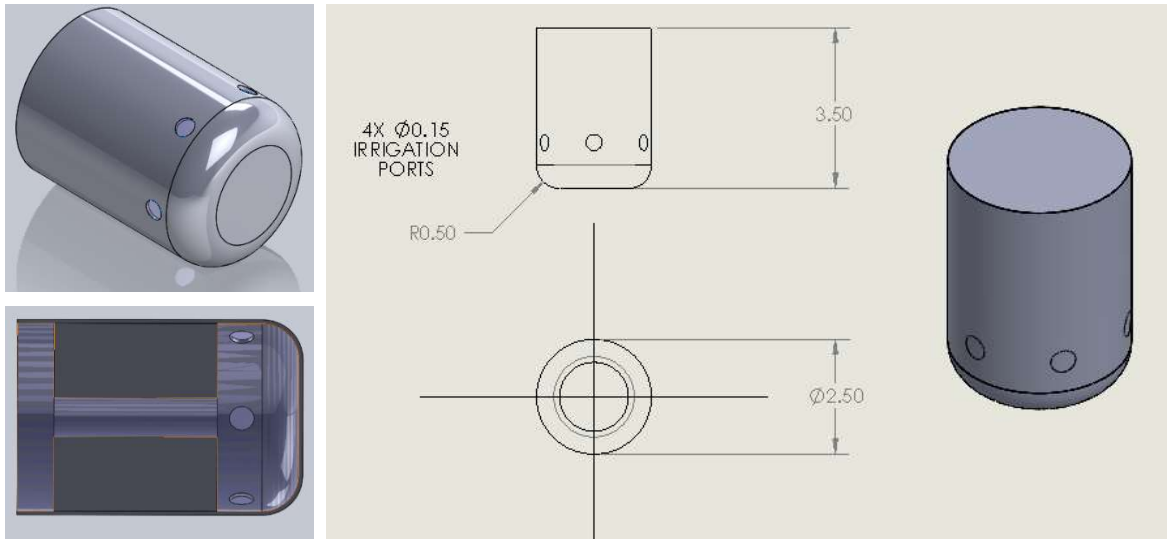


Figure 11. Model of BioSense Webster Navistar Thermocool® 7.5 Fr Ablation Catheter, Created in SolidWorks®.

To simplify the device geometry, irrigation ports and the catheter tip were modeled as surfaces rather than solid. Given enough design knowledge and a more computational resources, such detail could be included.

4.2 Physics and Material Properties Verification through Simplified Models

Several iterations of the ablation scenario with increasing geometric complexity were developed to verify the physics, boundary conditions, and material properties prior to implementation in the full left atrial anatomical model. Both the 2D and simplified 3D models consisted of a 7.5 Fr (2.5 mm OD) ablation catheter tip on a myocardial tissue block, with a blood volume above the tissue surface. Models were built with the catheter tip in a perpendicular and parallel configuration in relation to the tissue surface. For the perpendicular tip orientation, the catheter tip was inset 0.5 mm

into the tissue block with a conical depression to simulate the tissue tenting due to tip contact force. Blood flow of 0.13 m/s across this model was used to approximate the left atrial flow conditions [89].

In the 2D model, the irrigation ports were simulated with using an edge with a length of 0.5 mm, commensurate with the diameter of the irrigation ports on the chosen catheter. These ports were located 1 mm from the distal tip of the electrode. The 2D geometry and irrigation port placement are displayed in the following figure [Figure 12].

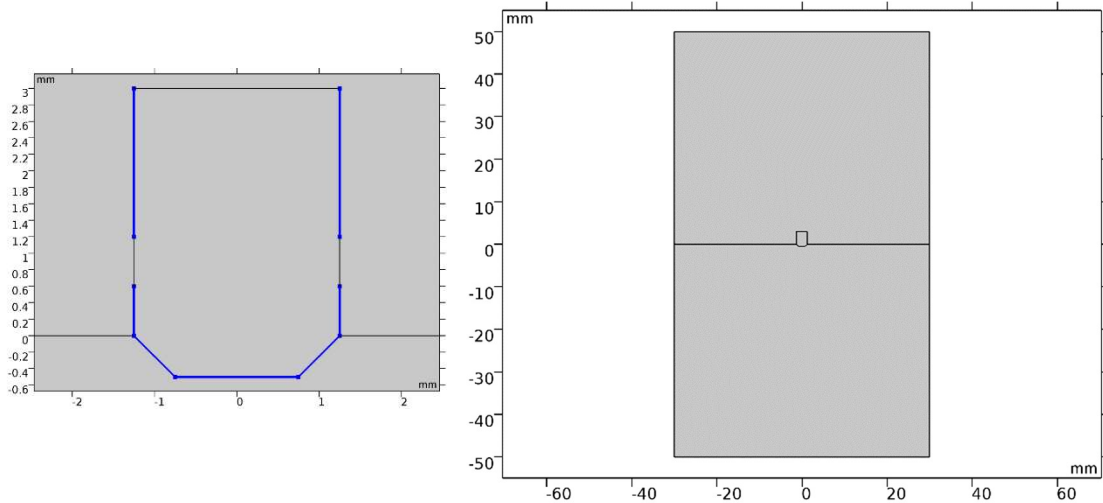


Figure 12. Geometry of 2D Model Used for Physics and Properties Verification.

Catheter tip inset at a depth of 0.5 mm. Irrigation ports modeled as line segments with a length of 0.5 mm. Tip diameter was 2.5 mm, and tip length was 3.5 mm. Catheter tip placed at interface between blood (top) and tissue (bottom) domains.

For the 3D model, an array of circular faces interspersed 60 degrees apart were propagated on the tip electrode exterior. The catheter domain was differenced off from the solution domain in the 3D model to reduce mesh sizing and solution times. Furthermore, a spherical subdomain encompassed the

catheter tip, which was used for mesh control purposes, as is described in more detail later in this chapter. Images of each simplified model are included in [Figure 13].

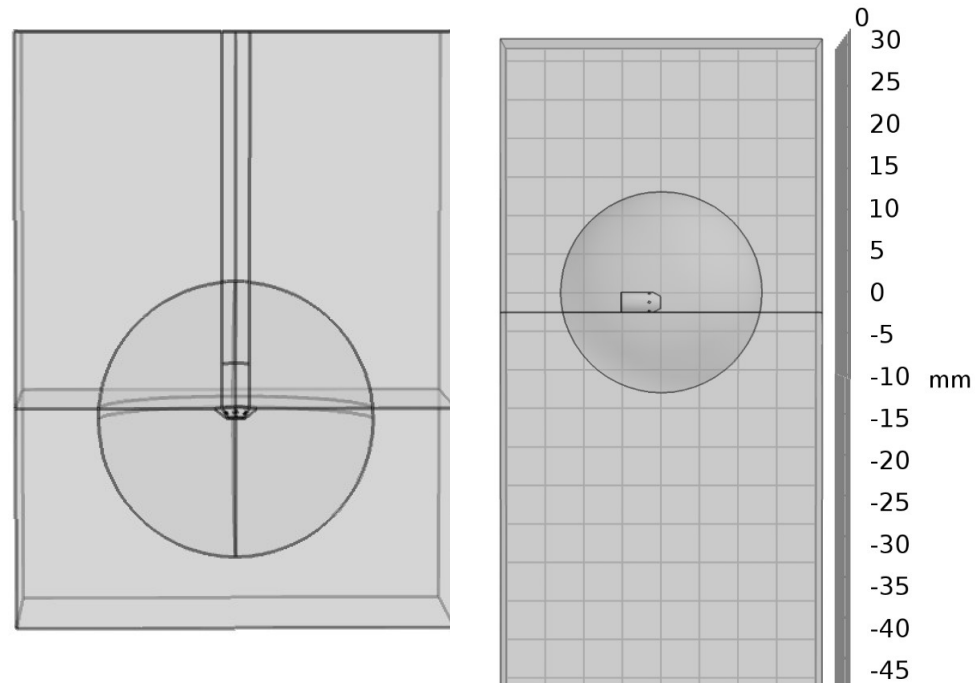


Figure 13. Simple 3D Ablation Simulation Model

Catheter tip oriented (a) perpendicular and (b) parallel to the tissue surface. The spherical subdomain allowed for custom mesh biasing. The perpendicular simulation featured a conical insertion region which mimicked tissue tenting due to contact force.

Several types of convergence studies were performed to determine appropriate sizing of the tissue block and the study region, following the practices of past models in this field. The electrical gradient in the simulated ablations was highly dependent on the separation distance between the tip electrode and the ground boundary condition due to the summed impedance of the tissue between them. Iterative simulations were performed with tissue depths from 20 – 60 mm. Of the simulation depths, 50 mm produced lesions that were closest to the maximum lesion depth of 9.3 mm reported by Moreno et al for the same ablation parameters. Images of the temperature distributions and electric field norms for each tissue thickness can be found in [Appendix A].

4.3 Left Atrial Anatomical Model Geometry

4.3.1 Left Atrial Anatomic Modeling Approaches

Models were built Fusion 360®, SolidWorks®, and COMSOL® MultiPhysics' native CAD environment, with varying degrees of morphological realism and computational suitability. Images of these early iterations of the model geometry can be found in these appendices: [Appendix B, Appendix C, Appendix D, Appendix E]. The final left atrial anatomical model was built in SolidWorks®. The primary advantages of this CAD software were easy specification and customizability of dimensions, an extensive set of primitive geometries and modeling tools, as well as the ability to define and manipulate assemblies.

4.3.2 Critical Anatomic Features of the Left Atrium

A central aspect of this thesis was in generating a more anatomically relevant left atrial anatomical geometry for testing ablation catheter tips that was compatible with COMSOL Multiphysics. Simplified left atrial geometry and procedurally relevant adjacent structures were generated using solid modeling. Dissection studies, computed tomography (CT) images, magnetic resonance imaging (MRI) stacks, and medical illustrations guided the overall morphology and positioning of the tissues.

The primary atrial features for this model included 4 pulmonary veins which inserted into the posterior wall of the left atrium, and the mitral valve annulus at the bottom end. While there are many anatomical variations of the atrio-venous junction, as depicted in [Figure 14], the configuration of four PVs is the most common type seen in humans and was included in this model.

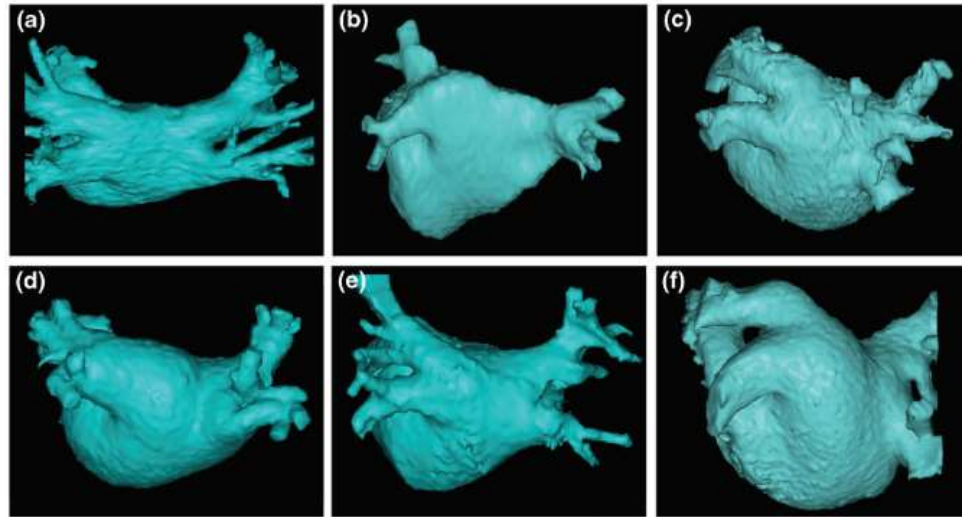


Figure 14. Posterior View of Left Atrium, Reconstructed from CT/MRI Data.

Several possible configurations of pulmonary vein entry into the left atrium. Upper left image (a) represents the most common, 4 PV branch configuration. Image credit: Calkins et al 2017 [73]. Published under the Creative Commons Attribution 4.0 International License (<http://creativecommons.org/licenses/by/4.0/>).

Furthermore, inclusion of the esophagus was deemed important to assessing procedural safety. The aorta and esophagus were approximated with hollow cylinders. All other collateral tissues were formed by differencing off these key anatomical structures from a tissue block. These collateral tissues were treated as a generic tissue volume encompassing all of the surrounding viscera. Of the regions formed by this operation, all internally confined regions were designated as blood, and all external regions were treated as a generic collateral tissue volume (a mixture of adipose, connective, and lung tissues).

The structures not included in this model were the left atrial appendage and the left lateral ridge located outside of the appendage. The appendage is a blind pouch on the anterior side of the heart which contributes greatly to thrombus risk, but in general plays a lesser role in ablative treatment of left atrial arrhythmias. Additionally, the anatomy of this appendage is highly variable and irregularly shaped [90]. The left lateral ridge marks the join between the appendage and the rest of the atrial body and is made of a thickened mass of muscle and connective tissues. This ridge is important procedurally, but it is more critical to catheter navigation and tip/tissue contact rather than

catheter tip ablation performance. Exclusion of these structures aided in reducing geometric complexity and allowed for a central plane of symmetry to be implemented.

Additionally, the major axes of the anatomical model were shifted to align with a more standard Cartesian system, with the plane used in 4 chamber echocardiography imaging used as the basis for the anterior XY plane, and the left-right PV bisecting line serving as the basis for the YZ plane. This configuration is illustrated in the figure below [Figure 15].

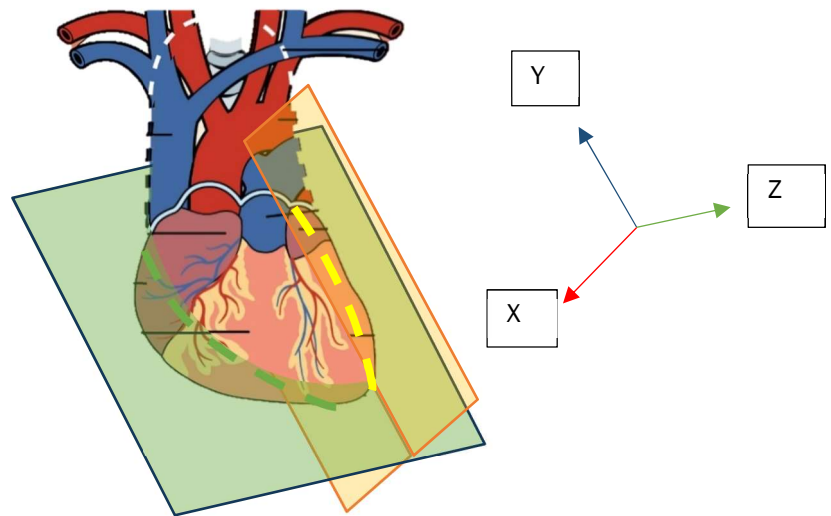


Figure 15. Planes Used to Map Left Atrial Geometry from Anatomical Positioning to a Standard XYZ Configuration.

4.3.3 Left Atrial + Adjacent Structure Dimensions

Dimensions were gleaned from studies on both living and deceased hearts. No single anatomic study captured all the dimensions needed for constructing the left atrial model. Due to the multiple sources consulted and high degree of anthropomorphic variability—as influenced by size, age, sex, concurrent pathology, and more—higher priority was given to cardiac dimensions from subjects over the age of 40 with diagnosed AF and moderate atrial enlargement. When possible, they were a compromise between the high end of female and the low end of male dimensional ranges.

Dimensions for modeling are summarized in the following tables [Table 1, 2, 3].

Table 1. Dimensions for Left Atrial Anatomy.

4CV = 4 chamber view, from echocardiographic studies. Unless otherwise indicated, values presented as means (range).

Structure	Literature Values	Sources	Value Used in Model
LA General Dimensions			
LA Major Axis (4CV)	44.0 ± 6.5 [mm]	[91]	56\m
	51 ± 10 [mm]	[92]	
Longitudinal diameter	64.2 ± 7.8 [mm]	[66]	
LA Minor Axis (4CV)	35 ± 8 [mm]	[92]	37 mm
Anterior-posterior diameter	33.1± 6.3 mm	[66]	33 mm
Atrial Wall Thickness			
Average	0.6 – 1.0 [mm] (0.5 – 5.0 [mm])	[79]	3.0 mm all around
Roof	5.0 ± 1.5 mm	[92]	
Anterior Wall	3.2 ± 1.6 [mm] 2.09 ± 0.89 [mm]	[92] [80]	
Posterior Wall	1.33 ± 1.46 [mm]	[80]	

Table 2. Dimensions for Collateral Structures Near the Left Atrium.

Structure	Literature Values	Sources	Value Used in Model
Aorta			
Diameter		[93]	3 cm
Descending	2.59 cm		
Sino-tubular junction	3.28 cm		
Wall Thickness	1.60 ± 0.22 mm	[94]	1.5 mm
Esophagus			
Diameter	15-18.5 mm	[95]	15 mm
Wall Thickness	2.11 – 4.70 mm	[95]	3 mm

Table 3. Dimensions of the Pulmonary Veins and Mitral Annulus.

Structure	Literature Values	Sources	Value Used in Model
<i>Pulmonary Veins</i>			
Wall thickness, Venoatrial junction	Carina ~ 3.2 mm Veno-atrial junction 1-1.5 mm	[66]	3.0 mm
LSPV Diameter	19.3 ± 2.5 [mm] Major: 20.6 ± 3.4 [mm] Minor: 13.3 ± 3.0 [mm] 18.4 ± 2.1 [mm]	[68] [96] [97]	Outer Diameter, all PVs: 15 mm
LIPV Diameter	17.3 ± 1.5 [mm] Major: 18.3 ± 3 Minor: 12.1 ± 2.8	[68] [96]	Inner Diameter, all PVs: 13 mm
RSPV Diameter	Major: 22.3 ± 4.4 Minor: 16.6 ± 3.9 [mm]	[72]	
RIPV Diameter	Major: 20.9 ± 4.7 Minor: 16.3 ± 3.7 [mm]	[72]	
Inter-orifice Separation	Left 1.2 - 3.4 cm Right 0.4 - 3 cm	[98]	8 mm
<i>Mitral Annulus</i>			
Major diameter	M, End Systole: 3.44 cm M, End Diastole: 3.15 cm F, End Systole: 3.11 cm F, End Diastole: 2.83 cm	[99]	Major diameter: 3 cm Minor diameter: 2 cm
Transverse Diameter, Parasternal View	2.1 ± 0.4 cm	[100]	
Horizontal Diameter, Parasternal View	2.3 ± 0.6 cm	[100]	

4.3.4 Constructing the Full Left Atrial Model

The left atrium was modeled as a revolved base, with an inner diameter of 15 mm (corresponding with ascending aorta outer diameter, and an outer diameter of 60 mm. This formed a wedge shape with an arc to arc separation of 45 mm. Successive cuts were made to roughly ‘sculpt’ the morphology of the left atrium. Edges were further shaved off with chamfers, before applying fillets with wide diameters (~5-10 mm) to round off the edges of the model. The LA body was then shelled to an inner wall thickness of 3 mm all around. This dimension is an average value of the reported ranges of wall thicknesses for the left atrium. As described in Chapter 2, the thickness of the wall varies regionally, with significant impact on procedural success in clinic. For the purposes of evaluating simple transmural, the 3 mm thickness is adequate. If further studies are performed with a greater emphasis on anatomical realism and/or collateral damage concerns, then it will be important to align the wall thicknesses with *in vivo* variations.

To model the mitral valve, an elliptical cut with a major diameter of 3 cm and a minor diameter of 2 cm was projected through the inferior aspect of the LA anterior wall. Next, two circular extruded cuts with a diameter of 13 mm were made through the superior face of the posterior wall at the approximate site of the veno-atrial junction, then mirrored across the top plane. The vertical positioning of these pulmonary veins were adjusted so that the orifices had an intermediary distance of 8 mm. An additional 15 mm circle was centered at each circular cut, and then the two profiles were swept along a curved 3D path away from the LA body to form hollow pulmonary veins.

The final model had an abundance of faces, which hindered successful meshing; therefore, several preprocessing operations were performed to prepare the model for import into COMSOL. These included merging adjacent faces on the exterior and interior of the model and eliminating any aspects that might be considered a “sharp” face or feature (i.e. anything with an angle $\ll 90$ degrees). For dimensioned drawings of the left atrial assembly, see [Figure 16; Appendix E].

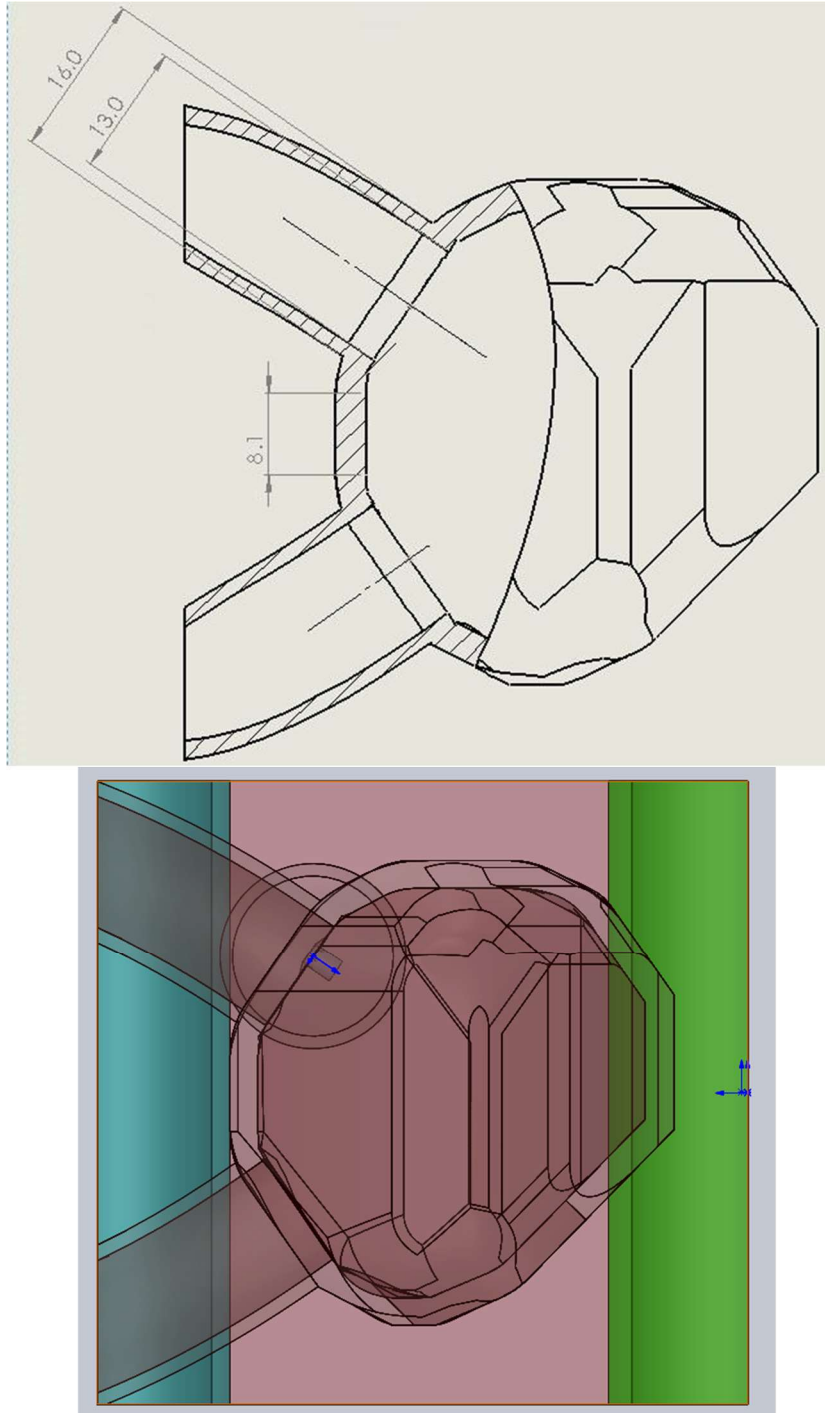


Figure 16. Side View of Atrial Model.

A) Broken Out Section depicting inter-orifice distance and pulmonary vein dimensions. B) Left atrial assembly, including esophagus (blue) and aorta (green).

Additional domains were formed in SolidWorks® by closing the openings of the LA with planar surfaces, overlaying the entire geometry with a solid block, then intersecting the two geometries. This

method was used to generate the blood volume, as well as the collateral tissue volumes. Also, hollow pipes representing the aorta (OD=30 mm / ID=27 mm) and esophagus (OD=15 mm / ID=9 mm) were modeled, then differenced off from collateral tissue block. Each part was then positioned using mating tools to form an assembly.

Due to the symmetry of the geometry, the assembly was bisected axially to enhance computational efficiency. This assembly was then exported as a Parasolid binary (.x_b) filetype, which in this particular application performed better than the STL and native SolidWorks® filetypes when importing geometry into COMSOL® Multiphysics. The following image depicts the labeled finalized geometry of the LA model space [Figure 17]. Additional views of this geometry can be found in [Appendix E, Appendix G].

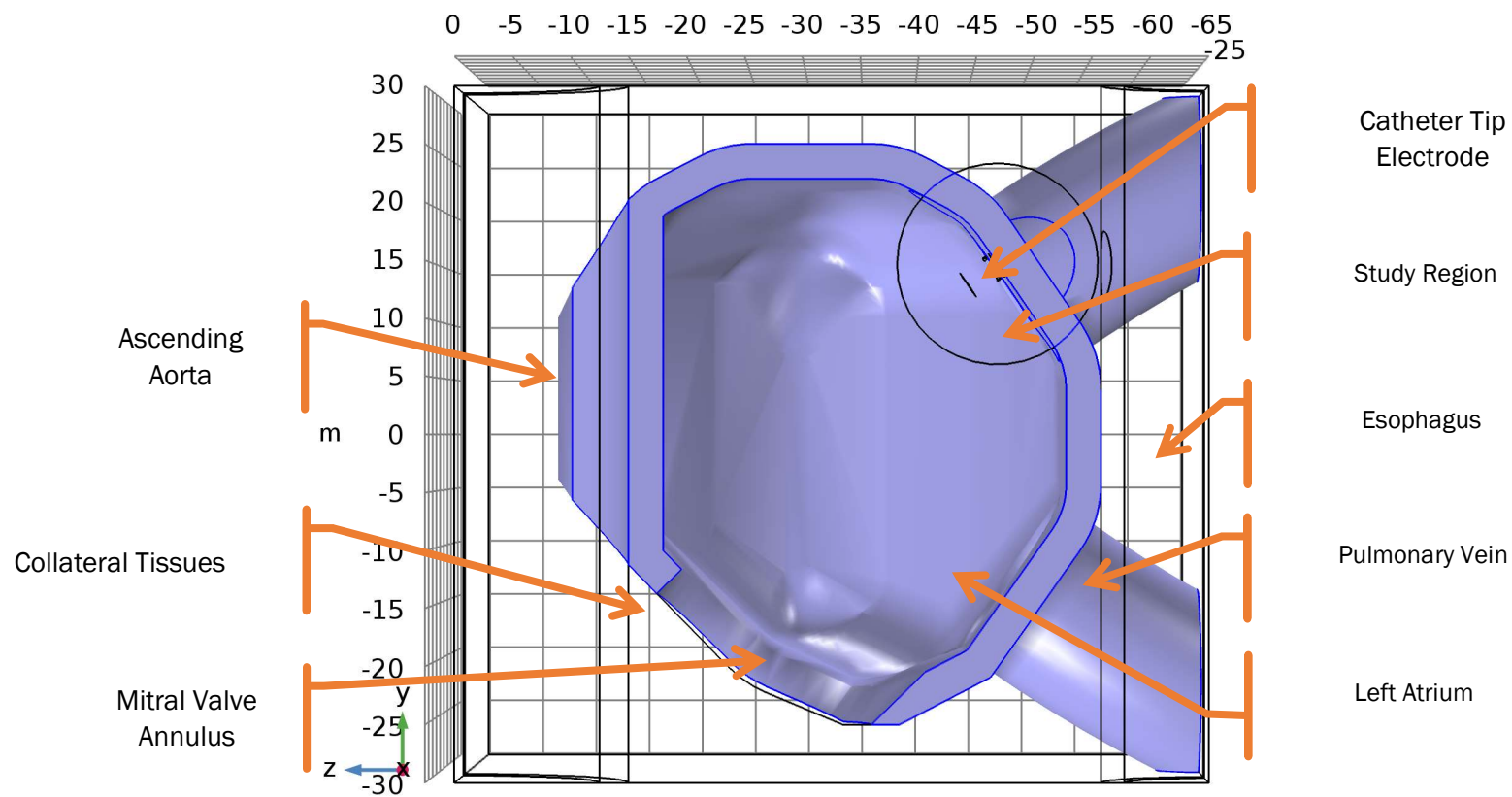


Figure 17. Left Atrial Assembly in COMSOL Multiphysics.
Left atrium highlighted in blue.

While not visible in the side views, the mitral valve annulus was capped by a planar surface which allowed for boundary condition assignment without having to model an interfacing ventricular geometry.

4.4 Physical Model Definition

The finite element analysis software COMSOL Multiphysics® was used to build the ablation simulations using the geometries. The electric currents, laminar flow, and bioheat transfer physics modules were coupled by non-isothermal flow and electromagnetic heat source multiphysics.

4.4.1 Assumptions

Several key assumptions were made when creating this ablation model:

- 1) The materials had homogenous properties.
- 2) Electrical contact between electrode and tissue was assumed to be perfect [41].
- 3) Since the wavelength of the RF energy is 500 kHz, all heating in the problem occurred through resistive heating, therefore a quasi-static approximation was applied.
- 4) Constant RMS voltage was equivalent to the average voltage output from the RF wave.
- 5) Flow in the left atrium was approximated by laminar fluid flow due to the predominantly passive flow/reservoir function of the left atrium.
- 6) Simulation of non-Newtonian blood flow was not critical for the purposes of left atrial ablation.
- 7) The pulmonary veins were approximately equidistant and had the same dimensions.
- 8) All “collateral” tissues could be approximated by general muscle properties.

4.4.2 Boundary Conditions

The following table summarizes the pertinent boundary conditions and initial values for the laminar flow, electric currents, and bioheat transfer physics, as well as the domains to which they were assigned [Table 4].

Table 4. Overview of Boundary Conditions + Initial Values of the Left Atrial Ablation Model

Physics	Domains/Boundaries	Initial Values	Boundary Conditions
Laminar Flow	Blood Saline Ports	$P_0 = 0$ [Pa] $u_0 = 0$ [m/s]	Normal inflow velocity Outlet zero pressure: $p = 0$ Pa No slip wall condition
Electric Currents	Electrode Blood Myocardium Collateral tissues	$V = 0$ [V] $E = 0$ [V/m]	Ground, posterior and inferior walls: 0 V Electrical potential on electrode: 50 V Electrical insulation on proximal tip end
Bioheat Transfer	Blood Myocardium Collateral tissues Saline	$T = 37$ [°C]	Arterial Blood Temperature: 37 °C Saline Temperature: 20 °C

The posterior and inferior walls of the tissue block were designated as ground ($V = 0$ V) to approximate the dispersive electrode, while an electrical potential was applied to the catheter tip surface. The energy output had a frequency of 500 kHz. Electrical insulation was assigned the irrigation port and proximal tip surfaces. For the thermal model, all domains were set to baseline physiologic temperature of 37 °C. The boundary electrothermal heat source was coupled. To simulate cooling by the saline irrigant, a temperature boundary condition of 20 °C was applied to all 6 irrigation ports on the catheter tip. Additionally, a temperature condition of 37 °C was placed on the pulmonary vein inlets, to simulate fresh blood flow.

While the geometry included portions of the aortal wall, the heat gradient was found to be essentially negligible in this portion of the atrium; thus, the boundary condition of lumen surface of the aorta was set to a constant 37 °C. Mass transport modeling was limited to atrial blood flow and saline irrigation. Saline flowed laminarly from the six irrigation ports at either 17 mL/min or 30 mL/min, which corresponded with a velocity of 0.06 m/s or 0.14 m/s, respectively. Based on Doppler echocardiography, an inflow velocity of 0.2 m/s was set on the pulmonary vein entrances. For this model, the ventricles and ventricular cavity were not simulated, but a zero-gage-pressure no back-flow

outlet condition was applied to the mitral valve opening to simulate the transit of oxygenated blood from the left atrium to the ventricle. The development of flow was then solved for by COMSOL. Additionally, a Point Pressure Initial Condition which assigned a 0 Pa gage pressure was applied to a point on the mitral valve opening. While this seemed redundant given the mitral valve boundary condition, the “priming” of the solution space for the Navier-Stokes was necessary to converge on a solution.

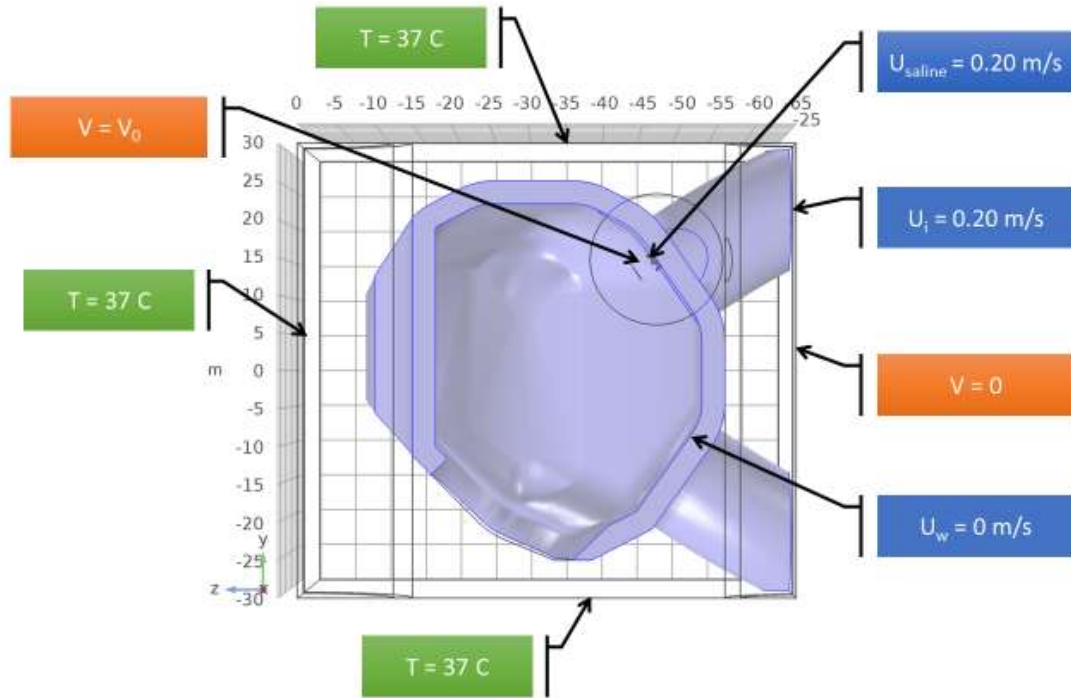


Figure 18. Boundary Conditions of Full Left Atrial Model Space.

4.5 Material Properties

The table below summarizes the material properties referenced, separated by material domains. For images depicting each material domain, see [Appendix G].

Table 5. Thermal and Electrical Material Properties, Temperature Independent.

* indicates properties with a potential temperature-dependent variant.

Parameter	Value	Units	Source
Myocardium			
Density	1060	kg/m ³	[45]
Thermal conductivity	0.531	W/(m·K)	[101]
Electrical conductivity*	0.6	S/m	[102]
Relative permittivity	3260		[103]
Specific heat	3111	J/(kg·K)	[45]
Perfusion	0.0064	1/s	[104]
Blood			
Density*	1060		[45]
Thermal conductivity	0.5 [W/m·K]	W/(m·K)	[101]
Electrical conductivity*	0.667 [S/m]		[102]
Relative permittivity	1800		[45]
Specific heat	3900	J/(g·K)	[105]
Dynamic viscosity	0.00345	Pa s	[104]
Generic Muscle			
Density	1060	kg/m ³	[108]
Thermal conductivity	0.642	W/(m·K)	[104]
Electrical conductivity*	0.446	S/m	[102]
Relative Permittivity	3650		[103]
Specific heat	3.72	J/(g·K)	[105]
Perfusion	0.0015	1/s	[101]

While not studied fully in this model, the electrical conductivity of tissues is strongly influenced by temperature, and could be implemented via a piecewise function, interpolation of tabulated values, or an analytical function tied to the property variable in COMSOL Multiphysics®.

4.6 Mesh Development

Several meshing strategies were implemented to improve element quality while minimizing the degrees of freedom needed to generate stable solutions. These included geometric subdivisions, mesh element sizing convergence, biasing evaluations, and element quality assessment.

4.6.1 Geometry Subdivisions

The geometry of the 3D models was divided using a spherical subdomain centered on the catheter to provide more control on mesh propagation and concentrate mesh biasing. To select the optimal diameter for this spherical subdivision—henceforth referred to as the region of interest (ROI)—convergence testing was performed on the small ablation model. A 50 V constant potential was applied to the electrode for a treatment time of 60 seconds. Three-dimensional isotherms were plotted to highlight the transition zone from 37.1 °C to the basal body temperature of 37 °C, as depicted in [Figure 19].

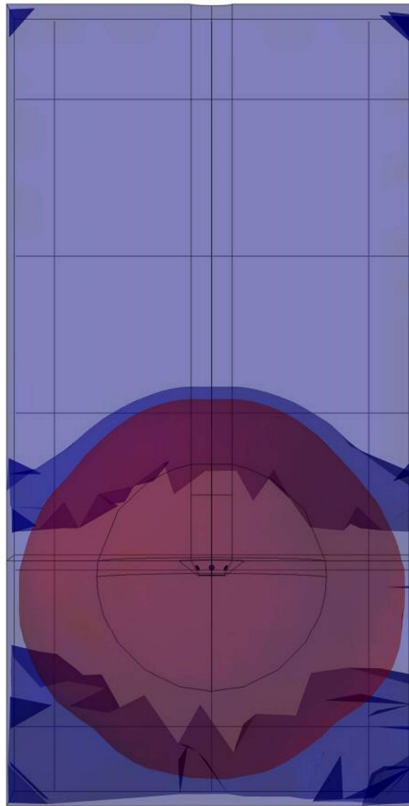


Figure 19. 37 °C and 37.1 °C Isotherms to Determine Ideal Study Region Diameter.
Constant voltage ablation for 60 s, no blood flow or saline irrigation.

For the simplified 3D model, the initial 4x4 cm tissue/blood column proved to be an insufficiently large study space; therefore, iterative simulations were performed with progressively larger study regions until there were no boundary effects. Boundary effects were identified by observed distortion and flattening of the 37.1 °C isotherm parallel to the adjacent tissue/blood domain boundaries. This assessment was done with no blood flow to provide the “worst case” (i.e. largest extent) scenario for the subdivision. The ultimate spherical radius was set at 10% larger than the diameter of the 37.1 °C isotherm, which corresponded with a radius of 1.4 cm. This diameter was then applied to both 3D models.

4.6.2 Study Region Convergence

The use of the spherical subdivision helped to reduce solution times and degrees of freedom. Areas of the simulation geometry outside of the spherical domain were set to large element sizes (max 15 mm), with up to 1.25x adjacent element size propagation. More gradual mesh biasing was applied in the ROI for blood and tissue, at a rate of 1.15x per layer of elements.

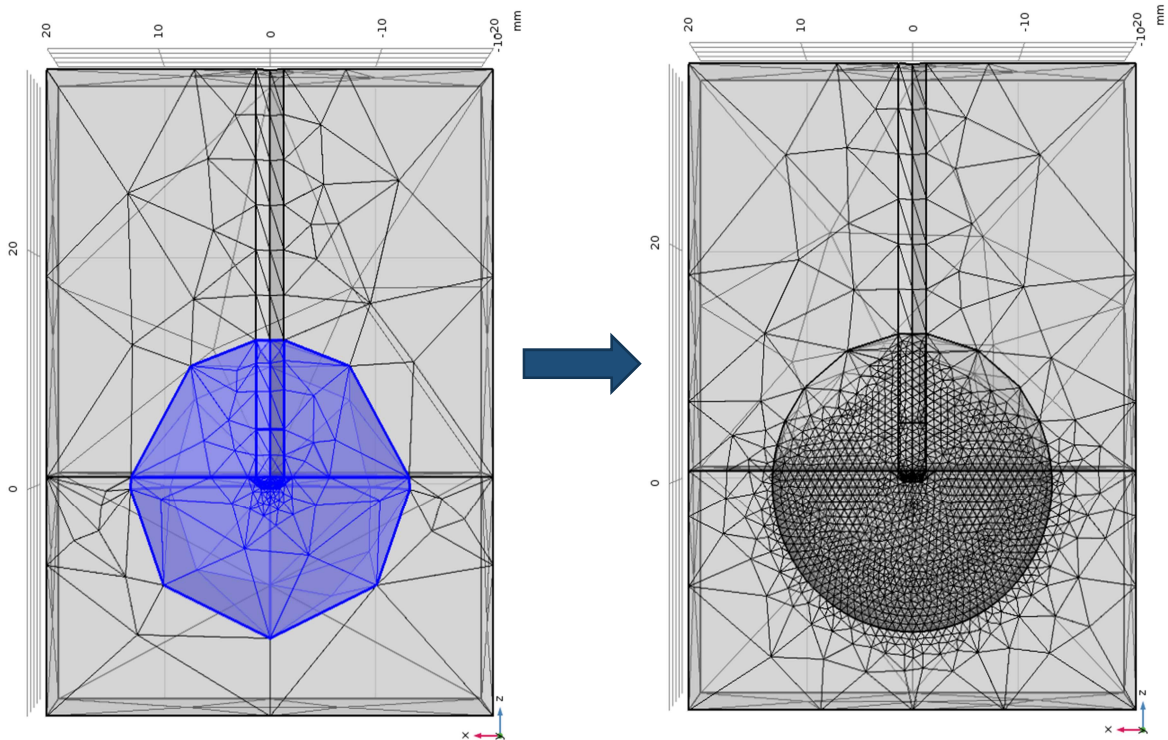


Figure 20. Element Size Convergence Studies.

Progressively finer meshes evaluated to determine minimum element sizing for optimum computational efficiency. Convergence performed on spherical study region in small model. Converged dimensions from small model applied to study region in full atrial model.

The governing rules for element sizing were that max ROI was less than or equal to the minimum ROI dimension, and that the max ROI dimension served as the minimum dimension of the coarsely meshed tissue and blood regions. Dimensions between 0.01 and 100 mm were tested. The dimension combinations tested are depicted on the graph below [Figure 21].

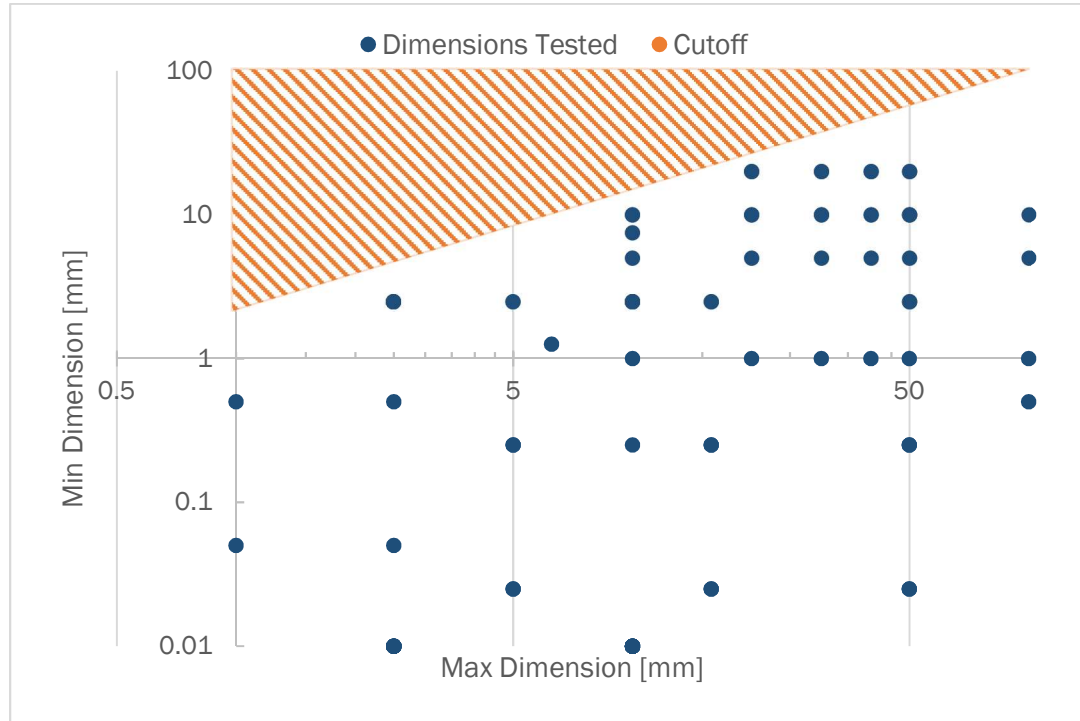


Figure 21. Dimension Combinations from Element Sizing Convergence Studies.

Axes values on logarithmic scale. Cutoff represents combinations outside of the search space (i.e. Min > Max).

To evaluate the impact of mesh size on solution stability, domain and point probes were defined to sample maximum temperatures in the blood and tissue domains, as well as tissue temperature as a function of distance from the tissue/electrode interface. Temperature was tracked from the interface temperature to 6 mm below, in steps of 1 mm. In addition to element size combinations, degrees of freedom were tracked for each simulation.

The percent difference in 60 second temperature values was calculated by dividing the difference in temperatures by the temperature associated with the lower degree of freedom simulation, as shown by the following equation.

$$\% \text{ Difference} = \frac{T_n - T_{n-1}}{T_{n-1}}$$

Mesheres were considered converged when there was <0.25% deviation in any of the measured temperature values for the sampled tissue depths. Degrees of freedom were plotted against 60 second temperature deviations between sampled values to monitor for convergence [Figure 22].

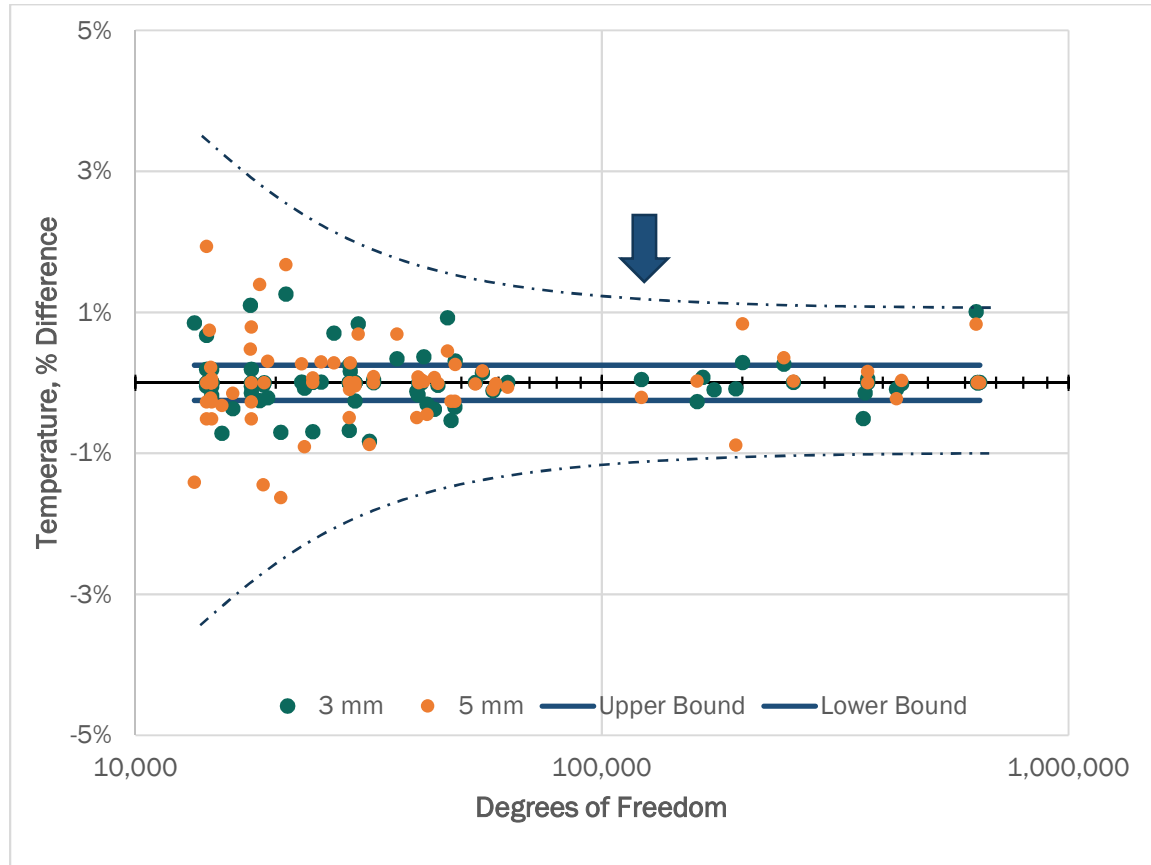


Figure 22. Mesh Convergence Plot: % Difference in Temperature at Tissue Depths of 3- and 5-mm vs the Degrees of Freedom in the Solution.

The parallel bars on the graph represent the $\pm 0.25\%$ bounds for convergence. The dashed lines highlight overall funneling trend of datapoints with an increase of degrees of freedom.

The plot suggests that the deviation in temperature response due to degree of freedom roughly converged within $\pm 1\%$ above 121,000. While it is possible that a finer mesh could reach a smoother convergence, run times (>6 hours) and RAM limits (16 GB) made models with mesh elements smaller than 0.01 mm impractical to run. Furthermore, since convergence was done on the simplified 3D model, the increased size and complexity of the full atrial model would make the use of this element size even more unfeasible. Therefore, to narrow down potential size combinations, a filter on minimum tissue element quality, as measured by skewness, was set at 0.20 or higher. The set of dimensions associated with a DOF greater than 121,000 that produced an acceptable element quality

was a max length of 1 mm and a min length of 0.05 mm. Mesh configurations for all domains are depicted in [Figures 23 and 24].

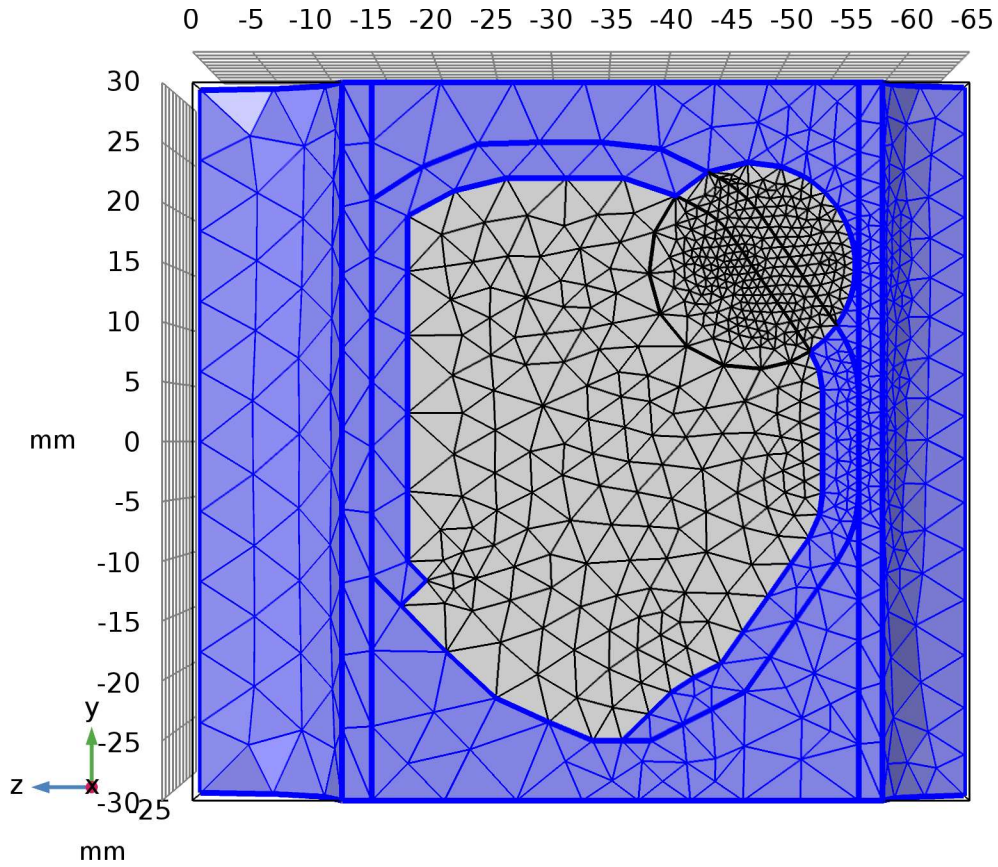


Figure 23. Mesh Tissue Domains (Blue) and Blood Domain (Grey) in Full Model,
General tissue domain has max element size: 7.26; minimum element size: 15; Curvature Factor 0.6;
Resolution of narrow regions: 0.5; Maximum element growth rate: 1.25. Max element size: 3.5 mm;
min element size: 0.05; Curvature Factor: 0.5; Resolution of Narrow Regions: 0.7; Maximum element
growth rate: 1.25.

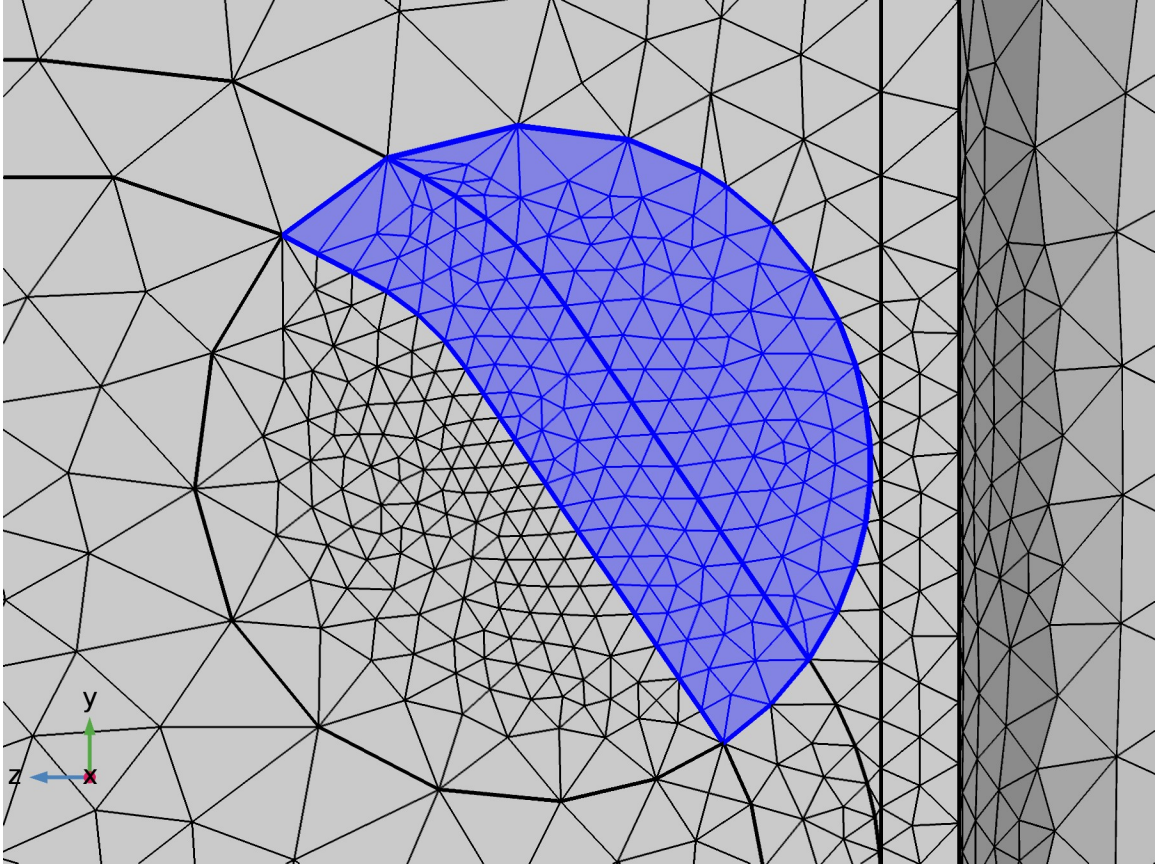


Figure 24. Tetrahedral Mesh on Tissue (Blue) and Blood (Grey) Spherical Study Regions.
 For tissue study region (blue), max element size: 15; min element size: 0.05; Curvature factor: 0.75; Resolution of narrow regions: 0.75; max element growth rate: 1.15. For blood study region (grey half circle), max element size: 15; min element size: 0.05; Curvature factor: 0.75; Resolution of narrow regions: 0.75; Max element growth rate: 1.15.

COMSOL Multiphysics® balances model physics and the user's mesh parameter definitions when generating meshes for a domain. Interestingly, while both tissue and blood ROI's were assigned the same element size growth rate (1.15), there was much a larger and more drastic growth of element sizes on the blood region compared with the tissue ROI, which barely changed from the finest region (i.e. near the blood/tissue interface) to the edges of the ROI adjacent to the esophagus.

The finalized mesh of all regions resulted in 965,160 degrees of freedom (DOF) when solving for the perpendicularly-oriented electrode, with temperature independent properties and saline/blood flow inclusion.

4.6.3 Element Quality Observations

Distribution of element quality was also analyzed graphically, with a color scale representing average element quality plotted per element. Element quality is important to the accuracy of the solution and is tied to the underlying theory of finite element analysis (i.e. Galerkin's Approximation Method). Briefly, the problem is modeled mathematically as a second order integral which includes an approximate solution and test functions governed by the physical conditions. Defining the problem in this way, after some derivation, leads to an approximately linear form of the solution, where the resultant "forces" are a result of the "displacements" multiplied by the "stiffness matrix. Solution of the problem requires integration of these functions at each node to form the stiffness matrix for a single element, while intermediate behavior is extrapolated through the element. Therefore, excessive element distortion leads to issues in the formation of the stiffness matrices for each element, which in turn leads to lower solution accuracy.

Overall element quality for the left atrial assembly was 0.6430. Elements with higher element quality were labeled in green, and elements with lower element quality were labeled in red. Based on the color distribution within the model, average element quality was 0.5 or higher within the study region, as shown in [Figure 25].

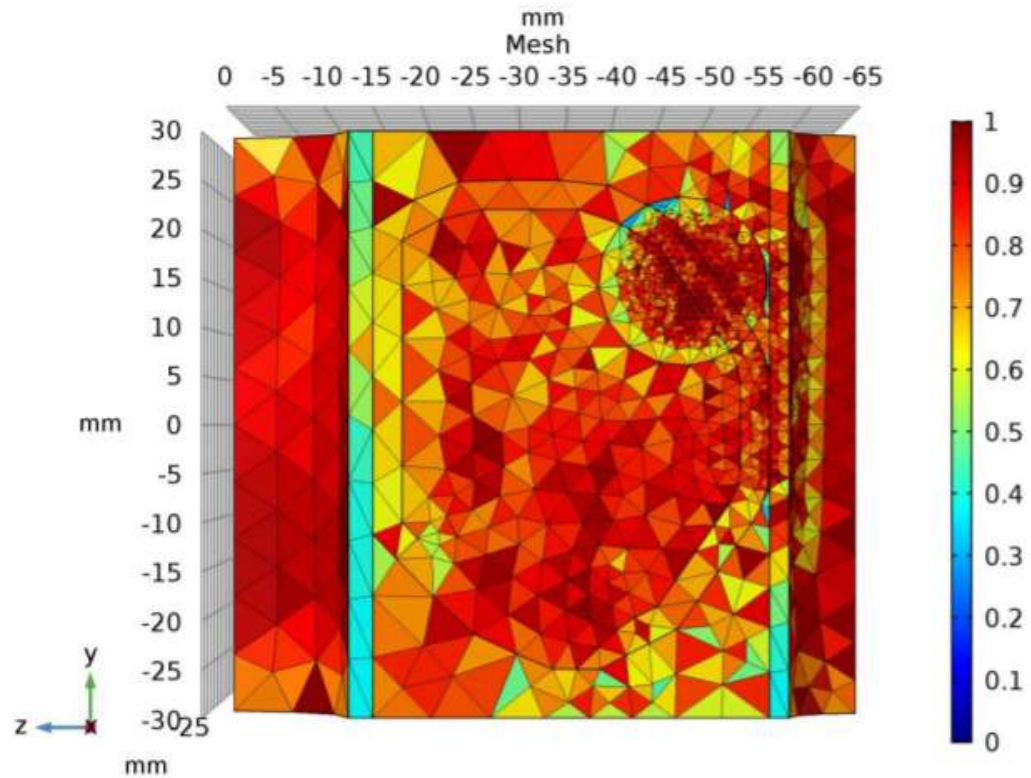


Figure 25. Element Quality Plot, Medial View of Bisected Left Atrial Anatomy.

Structures visible include the aorta (left), left atrium (center), esophagus (right), ROI, blood, and the generic surrounding tissue volume. Element quality was plotted on a rainbow color scale, with better quality elements in red and lower quality elements in blue.

Areas of particularly low quality were the external faces of the aorta and esophagus. This was due to the discrepancy between external element faces, and the interstitial element faces, where the wall thickness dimension was much smaller than the external surface element dimensions, as shown in the following image [Figure 26].

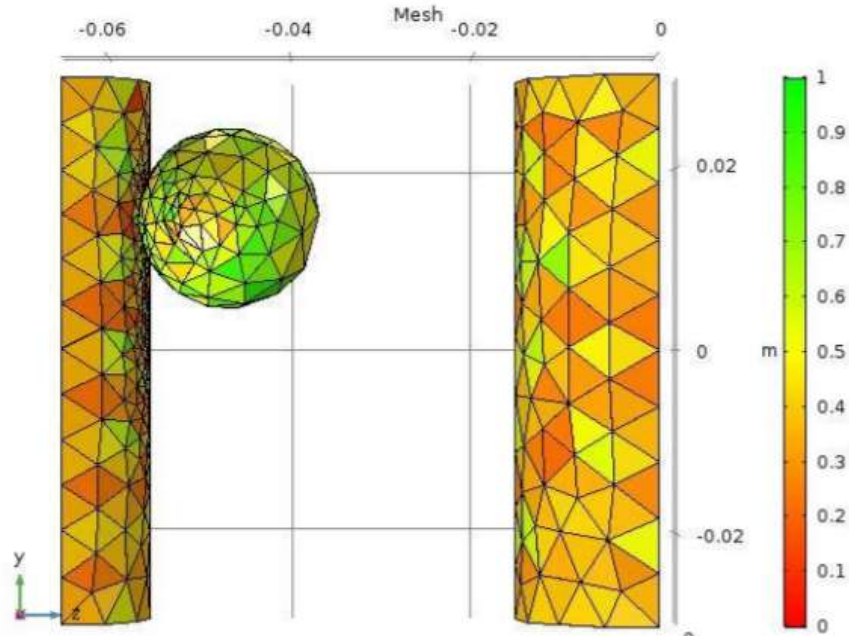


Figure 26. Element Quality Plots of Aorta, Region of Interest, and Esophagus.

Mesh elements shaded by quality—as determined by skewness, with higher element quality in green and lower element quality in red. Lateral view of simulation space. Tissue, atrium, and blood hidden to highlight the aorta (right), region of interest (sphere), and the esophagus (left).

As only 1 layer of tetrahedral elements were used to construct the esophageal and aortic meshes, this resulted in flattened tetrahedrons, like the ones modeled below [Figure 27].



Figure 27. Equilateral Tetrahedral Element (Left) Versus Flattened Tetrahedral Element (Right).

These structures were not critical to the objectives of this model but could be rectified with smaller element sizing if tracking the heating and damage of the aorta or esophagus was a priority.

4.7 Time Discretization

By default, time stepping values in COMSOL Multiphysics® are governed by a Backward Differentiation Formula (BDF) solver, which uses a range of time steps based on the dynamics of the problem. For each time step, the largest possible increment was determined by the solver. A sample

plot of the time-dependent solver timestep convergence is included below [Figure 28].

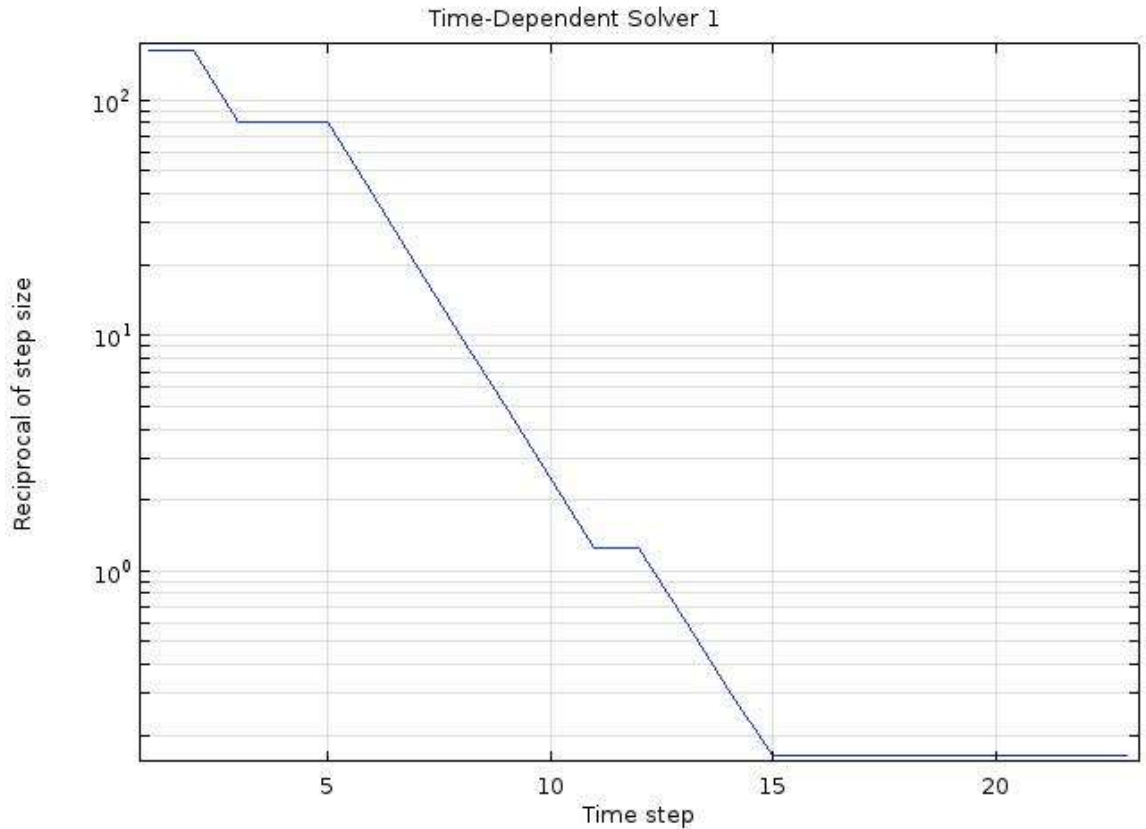


Figure 28. Convergence Plot of Time Dependent Solver.

Step size selected by Backward Differentiation Formula. Time step size determined based on time-dependent dynamics of the simulation. Maximum time step: $1/1 = 1$ second; minimum time step: $1/10^3 = 0.001$ second.

During simulations of the small and full models, time steps tended to fall between 0.001 and 1 seconds. To limit the solution space—which in some cases limited the solution time—the lower bound was set to 0.001 s. Additionally, a stricter BDF condition was applied such that the solver had to take at least one time step on the sampling interval of 0.1 s (from the solution interval 0:0.1:60 seconds).

4.8 FEM Analysis Steps

The coupled electrical-thermal-mass transport problem was solved using two study formulations. The study steps defined which equation form and which solver was used to derive the solution.

4.8.1 Step 1: Stationary Study

While the flow through the atrium is not perfectly laminar, it is sufficiently non-turbulent and passive that it can be approximated with a laminar flow. With consideration for computational limitations, the flow solution was generated using a stationary solution method, then used to propagate heat in later solution steps. Flow was solved for directly using the PARADISO stationary solver.

4.8.2 Step 2: Frequency Transient Study

The frequency transient solution step was used to solve for the electric field due to the ablation process. Heat transfer was also solved for during this step, integrating the flow fields of blood with the electrical heating of the electrode and perfusion of the cardiac tissue. This was computed with an iterative Geometric Multigrid solver.

4.9 Validation Case Study

To validate the model, the lesion dimensions and temperature profiles from the simulation were compared with in-vivo lesion studies using the Biosense Webster Thermocool RF catheter. In the validation case study, lesion data was generated using power-controlled 30W ablations for 60s in anesthetized adult pigs. The Thermocool catheter was irrigated with 17 mL/min of heparinized saline (1000 U/L). Parameters of the ablations are summarized in the table below [Table 6].

Table 6. Biosense Webster Thermocool Ablation Procedural Parameters for In-Vivo 30W/60 sec Ablations in Porcine Models. From Moreno et al 2014 [109]

Input Parameter	Units	Value
Voltage [V]	V	48.3 ± 2.6
Current [mA]	mA	619.4 ± 11.9
Power [W]	W	29.5 ± 0.4
Perpendicular Ablation Results		
Max Diameter	mm	10.3 ± 1.5
Depth Max Diameter	mm	3.6 ± 0.6
Depth	mm	9.3 ± 1.4
Volume	mm ³	555 ± 151
Tangential Ablation Results		
Max Diameter	mm	10.1 ± 1.6
Depth Max Diameter	mm	3.0 ± 0.8
Depth	mm	8.1 ± 1.8
Volume	mm ³	530 ± 128

Power output was approximated by a voltage of 50 V to the electrode surface using the terminal boundary condition. The terminal is a boundary condition in the AC/DC module of COMSOL Multiphysics® that allows the user to model voltage, current, and power sources. It can be used to model such things as current- or voltage-limited power supplies, or as a means of interfacing a circuit (e.g. one built in MatLab®) to the Multiphysics model. In addition, a saline irrigation rate of 17 mL/min applied across the 6 ports (equivalent to a normal velocity of 0.06 m/s at each port). Ablations were then performed for 60 seconds, and max depth and diameters were recorded for the perpendicular and tangential electrode orientations.

4.10 Damage Evaluation Methods

As described in Chapter 3, there are two methods of damage evaluation available in the COMSOL Bioheat module: (1) temperature threshold, and (2) Arrhenius damage integral based. In both modalities, damage is computed as a fraction of necrotic tissue and is represented by the symbol Ω . Damage values run from 0 to 1, where 1 represents total, irreversible damage. Both damage criteria were evaluated in a 2D ablation model to select which would be used for lesion measurement in further studies. When compared against the commonly-used 50 °C isotherm—the temperature of tissue protein coagulation—the Arrhenius damage formulation for myocardium estimated a smaller lesion than the temperature-based method, as shown on the following page [Figure 29].

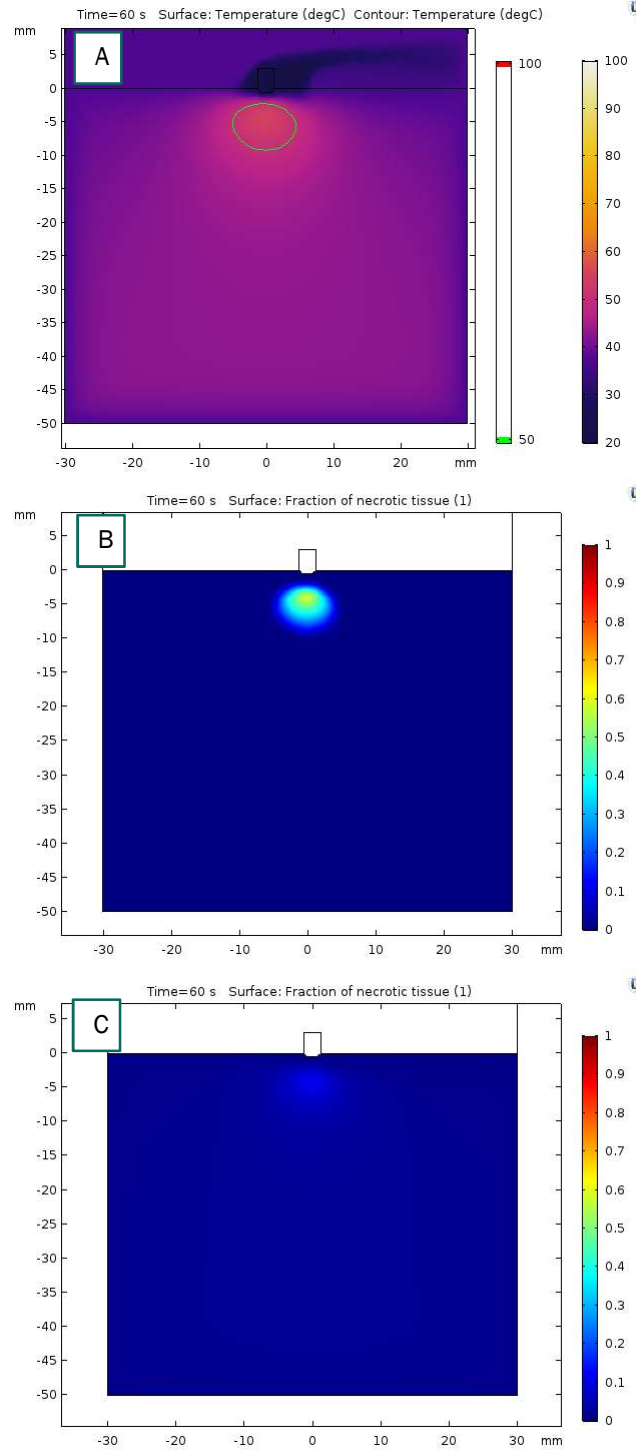


Figure 29. Comparison of Damage Criteria for Lesion Measurement in Ablation Studies. Damage determined by A) standard 50 °C isotherm, B) temperature threshold-based damage, or C) Arrhenius damage integral. Parameters for the Arrhenius damage integral tailored for myocardium: $A = 3.0 \times 10^3$ [Hz], $E_a = 1.62 \times 10^5$ [J/mol]).

The lesion defined by the temperature-threshold criteria more closely matched the experimental validation case dimensions. Damage evolution as calculated by the COMSOL solver is included as a

step during segregated solution of the bioheat equation; this leads to longer solution times. Since the temperature-threshold lesion was essentially the same as the 50 °C isotherm for this ablation case, both COMSOL-based evaluations of damage for lesions were not considered in further studies.

Should use of the Arrhenius damage integral be applied in later versions of this testbed, optimal values for activation energy would need to be determined. cursory parametric studies on the activation energy suggested that the myocardial activation energy would need to be lower to achieve similar results to the validation case study [Appendix J].

5.1 Multiphysics Verification with Simplified Models

Perpendicular and tangential ablations were performed in a 2D and simplified 3D model to verify the researched physics, materials properties, and boundary conditions. Morphology, temperature distributions, and lesion size were compared against similar ablation parameters as an *in vivo* experimental study [109]. Once successful physics implementation could be achieved, the bioheat model could then be applied in the full atrial model. Overall, the morphology of the lesions produced in these simplified models matched typical ellipsoid morphology for monopolar RF ablations [Figure31, Figure32].

Interestingly, the 3D models reached higher temperatures near the electrode-tissue interface yet produced relatively equivalent lesion depths (6.8 vs 6.9 mm and 7.6 vs 7.1 mm for perpendicular and tangential, respectively). Lesion dimensions from these initial as summarize and compared against the Moreno et al [109] lesion study in the table below [Table 7].

Table 7. Lesion Dimensions from Verification Studies in 2D and Simple 3D Ablation Models.

	Max Depth	% Difference	Max Diameter	% Difference
Perpendicular Ablations				
Moreno et al	9.3 ± 1.4	—	10.3 ± 1.5	—
2D Model	6.8	-26.9%	9.4	-8.7%
Simple 3D Model	6.9	-25.8%	11.4	+10.7%
Tangential Ablations				
Moreno et al	8.1±1.8	—	10.1±1.6	—
2D Model	7.6	-6.2%	10.7	+5.9%
Simple 3D Model	7.1	-12.3%	12.5	+23.8%

Percent difference in means ranged from 5.9 – 26.9%; however, apart from the perpendicular ablation max depths, all measured lesion dimensions fell within the spread the experimental values.

Additional simulations examined the effect of blood flow, saline irrigation, and temperature-dependent properties on ablation performance. Images and more in-depth description of these aspects are located in [Appendix H].

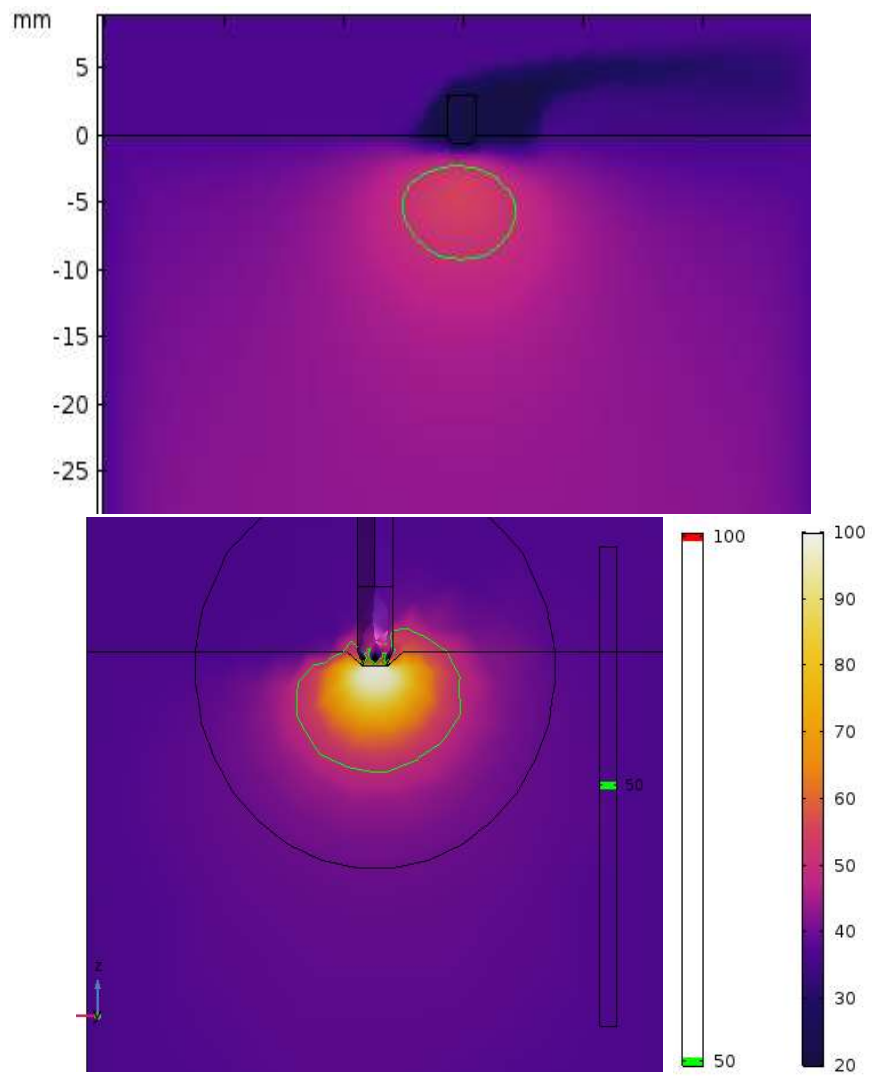


Figure 30. Temperature Distribution and Lesion Isotherms of Perpendicular Electrode Orientation Ablations in the 2D (Top) and Simplified 3D (Bottom) Models
 Images aligned to match length scales.

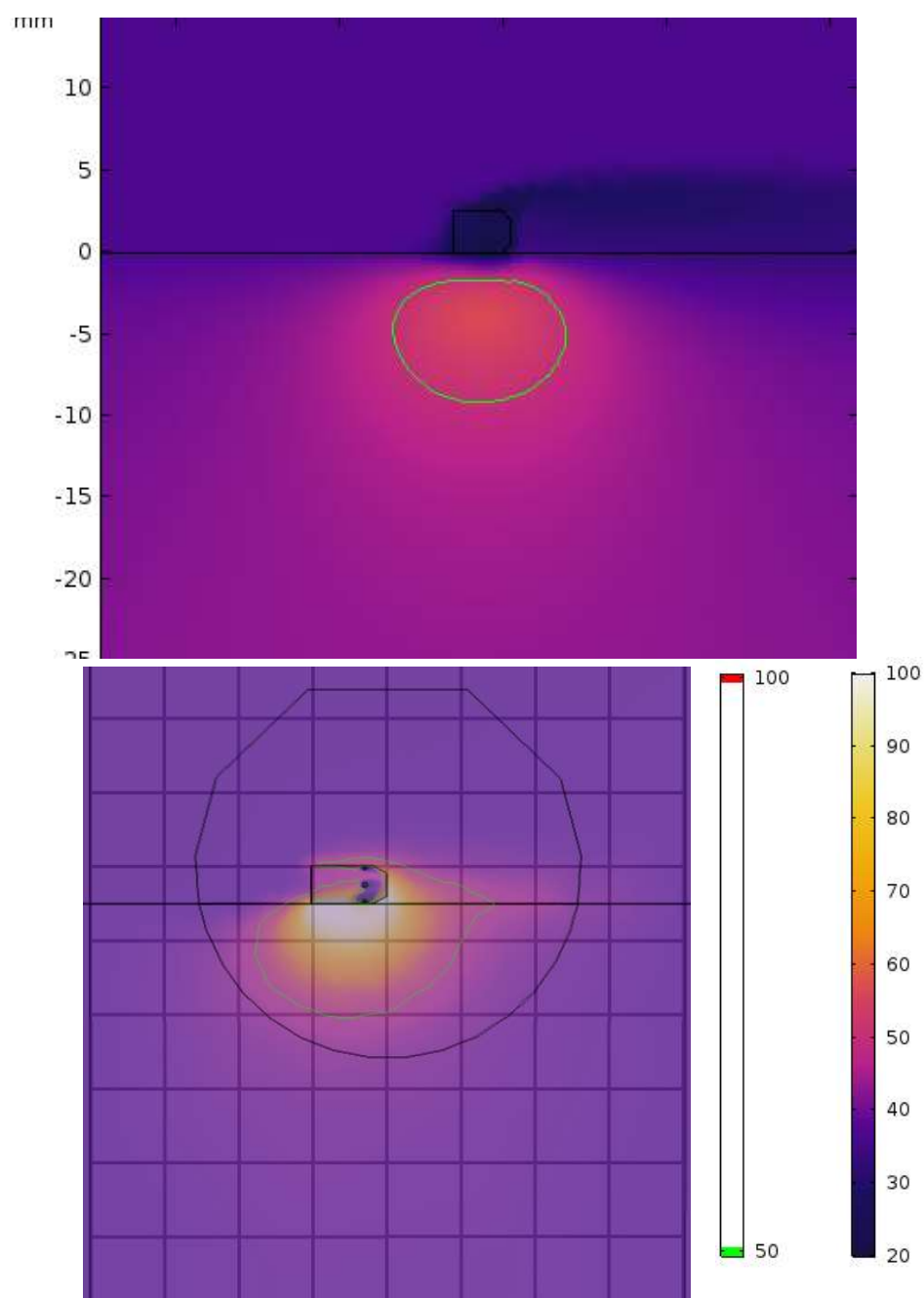


Figure 31. Temperature Distribution and Lesion Isotherms After 60 Second Ablation With a Tangentially Oriented Electrode for the 2D (Top) and Simplified 3D (Bottom) Preliminary Simulations.

5.2 Initial Simulations + Modifications to the Full Atrial Model

Aortal blood flow was originally included in the simulations of the left atrial model; however, based on the chosen location of the ablation site in this particular simulation, the aorta was far enough away and the blood velocity high enough that the thermal effect could be approximated by a 37 °C boundary condition.

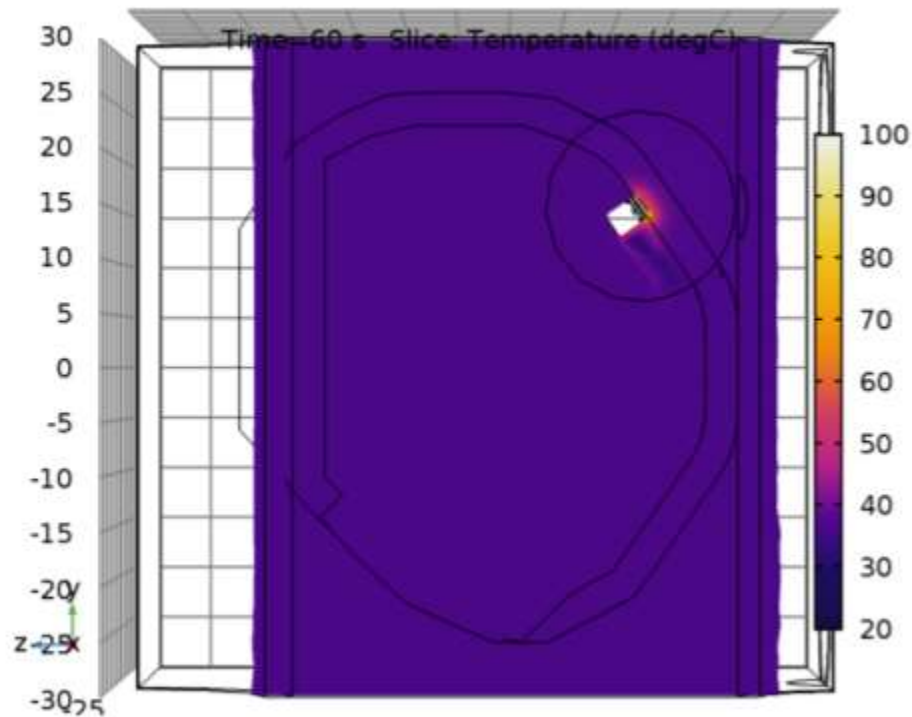


Figure 32. Temperature Plot, Medial View of Left Atrium Assembly.

While the focus of this geometry was in providing locations around the PV ostium for ablation, if other treatments are trialed and/or the geometry is modified, the aortal flow might become a significant heat sink. Thus, this 37 °C boundary condition would need to be re-evaluated on a case-by-case basis.

5.3 Full Atrial Model vs Validation Case Lesion Comparison

Ablations performed in the left atrial model with a constant voltage of 50 V, saline irrigation of 17 mL/min, and cooling due to blood flow and tissue perfusion resulted in ellipsoid lesions with surface diameters slightly larger than the electrode tip [Figure 33].

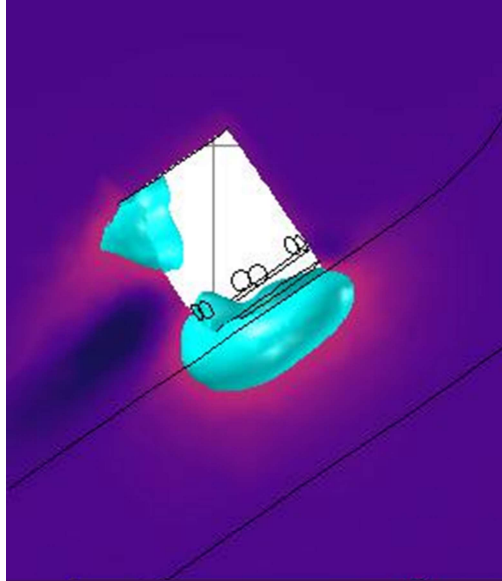


Figure 33. Lesion Morphology of 50 V, 60 s Ablation, Perpendicular Electrode Orientation. The 50 °C isotherm is highlighted in cyan. Color gradient indicates temperature distributions below 50 °C, with lighter pink indicating higher temperatures and darker purple indicating lower temperatures (~20 °C).

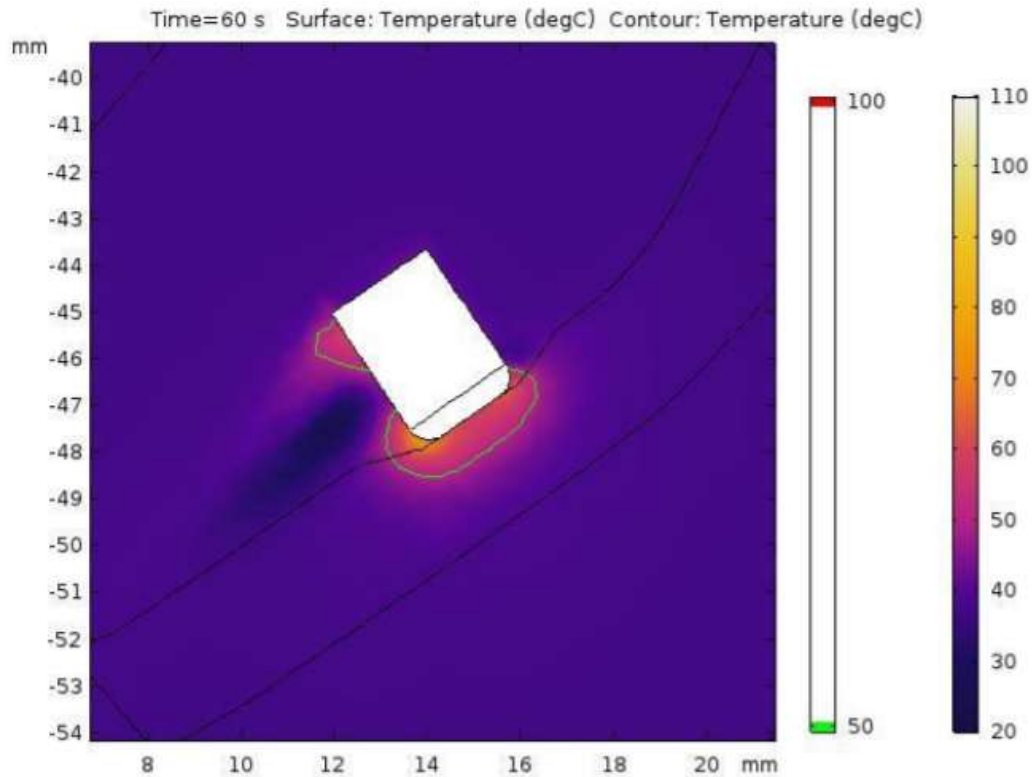


Figure 34. Temperature Distribution Following a 50 V, 60 Second Ablation, With Electrode Tip Oriented Perpendicularly to the Myocardial Surface.

Maximum lesion depth for this ablation was 0.8 mm, and maximum lesion diameter was 3.4 mm, as is summarized in the following table [Table 8]. Compared with the validation case, this represented a 91.3 and 70.0% difference, respectively.

The tangentially oriented electrode ablation produced lesion values much closer to those found in the validation study, as shown in the following image [Figure 35]. The max depth and max diameter were 5.8 and 10.9 mm respectively, which corresponded with a percent difference of -28.4% and 7.9% from the reported values by Moreno et al 2014 [109].

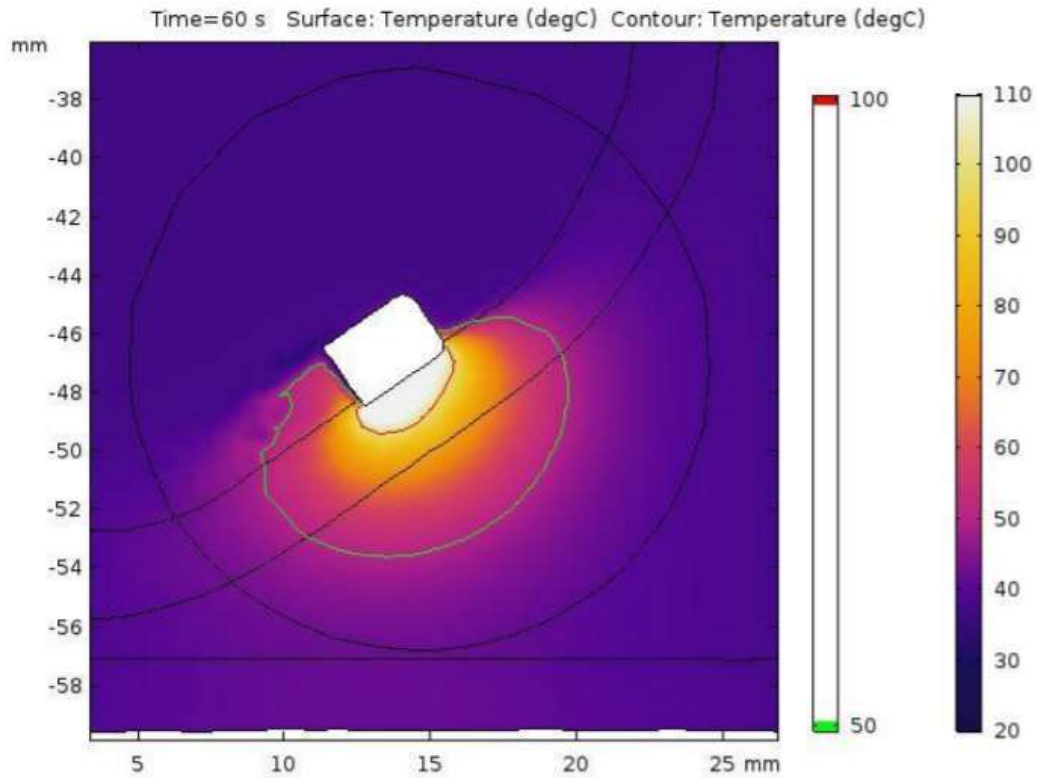


Figure 35. Temperature Distribution Following a 50 V, 60 Second Ablation, With Electrode Tip Oriented Tangentially to the Myocardial Surface.

Table 8. Comparison of Lesion Dimensions from Left Atrial Simulations and Experimental Lesion Studies.

	Max Depth [mm]	% Difference	Max Diameter [mm]	% Difference
Perpendicular Ablations				
Moreno et al	9.3 ± 1.4	---	10.3 ± 1.5	---
3D Left Atrial Model	0.8	91.3%	3.4	70.0%
Tangential Ablations				
Moreno et al	8.1±1.8	---	10.1±1.6	---
3D Left Atrial Model	5.8	-28.4%	10.9	7.9%

5.4 Diagnostics to Determine Root Cause of Perpendicular Lesion Size Discrepancy

5.4.1 Flow Velocity Distribution in the Full Atrial Model

In the simple case of the rectangular model, though, flow path and velocity did not change substantially within the simulated blood volume. Outflow in this case was normal to the outlet boundary and remained at the same inlet velocity (i.e. 0.13 m/s). The flow path in the left atrial model, on the other hand, was more influenced by structure-fluid relations. Streamline plots indicated that flow across the ablation site was approximately parallel to the tissue surface [Figure 36].

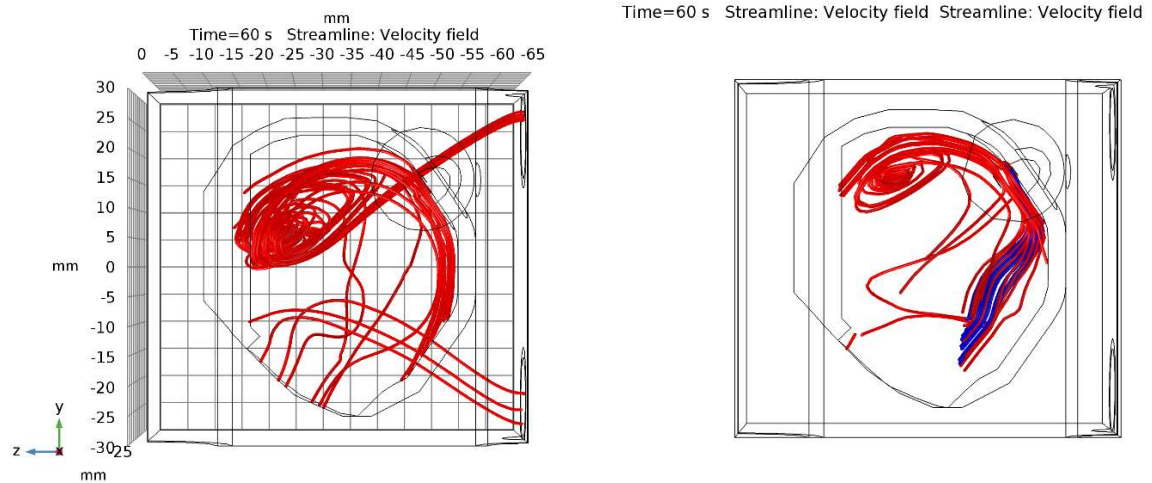


Figure 36. Streamlines of Blood Flow for Non-Irrigated (Left) and Saline-Irrigated (Right) Simulations in the Left Atrial Model.

Blood flow streamlines in red, saline flow streamlines in blue.

In the left atrial model, initial blood velocity was specified by a normal inflow condition at the PV inlets, commensurate with the pulmonary venous velocities measured by Doppler echocardiography in vivo. At the mitral valve outlet boundary, a 0 Pa gage pressure was applied, and flow between these points was solved for with a steady state laminar flow formulation. A plot of the flow velocity distribution is depicted in the following image [Figure 37].

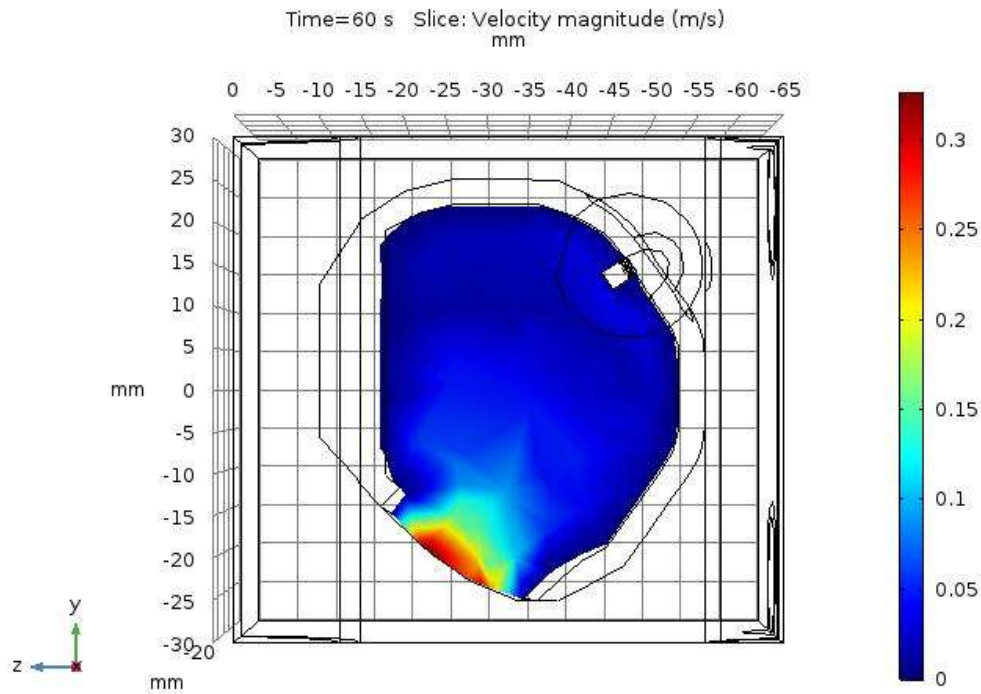


Figure 37. Blood Velocity Magnitude in the Left Atrial Model, Pulmonary Vein Inflow Velocity of 0.15 m/s. Transmitral velocity ~0.3 m/s, overall left atrial velocity between 0.05 and 0.10 m/s.

The resulting blood velocity distribution in the left atrial model varied with location, as was expected. Velocity distribution in the left atrial model remained low (<0.1 m/s) in the upper atrium, but quickly climbed to 0.15 m/s in the vestibular region, reaching 0.35 m/s at the center of the mitral valve annulus.

Table 9. Comparison of Blood Velocities in Doppler Echocardiography Study of AF Patients [89] vs the Left Atrial Model.

Location	Literature [m/s]	Model [m/s]
Domain Average	0.13 +/- 0.02	0.042
Transmitral (Luminal)	0.30 +/- 0.10	0.141
Ablation Site	N/A	0.017

When compared against flow studies created by MRI segmentation and CFD simulation, velocities of flow were similar or small in magnitude than in patients in AF, as depicted in [Figure 38].

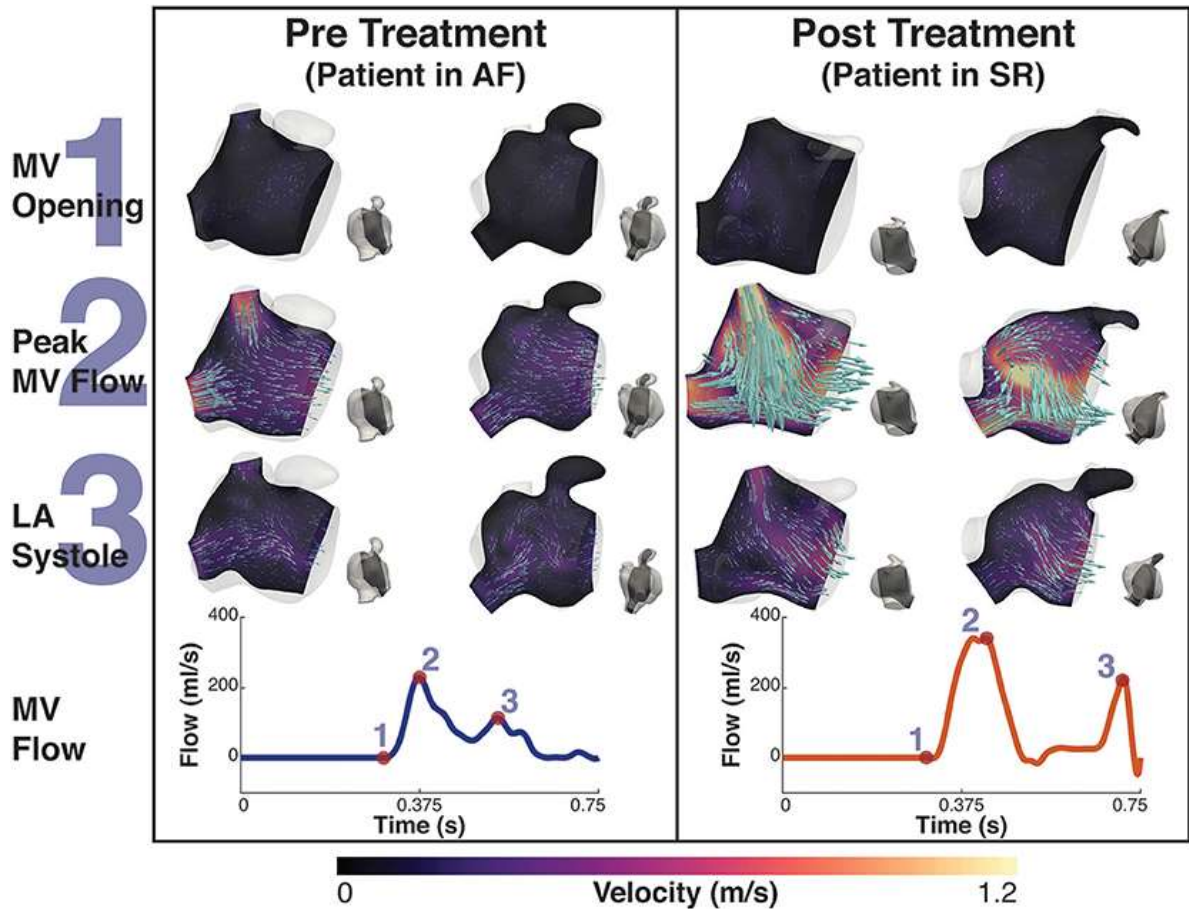


Figure 38. Flow Through the Left Atrium for Patients in AF and Sinus Rhythm.

Image credit: Dillon-Murphy et al 2018 [110]. Published under Creative Commons Attribution Licences 4.0 (<https://creativecommons.org/licenses/by/4.0>).

Nevertheless, the flow patterns of simple LA geometry differed greatly from the segmented model. Significant vortices in the atrial vestibule in the Dillon-Murphy et al study were only observed during peak flow in sinus rhythm. Critically though, flow near the ablation site was approximately parallel with the walls but with much lower velocity (~ 0.017 m/s) than in the simple preliminary models where flow was defined directly and had negligible fluid-structure interaction.

5.5 Electric Field in the Full Atrial Model

Interestingly, the electrical distribution in the full left atrial model favored higher current densities in the blood rather than the tissue, despite the ground ($V = 0$ V) boundary condition being in closer proximity to the tissue [Figure 39].

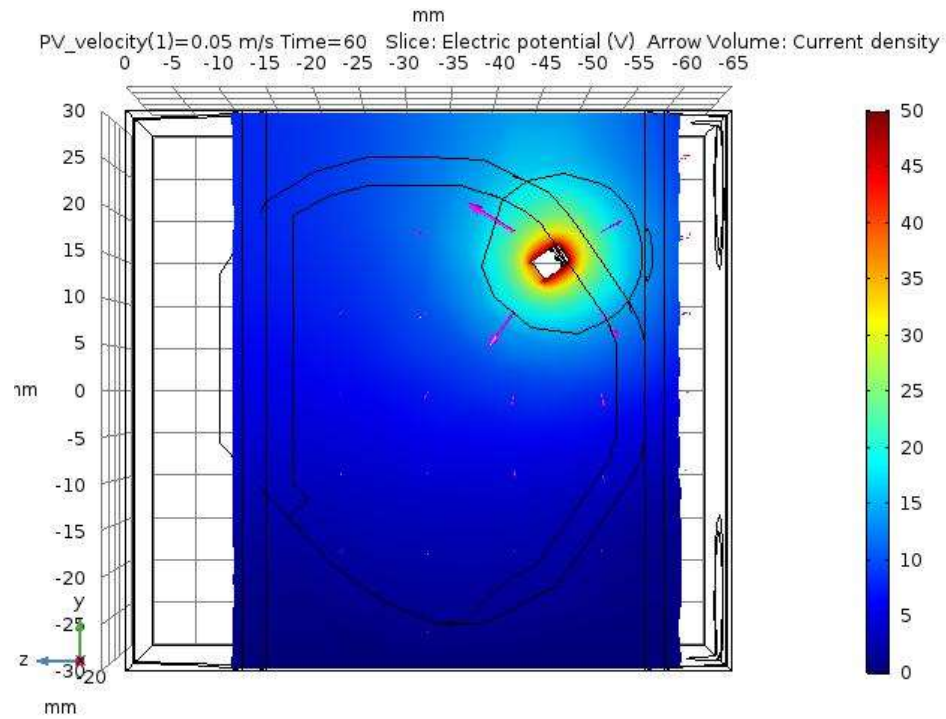


Figure 39. Electric Field with Overlaid Current Density Vector Field.

The magnitude of the current density vector was 2x that of the directed toward the tissue. Considering that all other boundaries were treated as electrically insulative, these results were peculiar and may warrant further investigation into material properties or boundary conditions.

5.6 Contact Area Investigation: Removal of Tissue Tenting

To investigate the impact of the reduced contact area due to the tissue tenting depression, the conical indent was removed and the simulation run with complete tip contact, as depicted in [Figure 40]. The results suggested that increased contact area did not result in deeper lesions.

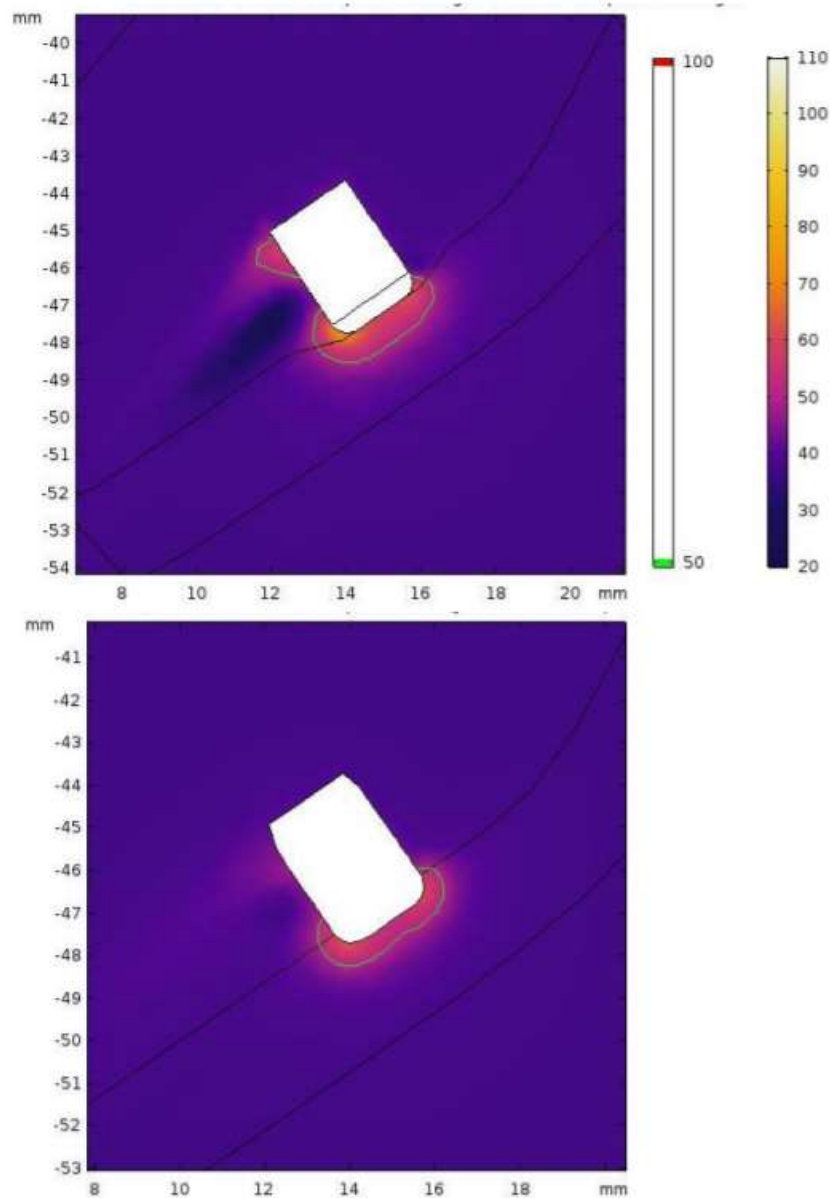


Figure 40. Temperature Distributions in Full Atrial Model Following a 50 V, 60 Second Ablation with Tissue Tenting (Top) and Complete Insertion Contact (Bottom).

DISCUSSION

A three-dimensional multi-physics model of the left atrium was developed to provide a more anatomically relevant testing environment for *in silico* evaluation of ablation catheter electrode tip designs. To achieve this, an anatomical assembly was developed in computer aided drafting software and transferred to COMSOL Multiphysics®. The physical model was generated using the electrical, thermal, and mass transport physics interfaces. Through these interfaces, the coupled Joule heating, Pennes' bioheat transfer, and incompressible Navier-Stokes flow equations were solved using finite element methods. Ablation lesions for a gold-standard RF ablation device (Biosense Webster Navistar Thermocool®) were generated during 60s, 50 V constant voltage ablations and compared with *in vivo* lesion characterization studies performed with this device.

6.1 Assessment of Multiphysics and Catheter Design Aspects in 2D and 3D Models

Physics and material properties were assessed in a simplified 3D ablation case, as is commonly reported in literature. Mean lesion dimensions in this model were between 5.9 – 26.9% different from the reported values of the Moreno et al 2014 *in vivo* lesion study. When compared with the range of reported values though, most of the measurements fell within the range indicated by the means \pm standard errors. With reasonably similar result, other procedural and design aspects were evaluated. These included the effect of blood flow, tip saline irrigation, and temperature-dependent properties on lesion production and morphology. The cooling effect of blood flow was substantial and necessary to achieve the classic ellipsoid lesion morphology. Saline irrigation reduced interface temperature and damage, although there was no discernible change in lesion dimensions. Finally, temperature-dependent properties formed smaller lesions—as expected—due to thermally mediated reduction of electrical conductivity.

6.2 The Left Atrial Anatomical Model

Desirability of the left atrial CAD model was a balance of anatomical fidelity versus computational efficiency. Aspects such as model symmetry and importability into COMSOL Multiphysics with minimal errors made for easier mesh generation and physics modeling. One of the main advantages of the developed model was the relative ease of customizability. New tissue domains

and catheter tip designs could be easily edited, added, positioned, and rebuilt within the assembly. Furthermore, exporting domains as an aggregated assembly cut down on lengthy repositioning and modification times in COMSOL's native CAD environment.

While modeling the geometry rather than producing it through image segmentation made for easier construction and catheter tip positioning, many anatomical aspects were simplified extensively or not included. As detailed in Chapter 2, the left atrial myocardial wall thickness is regionally variable, with wall thicknesses ranging from 1-5+ mm. An average thickness of 3 mm was chosen for ease of construction; however, the variable wall thicknesses have clinical significance with regards to procedural success and/or adverse events. Thinner areas like the posterior wall and the wall adjacent to the ascending aorta are at risk for excessive collateral damage or cardiac perforation. Thicker regions such as the ridges between ipsilateral pulmonary veins or at surrounding the opening of the atrial appendage may hinder procedural success by requiring increased RF applications and a more aggressive heating strategy to generate the ideal depth of lesion needed to prevent AF reconnection [84]. As such, the current testbed can assess catheter performance but has less predictive capability with assessing procedural success.

6.3 Ablation Simulation Performance vs Experimental Studies

While the lesion dimensions predicted by the 2D and simplified 3D preliminary models were close to those reported by Moreno et al [109], lesions generated with the perpendicular electrode orientation in the full atrial model were 91.3% narrower and 70% shallower than the experimental lesions. The source of this discrepancy is unclear, especially given the same physics, boundary conditions and parameters were used for the simplified 3D models. Moreover, ablation with the tangentially oriented electrode tip generated lesions that were closer to the experimental study and lesions generated in the simplified 3D model, with only -28.5 and +7.9% differences from reported max depth and diameter, respectively. Preliminary investigation on the root-cause of this discrepancy was carried out in the following studies on the impact of blood velocity on tissue/tip cooling, the distribution of current density, and the effect of contact area.

6.4 Associated Diagnostic Studies

6.4.1 Fluid Velocities and Blood Cooling

For this test bed, blood motion was included in order to assess thrombogenic potential of a catheter design. As expected, in simplifying the anatomical geometry, fluid-structure interaction significantly deviated from realistic flows. While realistic flow patterns and velocities were beyond the scope of this thesis, initial evaluations suggested that they had a large impact on the lesion outcomes [Appendix H]. This is supported by the governing expressions that define heat transfer convective coefficients at the electrode-blood interface (h_E) and the blood tissue interface (h_T), as described by Gonzalez-Suarez et al 2016 and others [45]. As velocity field magnitude increases, the degree of cooling by the blood also increases. The proportionality relationships of heat transfer coefficient to velocity field can be summarized by the following:

$$h_E \propto u^{0.466}$$

$$h_T \propto u^{0.8}$$

However, these assume Newtonian heat transfer conditions assume a uniform, tangential flow across the surface of the tissue, which is not the case in the real atrial model context. Higher resolution imaging studies [111] and segmented image computational flow models depict [110] vortices and areas of high flow throughout the atrial activation cycle. More heat loss to blood means lower net tissue heating, thus leading to reduced lesion sizes. Flow boundary conditions in this model were set using an average value for PV inflow velocity from literature. It is not clear whether that velocity represented the average velocity, or the luminal velocity found away from the walls. Most importantly though, the velocities developed within this left atrial model were for the most part lower than typical atrial flow velocities for both healthy and AF hearts. Thus, it is unlikely that excess blood cooling due to flow is occurring.

6.4.2 Contact Area Investigation

Contrary to what was expected, tangential lesions produced larger and deeper lesions than perpendicular lesions. This does not match experimental studies of electrode orientation, which suggested that electrode tips oriented parallel with the tissue surface led to smaller lesions overall [87]. The cause of this discrepancy is likely the way electrode contact was modeled. In the

perpendicular orientation case, a dish-like indent with a depth of 0.5 mm was formed at the catheter contact site as a rough approximation of tissue tenting induced by contact force. Under the assumption that less contact force was achievable with the tangential orientation, no such indent was applied, with the catheter tip inset minimally (<0.25 mm) into the tissue volume.

The effect of contact area was primarily investigated by running an ablation in which the conical depression used to simulate tissue tenting was removed. Interestingly, the lesion dimension change by omitting the depression and allowing continuous contact with the inserted portion of the catheter was miniscule. This suggests that reduced contact area was not responsible for the perpendicular/tangential and simple/full 3D model discrepancies. Given that current is a function of current density and area, all else held equal, charge traveling between a smaller electrode and a larger electrode should result in a higher local current density at the smaller electrode. Thus more investigation is still necessary to pinpoint the cause of these anomalous results.

6.5 Limitations

While assumption for homogenous isotropic and parametrically independent material domains is generally acceptable for “large” geometries, the inherent anisotropy of tissues coupled with multi-parameter dependent material properties means that this assumption may oversimplify the real situation. Furthermore, the source of the parameter values also casts uncertainty on their appropriateness. Most of the material properties and parameters used in this study were based on ex vivo (i.e. non-living and non-perfused) and/or non-human tissues.

Core assumptions of the Pennes’ bioheat equation may also contribute to discrepancies between experimental and modeled results. This equation assumes that the solution domain is an infinite continuous material. With this assumption of macro-continuity, the propagation speed of heat is assumed to be instant. However, in cases of high temperatures, high heat fluxes, and short durations, the lagging of the heat wave is more apparent. Because of this, there are several alternate bioheat models—like the hyperbolic heat transfer model—which take this phenomenon into account. In comparative studies of hyperbolic bioheat vs the Pennes’ bioheat equations, lesion size plotted against time indicate that the bioheat equation estimates a larger lesion size at $t < 30$ seconds. After 30 seconds, lesion volume from hyperbolic heat equation overtakes the Pennes’ bioheat lesion

estimation, with an estimated 20% difference in lesion size at 60 seconds [112]. Therefore, the formulation of the bioheat transfer equation—while likely not a huge contributor—could be underestimating lesion sizes. Lastly, better computational resources would enable faster solution times, finer meshes, and more complex physical situations.

6.6 Next Steps

The most likely remaining culprit has to do with the current density. Dispersive electrodes placed on the posterior of the patient are sized such that there is a larger surface area discrepancy between the active and dispersive (ground) electrodes. As mentioned in Chapter 3, larger relative dispersive electrodes lead to an increase in the current density adjacent to the active electrode. It is possible that the boundary representing the posterior face of the tissue block containing the left atrium was not large enough. This might be remedied by increasing the side-length of the generic tissue block's posterior face.

Furthermore, early studies on tissue block sizing performed with the simpler model geometries emphasized the impact of separation distance between the active and dispersive electrodes. This is somewhat supported by experimental studies on skin electrode placement done for endocardial ablations in sheep, where skin electrodes placed directly opposite of the catheter electrode tip produce deeper and more consistent lesion depths [113].

The tissue is essentially a volumetric resistive domain. With a larger intermediary volume between the active and dispersive electrodes, there would be a correspondingly larger impedance between them. Following Ohmic relations ($V=IR$), that would imply that current in the higher impedance cases would be lower. While both of these current related suggestions are plausible, they do not explain why the tangential electrode positioning performed so well compared with the perpendicular electrode position. Thus, more studies are necessary.

There are several potential improvements for this model that could be implemented. Most critically is investigating the causes behind the dramatic decrease in lesion size with the perpendicular electrode lesion for the full atrial anatomic model. Another improvement would be implementation of a power terminal condition, or voltage titration algorithm to achieve the desired power output. While lesion profiles had the correct morphology—i.e. ellipsoids—the observed insufficiency of the 50 V

potential assigned to the electrode tip suggests that greater environmental feedback and power titration may be necessary. This could be achieved using power- or temperature-controlled ablation algorithms. As these algorithms are a critical component of device performance in clinic, emulation of these control systems might be the key to producing more realistic lesion dimensions. Once power output could be appropriately controlled, parametric properties could be added to the material models.

Geometry-wise, regional wall thicknesses could be altered to emulate their real-life counterparts. Currently the wall thickness is set to a uniform 3 mm, but anatomical studies of the left atrium indicate that the wall thickness can vary from 1 – 5 mm. Depending on the application of this test bed environment, other structure dimensions might need to be customized as well. For example, the 4 pulmonary veins in the current model have a circular cross section, with an outer diameter of 15 mm and an inner diameter of 13 mm. This does not reflect the true diameters of the pulmonary veins, where the superior PVs tend to be larger in diameter than the inferior PVs, and the right PVs tend to be smaller than the left PVs. Realistic PV orifice dimensions would be of interest when testing balloon-based catheter ablation systems.

While this model was built and tested specifically with the Biosense Webster Thermocool® catheter, testing another commercially available catheter tip design and comparing it with the output of the model would strengthen the model validity. The ultimate purpose of this model is to aid academic research and design of catheter tips through a low-cost, low-variability test bed. Therefore, the continuation of this project would be the testing and optimization performance of a novel catheter tip design.

Finally, the use of this model is not limited to radiofrequency ablation; the bioheat module accounts for damage due to tissue heating *and* freezing. Thus, with some modification of the material model to include lower temperature ranges, cryoballoon designs could be tested.

6.7 Conclusions

A 3-dimensional, anatomically relevant, left atrial (LA) test bed for ablation catheter tip evaluation was constructed in COMSOL Multiphysics®. The test bed was evaluated using a catheter tip based on the Biosense Webster Thermocool® irrigated RF ablation catheter, for a 60 second constant 50 V ablation. The morphology of the lesions produced in the atrial testbed had the typical ellipsoid shape with surface diameter consistent with the electrode contact area observed in lesion studies.

While the tangentially oriented tip electrodes generated lesions similar to the literature comparison study (28.4 and 7.9% difference for max depth and diameter) and the simplified 3D ablation case, the perpendicularly oriented electrodes generated 70 – 90% smaller lesions. Possible sources of discrepancy include reduced current flow due to larger resistive tissue volumes, the use of non-parametric material properties, and neglecting the time-dependence of thermal wave propagation. Once discrepancies are accounted for, this testbed could be customized to assess performance of other hyper- or hypothermic atrial ablation devices.

REFERENCES

1. S. Colilla, A. Crow, W. Petkun, D. E. Singer, T. Simon and X. Liu, "Estimates of current and future incidence and prevalence of atrial fibrillation in the U.S. adult population," *American Journal of Cardiology*, vol. 112, no. 8, pp. 1142-1147, 2013.
2. S. S. Chugh, G. A. Roth, R. F. Gillum and G. A. Mensah, "Global burden of atrial fibrillation in developed and developing nations," *Global Heart*, vol. 9, no. 1, pp. 113- 119, 2014.
3. Y.-k. Iwasaki, K. Nishida, T. Kato and S. Nattel, "Atrial Fibrillation Pathophysiology: Implications for Management," *Circulation*, vol. 124, pp. 2264-2274, 2011.
4. E. E. Cogen, T. Tombul, G. Yildirim, F. O. Odabas and R. Sayin, "The role of atrial fibrillation on mortality and morbidity in patients with ischaemic stroke," *The Journal of the Pakistan Medical Association*, pp. 1516-1519, 2013.
5. D. D. McManus, M. Rienstra and E. J. Benjamin, "An Update on the Prognosis of Patients with Atrial Fibrillation," *Circulation*, vol. 126, no. 10, pp. e143-e146, 2012.
6. S. Aldrugh, M. Sardana, N. Henninger, J. S. Saczynski and D. D. McManus, "Atrial fibrillation, cognition and dementia: A review," *Journal of Cardiovascular Electrophysiology*, vol. 28, no. 8, pp. 958-965, 8 2017.
7. J. Andrade, P. Khairy, D. Dobrev and S. Nattel, "The Clinical Profile and Pathophysiology of Atrial Fibrillation," *Circulation Research*, vol. 114, no. 9, pp. 1453- 1468, 25 4 2014.
8. M. Thind, D. N. Holmes, M. Badri, K. S. Pieper, A. Singh, R. G. Blanco, B. A. Steinberg, G. C. Fonarow, B. J. Gersh, K. W. Mahaffey, E. D. Peterson, J. A. Reiffel, J. P. Piccini and P. R. Kowey, "Emboic and Other Adverse Outcomes in Symptomatic Versus Asymptomatic Patients With Atrial Fibrillation (from the ORBIT-AF Registry)," *The American Journal of Cardiology*, pp. 1677-1683, 2018.
9. T. Kazui, M. C. Henn, Y. Watanabe, S. J. Kovács, C. P. Lawrance, J. W. Greenberg, M. Moon, R. B. Schuessler and R. J. Damiano, "The impact of 6 weeks of atrial fibrillation on left atrial and ventricular structure and function," *The Journal of Thoracic and Cardiovascular Surgery*, vol. 150, no. 6, pp. 1602-1608.e1, 1 12 2015.
10. A. Pedersen, "Will Apama Help Bos Sci Find Its Rhythm?," 2017. [Online]. Available:

<https://www.mddionline.com/will-apama-help-bos-sci-find-its-rhythm>

11. A. Pedersen, "3 Medtech Markets That Are Showing Growth," 2018. [Online]. Available: <https://www.mddionline.com/3-medtech-markets-are-showing-growth>.
12. J. M. Guerra, E. Jorge, S. Raga, C. G. Alvez-mont, C. Galvez-Monton, C. Alonso-Martin, E. Rodriguez-Font, J. Cinca and X. Vinolas, "Effects of Open-Irrigated Radiofrequency Ablation Catheter Design on Lesion Formation and Complications : In Vitro Comparison of 6 Different Devices," *Journal of Cardiovascular Electrophysiology*, vol. 24, no. 10, pp. 1157-1162, 1 5 2013.
13. D. Schutt, E. J. Berjano and D. Haemmerich, "Effect of electrode thermal conductivity in cardiac radiofrequency catheter ablation: A computational modeling study," *International Journal of Hyperthermia*, pp. 99-107, 2009.
14. N. Gallagher, E. C. Fear, I. A. Byrd and E. J. Vigmond, "Contact Geometry Affects Lesion Formation in Radio-Frequency Cardiac Catheter Ablation," *PLoS ONE*, vol. 8, no. 9, p. e73242, 23 9 2013.
15. D. Haemmerich, "Mathematical Modeling of Impedance Controlled Radiofrequency Tumor Ablation and Ex-Vivo Validation," in *32nd Annual International Conference of the IEEE EMBS*, Buenos Aires, Argentina, 2010.

16. D. Haemmerich and J. G. Webster, "Automatic control of finite element models for temperature-controlled radiofrequency ablation," *BioMedical Engineering OnLine*, vol. 4, no. 1, p. 42, 2005.
17. S. Yan, X. Wu and W. Wang, "Theoretical and experimental analysis of amplitude control ablation and bipolar ablation in creating linear lesion and discrete lesions for treating atrial fibrillation," *International Journal of Hyperthermia*, vol. 33, no. 6, pp. 608-616, 18 8 2017.
18. J. B. Leonard, K. R. Foster and T. W. Athey, "Thermal Properties of Tissue Equivalent Phantom Materials," *IEEE Transactions on Biomedical Engineering*, vol. 31, no. 7, pp. 33-36, 1984.
19. R. Blasco-Gimenez, J. L. Lequerica, M. Herrero, F. Hornero and E. J. Berjano, "Blackbox modeling to estimate tissue temperature during radiofrequency catheter cardiac ablation: Feasibility study on an agar phantom model," *Physiological Measurement*, vol. 31, no. 4, pp. 581-594, 1 4 2010.
20. Y.-C. N. Cheng, R. W. Brown, Y.-C. Chung, J. L. Duerk, H. Fujita, J. S. Lewin, D. E. Schuele and S. Shvartsman, "Calculated RF electric field and temperature distributions in RF thermal ablation: Comparison with gel experiments and liver imaging," *Journal of Magnetic Resonance Imaging*, vol. 8, no. 1, pp. 70-76, 1 1 1998.
21. Z. Bu-Lin, H. Bing, K. Sheng-Li, Y. Huang, W. Rong and L. Jia, "A polyacrylamide gel phantom for radiofrequency ablation," *International Journal of Hyperthermia*, vol. 24, no. 7, pp. 568-576, 9 1 2008.
22. A. S. Mikhail, A. H. Negussie, C. Graham, M. Mathew, B. J. Wood and A. Partanen, "Evaluation of a tissue-mimicking thermochromic phantom for radiofrequency ablation.," *Medical Physics*, vol. 43, no. 7, p. 4304, 7 2016.
23. "Reporting of Computational Modeling Studies in Medical Device Submissions Guidance for Industry and Food and Drug Administration Staff," 2016.
24. S. Tungjitsukulmun, I. E. J. Woo, H. Cao, J.-Z. Tsai, V. R. Vorperian and J. G. Webster, "Thermal-electrical finite element modelling for radio frequency cardiac ablation: Effects of changes in myocardial properties," *Med. Biol. Eng. Comput*, vol. 38, pp. 562-568, 2000.

25. D. E. Haines and D. D. WATSON, "Tissue Heating During Radiofrequency Catheter Ablation: A Thermodynamic Model and Observations in Isolated Perfused and Superfused Canine Right Ventricular Free Wall," *Pacing and Clinical Electrophysiology*, vol. 12, no. 6, pp. 962-976, 1 6 1989.
26. M. J. Rivera, J. A. Lopez-Molina, M. Trujillo, V. Romero-Garcia and E. J. Berjano, "Analytical Validation of COMSOL Multiphysics for Theoretical Models of Radiofrequency Ablation Including the Hyperbolic Bioheat Transfer Equation," in *32nd Annual International Conference of the IEEE EMBS*, Buenos Aires, Argentina, 2010.
27. S. Labonte, "Numerical Model for Radio-Frequency Ablation of the Endocardium and its Experimental Validation," *IEEE Transactions on Biomedical Engineering*, vol. 41, no. 2, pp. 108-115, 1994.
28. Z. Kaouk, "A finite element model of a microwave catheter for cardiac ablation," *IEEE Transactions on Microwave Theory and Techniques*, vol. 44, no. 10 PART 2, pp. 1848- 1854, 1996.
29. D. Panescu, J. Whayne, S. Fleischman, M. Mirotznik, D. Swanson and J. Webster, "Three-dimensional finite element analysis of current density and temperature distributions during radio-frequency ablation," *IEEE Transactions on Biomedical Engineering*, vol. 42, no. 9, pp. 879-890, 1995.
30. J. A. Pearce and S. Thomsen, "Numerical Models of RF Ablation in Myocardium," in *IEEE-EMBC and CMBEC*, 1995.
31. C. L. Antunes, T. R. O. Almeida, N. Raposeiro, B. Gonçalves and P. Almeida, "Using a tubular electrode for radiofrequency ablation: Numerical and experimental analysis," *COMPEL - The International Journal for Computation and Mathematics in Electrical and Electronic Engineering*, vol. 31, no. 4, pp. 1077-1086, 2012.
32. M. Jain and P. Wolf, "A finite element study of the effects of ground electrode position on radio frequency ablation lesions," in *Proceedings of 18th Annual International Conference of the IEEE Engineering in Medicine and Biology Society*.
33. M. Jain and P. Wolf, "Effect of electrode contact on lesion growth during temperature

- controlled radio frequency ablation," in Proceedings of the 20th Annual International Conference of the IEEE Engineering in Medicine and Biology Society. Vol.20 Biomedical Engineering Towards the Year 2000 and Beyond (Cat. No.98CH36286).
34. M. Jain and P. Wolf, "Finite element analysis predicts dose-response relationship for constant power and temperature controlled radiofrequency ablation," in Proceedings of the 19th Annual International Conference of the IEEE Engineering in Medicine and Biology Society. 'Magnificent Milestones and Emerging Opportunities in Medical Engineering' (Cat. No.97CH36136).
 35. M. K. Jain and P. D. Wolf, "A Three-Dimensional Finite Element Model of Radiofrequency Ablation with Blood Flow and its Experimental Validation," Annals of Biomedical Engineering, pp. 1075-1084, 2000.
 36. M. K. Jain and P. D. Wolf, "Temperature-Controlled and Constant-Power What Affects Lesion Growth ?," Convergence, vol. 46, no. 12, pp. 1405-1412, 1999.

37. H. Cao and S. Paul, "Finite Element Model of Wet Brush RF Ablation Catheter," in 30th Annual International IEEE EMBS Conference, 2008.
38. T. A. Pilcher, A. L. Sanford, J. P. Saul and D. Haemmerich, "Convective Cooling Effect on Cooled-Tip Catheter Compared to Large-Tip Catheter Radiofrequency Ablation," *Pacing and Clinical Electrophysiology*, vol. 29, no. 12, pp. 1368-1374, 12 2006.
39. X. Min and R. Mehra, "Analysis of the Variables that Affect Electrode and Tissue Temperature during RF Ablation in a Finite Element Analysis Model," in IEEE, 2003.
40. H. Cao, V. R. Vorperian, S. Tungjitumolmun, J.-Z. Tsai, D. Haemmerich, Y. B. Choy and J. G. Webster, "Flow Effect on Lesion Formation in RF Cardiac Catheter Ablation," *IEEE Transactions on Biomedical Engineering*, pp. 425-432, 2001.
41. OM. LAU, B. HU, R. WERNETH, M. Sherman, H. ORAL, F. Morady and P. KRYSL, "A Theoretical and Experimental Analysis of Radiofrequency Ablation with a Multielectrode, Phased, Duty-Cycled System," *Pacing and Clinical Electrophysiology*, vol. 33, no. 9, pp. 1089-1100, 9 2010.
42. Y.-C. Lai, Y. B. Choy, D. Haemmerich, V. R. Vorperian and J. G. Webster, "Lesion Size Estimator of Cardiac Radiofrequency Ablation at Different Common Locations With Different Tip Temperatures," *IEEE Transactions on Biomedical Engineering*, vol. 51, no. 10, pp. 1859-1864, 2004.
43. I. dos Santos, D. Haemmerich, C. Pinheiro, A. da Rocha, C. da Silva Pinheiro, A. Ferreira da Rocha, C. Pinheiro and A. da Rocha, "Effect of variable heat transfer coefficient on tissue temperature next to a large vessel during radiofrequency tumor ablation," *BioMedical Engineering OnLine*, vol. 7, no. 1, pp. 1-11, 2008.
44. X. Chen and G. M. Saidel, "Mathematical Modeling of Thermal Ablation in Tissue Surrounding a Large Vessel," *Journal of Biomechanical Engineering*, vol. 131, no. 1, p. 011001, 11 2008.
45. A. Gonzalez-Suarez, E. Berjano, J. M. Guerra and L. Gerardo-Giorda, "Computational Modeling of Open-Irrigated Electrodes for Radiofrequency Cardiac Ablation Including Blood Motion-Saline Flow Interaction," *PLOS ONE*, 2016.

46. A. Gonzalez-Suarez, E. Berjano, J. M. Guerra and L. Gerardo-Giorda, "A Computational Model of Open-Irrigated Electrode for Endocardial RF Catheter Ablation," *Computing in Cardiology*, pp. 73-76, 2015.
47. A. González-Suárez, J. J. Pérez and E. J. Berjano, "Should fluid dynamics be included in computer models of RF cardiac ablation by irrigated-tip electrodes?," *BioMedical Engineering Online*, vol. 17, no. 1, pp. 1-14, 2018.
48. S. Tungjitkusolmun, V. R. Vorperian, N. C. Bhavaraju, H. Cao, J.-Z. Tsai and J. G. J. Webster, "Guidelines for predicting lesion size at common endocardial locations during radio-frequency ablation," *IEEE Transactions on Biomedical Engineering*, vol. 48, no. 2, pp. 194-201, 2001.
49. J. Arenas, J. J. Pérez, M. Trujillo and E. J. Berjano, "Computer modeling and ex vivo experiments with a (saline-linked) irrigated electrode for RF-assisted heating," *BioMedical Engineering Online*, vol. 13, no. 164, pp. 1-16, 2014.
50. J. J. Pérez, A. González-Suárez and E. J. Berjano, "Numerical analysis of thermal impact of intramyocardial capillary blood flow during radiofrequency cardiac ablation," *International Journal of Hyperthermia*, vol. 34, no. 3, pp. 243-249, 3 4 2018.
51. A. González-Suárez and E. J. Berjano, "Comparative analysis of different methods of modeling the thermal effect of circulating blood flow during RF cardiac ablation," *IEEE Transactions on Biomedical Engineering*, vol. 63, no. 2, pp. 250-259, 2 2016.
52. J. Gopalakrishnan, "A mathematical model for irrigated epicardial radiofrequency ablation," *Annals of Biomedical Engineering*, 2002.
53. J. Alba, M. Trujillo, R. Blasco and E. J. Berjano, "Computer Modeling to Study the Dynamic Response of the Temperature Control Loop in RF Cardiac Ablation," in *MEDICON 2010, IFMBE Proceedings 29*, 2010.
54. M. Trujillo, J. Bon, M. José Rivera, F. Burdío and E. J. Berjano, "Computer modelling of an impedance-controlled pulsing protocol for RF tumour ablation with a cooled electrode," *International Journal of Hyperthermia*, vol. 32, no. 8, pp. 931-939, 16 11 2016.
55. S. Tungjitkusolmun, E. J. Woo, H. Cao, J. Z. Tsai, V. R. Vorperian and J. G. Webster, "Thermal-

- electrical finite element modelling for radio frequency cardiac ablation: effects of changes in myocardial properties," *Med. Biol. Eng. Comput.*, pp. 562-568, 2000.
56. H. Watanabe, N. Yamazaki, Y. Kobayashi, T. Miyashita, M. Hashizume and M. G. Fujie, "Temperature Dependence of Thermal Conductivity of Liver Based on Various Experiments and a Numerical Simulation for RF Ablation," in *2010 Annual International Conference of the IEEE Engineering in Medicine and Biology*, 2010.
 57. J. P. Abraham and E. M. Sparrow, "A thermal-ablation bioheat model including liquid-to-vapor phase change, pressure- and necrosis-dependent perfusion, and moisture-dependent properties," *International Journal of Heat and Mass Transfer*, vol. 50, no. 13-14, pp. 2537-2544, 2007.
 58. E. J. Berjano, *Theoretical modeling for radiofrequency ablation: State-of-the-art and challenges for the future*, 2006.
 59. E. J. Berjano and F. Hornero, "What affects esophageal injury during radiofrequency ablation of the left atrium? An engineering study based on finite-element analysis," *Physiological Measurement*, vol. 26, no. 5, pp. 837-848, 2005.

60. F. HORNERO and E. J. BERJANO, "Esophageal Temperature During Radiofrequency Catheter Ablation of Left Atrium: A Three-Dimensional Computer Modeling Study," *Journal of Cardiovascular Electrophysiology*, vol. 17, no. 4, pp. 405-410, 1 4 2006.
61. C. Audigier, T. Mansi, H. Delingette, S. Rapaka, T. Passerini, V. Mihalef, M.-P. Jolly, . R. Pop, M. Diana, . Luc Soler, A. Kamen, . Dorin Comaniciu and . N. Ayache, "Comprehensive preclinical evaluation of a multi-physics model of liver tumor radiofrequency ablation," *Int J CARS*, vol. 12, pp. 1543-1559, 2017.
62. O. Dössel, M. W. Krueger, F. M. Weber, M. Wilhelms and G. Seemann, "Computational modeling of the human atrial anatomy and electrophysiology," *Medical and Biological Engineering and Computing*, vol. 50, pp. 773-799, 2012.
63. E. J. Vigmond, R. Ruckdeschel and N. Trayanova, "Reentry in a Morphologically Realistic Atrial Model," *Journal of Cardiovascular Electrophysiology*, vol. 12, no. 9, 2003.
64. C. Bellini, E. S. Di Martino and S. Federico, "Mechanical Behaviour of the Human Atria," *Annals of Biomedical Engineering*, vol. 41, no. 7, pp. 1478-1490, 11 7 2013
65. L. Zhao, X. X. Meng, J. Y. Zhang, Q. J. Jiang, X. Zhao, S. Y. Liu and D. N. Liao, "Anatomical morphologic study of pulmonary vein antrum by computed tomography angiography in patients with atrial fibrillation," *Journal of Interventional Radiology*, vol. 17, no. 12, pp. 879-883, 12 2008.
66. S. Y. Ho, J. A. Cabrera and D. Sanchez-Quintana, "Left Atrial Anatomy Revisited," *Circulation: Advances in Arrhythmia and Electrophysiology*, vol. 5, no. 1, pp. 220-228, 2 2012.

67. S. Y. Ho, C. Basso, J. A. Cabrera, A. Corrado, J. Farré, J. Kautzner and R. De Ponti, "Anatomy of Structures Relevant to Atrial Fibrillation Ablation," in *Atrial Fibrillation Ablation, 2011 Update: The State of the Art Based on the VeniceChart International Consensus Document*, A. Natale and A. Raviele, Eds., John Wiley & Sons, Ltd, 2011, pp. 1-19
68. J. A. Cabrera, S. Y. Ho, V. Climent and D. Sánchez-Quintana, "The architecture of the left lateral atrial wall: A particular anatomic region with implications for ablation of atrial fibrillation," *European Heart Journal*, vol. 29, pp. 356-362, 2008.
69. J. Jalife, M. Allesie, C. Antzelevitch, Y. Iesaka, W. M. Jackman, M. M. Scheinman and S.-A. Chen, "Pathophysiology of atrial fibrillation," in *Atrial Fibrillation Ablation: The State of the Art Based on the Venicechart International Consensus Document*, A. Natale and A. Raviele, Eds., John Wiley & Sons, Ltd, 2011, pp. 20-34.
70. C. Antzelevitch and A. Burashnikov, "Overview of Basic Mechanisms of Cardiac Arrhythmia," *Cardiac Electrophysiology Clinics*, vol. 3, no. 1, pp. 23-45, 1 3 2011.

71. H. Calkins, G. Hindricks, R. Cappato, Y.-H. Kim, E. B. Saad, L. Aguinaga, J. G. Akar, V. Badhwar, J. Brugada, A. J. Camm, P.-S. Chen, S.-A. Chen, M. K. Chung, J. C. Nielsen, A. B. Curtis, D. Wyn Davies, J. D. Day, A. D'Avila, N. de Groot, L. Di Biase, M. Duytschaever, J. R. Edgerton, K. A. Ellenbogen, P. T. Ellinor, S. Ernst, G. Fenelon, E. P. Gerstenfeld, D. E. Haines, M. Haissaguerre, R. H. Helm, E. Hylek, W. M. Jackman, J. Jalife, J. M. Kalman, J. Kautzner, H. Kottkamp, K.-H. Kuck, K. Kumagai, R. Lee, T. Lewalter, B. D. Lindsay, L. Macle, M. Mansour, F. E. Marchlinski, G. F. Michaud, H. Nakagawa, A. Natale, S. Nattel, K. Okumura, D. L. Packer, E. Pokushalov, M. R. Reynolds, P. Sanders, M. Scanavacca, R. J. Schilling, C. Tondo, H.-M. Tsao, A. Verma, D. J. Wilber and T. Yamane, "2017 HRS/EHRA/ECAS/APHRS/SOLAECE expert consensus statement on catheter and surgical ablation of atrial fibrillation: executive summary," *Journal of Interventional Cardiac Electrophysiology*, vol. 50, no. 1, pp. 1- 55, 15 10 2017.
72. F. Holmqvist, S. Kim, B. Steinberg, J. Reiffel, K. Mahaffey, B. Gersh, G. Fonarow, G. Naccarelli, P. Chang, J. Freeman, P. Kowey, L. Thomas, E. Peterson and J. Piccini, "Heart rate is associated with progression of atrial fibrillation, independent of rhythm," *Heart*, vol. 101, no. 11, pp. 894-899, 2015.
73. G. Batra, B. Svennblad, C. Held, T. Jernberg, P. Johanson, L. Wallentin and J. Oldgren, "All types of atrial fibrillation in the setting of myocardial infarction are associated with impaired outcome," *Heart*, vol. 102, no. 12, pp. 926-933, 2016.
74. "Rate vs rhythm control," in *Atrial Fibrillation: The Management of Atrial Fibrillation*, London, National Institute for Health and Care Excellence (UK), 2014.

75. N. J. Sethi, J. Feinberg, E. E. Nielsen, S. Safi, C. Gluud and J. C. Jakobsen, "The effects of rhythm control strategies versus rate control strategies for atrial fibrillation and atrial flutter: A systematic review with meta-analysis and Trial Sequential Analysis," *PLOS ONE*, vol. 12, no. 10, p. e0186856, 26 10 2017.
76. D. Caldeira, C. David and C. Sampaio, "Rate versus rhythm control in atrial fibrillation and clinical outcomes: Updated systematic review and meta-analysis of randomized controlled trials," *Archives of Cardiovascular Diseases*, vol. 105, no. 4, pp. 226-238, 4 2012.
77. A. Noheria, A. Kumar, J. V. J. Wylie and M. E. Josephson, "Catheter Ablation vs Antiarrhythmic Drug Therapy for Atrial Fibrillation," *Archives of Internal Medicine*, vol. 168, no. 6, pp. 581-586, 2008.
78. K.-H. Kuck, P. Adragao, D. J. Burkhard, P. Jais, D. Keane, H. Nakagawa, R. Schweikert, J. Sra and V. Y. Reddy, "Techniques and technologies for atrial fibrillation catheter ablation," in *Atrial Fibrillation Ablation: The State of the Art Based on the Venicechart International Consensus Document*, A. Natale and A. ROaviele, Eds., John Wiley & Sons, Ltd, 2011, pp. 35-60.
79. M. Bishop, R. Rajani, G. Plank, N. Gaddum, G. Carr-White, M. Wright, M. O'Neill and S. Niederer, "Three-dimensional atrial wall thickness maps to inform catheter ablation procedures for atrial fibrillation," *Europace*, pp. 376-383, 2016.
80. G. P. Aurigemma, J. S. Gottdiener, A. M. Arnold, M. Chinali, J. C. Hill and D. Kitzman, "Left atrial volume and geometry in healthy aging the cardiovascular health study," *Circulation: Cardiovascular Imaging*, vol. 2, pp. 282-289, 2009.
81. R. Ang, G. Domenichini, M. C. Finlay, R. J. Schilling and R. J. Hunter, "The Hot and the Cold: Radiofrequency Versus Cryoballoon Ablation for Atrial Fibrillation," *Current Cardiology Reports*, vol. 17, no. 9, p. 77, 13 9 2015.
82. D. Kim, "Heart Anatomy," *Institute for the Study of Knowledge Management in Education: OER Commons*, 2016.
83. V. Jacobs, H. T. May, B. G. Crandall, B. Ballantyne, B. Chisum, D. Johnson, K. G. Graves, M. Cutler, J. D. Day, C. Mallender, J. S. Osborn, J. P. Weiss and T. J. Bunch, "Vagus nerve injury

- symptoms after catheter ablation for atrial fibrillation," *Pacing and Clinical Electrophysiology*, vol. 41, no. 4, pp. 389-395, 4 2018.
84. G. Lee and J. M. Kalman, "Endpoints in Ablation of Paroxysmal Atrial Fibrillation: When is Enough Enough?," *Journal of Cardiovascular Electrophysiology*, pp. 389-392, 2010.
 85. P. Chavez, F. H. Messerli, A. C. Dominguez, E. F. Aziz, T. Sichrovsky, D. Garcia, C. D. Barrett and S. Danik, "Atrioesophageal fistula following ablation procedures for atrial fibrillation: systemic review of case reports," *Open Heart*, vol. 2, 2015.
 86. J. L. Eggleston and W. W. von Maltzahn, "Electrosurgical Devices," in *The Biomedical Engineering Handbook*, 2nd ed., J. D. Bronzino, Ed., Boca Raton, CRC Press LLC, 2000.
 87. M. Houmsse and E. G. Daoud, "Biophysics and clinical utility of irrigated tip radiofrequency catheter ablation," *Expert Reviews in Medical Devices*, vol. 9, no. 1, pp. 59-70, 2012.
 88. S. Dokos, *Modelling Organs, Tissues, Cells and Devices: Using MATLAB and COMSOL Multiphysics*, Springer-Verlag Berlin Heidelberg, 2017.
 89. D. C. Lee, M. Markl, J. Ng, M. Carr, B. Benefield, J. C. Carr and J. J. Goldberger, "Three dimensional left atrial blood flow characteristics in patients with atrial fibrillation assessed by 4D flow CMR," *European Heart Journal*, vol. 17, pp. 1259-1268, 2016.

90. T. Hanke, "Surgical management of the left atrial appendage: a must or a myth?," *European Journal of Cardio-Thoracic Surgery*, vol. 53, no. suppl_1, pp. i33-i38, 1 4 2018.
91. G. B. Forleo, C. Tondo, L. De Luca, A. D. Russo, M. Casella, V. De Sanctis, F. Clementi, R. Lopes Fagundes, R. Leo, F. Romeo and M. Mantica, "Gender-related differences in catheter ablation of atrial fibrillation," *Europace*, vol. 9, pp. 613-620, 2007.
92. H. Calkins, S. Y. Ho, J. Angel Cabrera, P. Della Bella, J. Farré, J. Kautzner and P. J. Tchou, "Anatomy of the Left Atrium and Pulmonary Veins," *Atrial Fibrillation Ablation: The State of the Art Based on the Venicechart International Consensus Document*, pp. 1-10, 2008.
93. B. L. McComb, R. F. Munden, F. Duan, A. A. Jain, C. Tuite and C. Chiles, "Normative reference values of thoracic aortic diameter in American College of Radiology Imaging Network (ACRIN 6654) arm of National Lung Screening Trial," *Clinical Imaging*, vol. 40, no. 5, pp. 936-943, 9 2016.
94. B. Mensel, J.-P. Kühn, T. Schneider, A. Quadrat and K. Hegenscheid, "Mean Thoracic Aortic Wall Thickness Determination by Cine MRI with Steady-State Free Precession: Validation with Dark Blood Imaging," *Academic Radiology*, vol. 20, no. 8, pp. 1004- 1008, 1 8 2013.
95. F. Xia, J. Mao, J. Ding and H. Yang, "Observation of normal appearance and wall thickness of esophagus on CT images," *European Journal of Radiology*, vol. 72, no. 3, pp. 406-411, 12 2009.

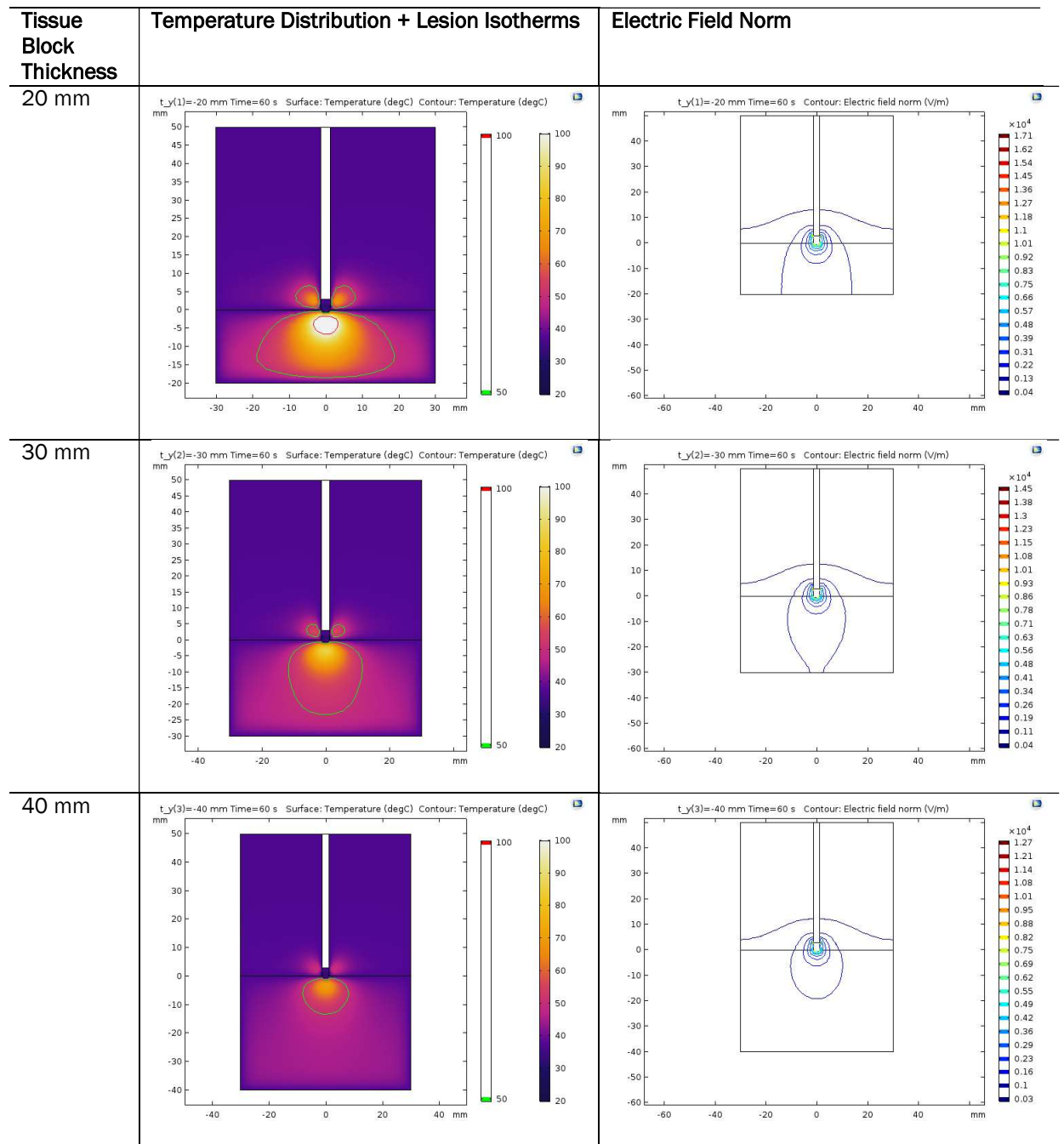
96. G. Pontone, D. Andreini, E. Bertella, M. Petullà, E. Russo, E. Innocenti, S. Mushtaq, P. Gripari, M. Loguercio, C. Segurini, A. Baggiano, E. Conte, V. Beltrama, A. Annoni, A. Formenti, A. I. Guaricci, M. Casella, G. Fassini, M. Giovannardi, F. Veglia, C. Tondo and M. Pepi, "Comparison of cardiac computed tomography versus cardiac magnetic resonance for characterization of left atrium anatomy before radiofrequency catheter ablation of atrial fibrillation," *International Journal of Cardiology*, vol. 179, pp. 114- 121, 2015.
97. W. Wei, J.-B. Ge, Y. Zou, L. Lin, Y. Cai, X.-B. Liu and W.-Q. Zhu, "Anatomical characteristics of pulmonary veins for the prediction of postoperative recurrence after radiofrequency catheter ablation of atrial fibrillation.," *PloS one*, vol. 9, no. 4, p. e93817, 2014.
98. S. Ispas, C. Dina, I. Bulbuc, D. Iliescu and P. Bordei, "Morphological aspects of the pulmonary veins," *ARS Medica Tomitana*, vol. 20, no. 1, pp. 50-56, 2014.
99. G. Dwivedi, G. Mahadevan, D. Jimenez, M. Frenneaux and R. P. Steeds, "Reference values for mitral and tricuspid annular dimensions using two-dimensional echocardiography.," *Echo research and practice*, vol. 1, no. 2, pp. 43-50, 1 12 2014.
100. H. G. Klues, M. A. Proschan, A. L. Dollar, P. Spirito, W. C. Roberts and B. J. Maron, "Echocardiographic assessment of mitral valve size in obstructive hypertrophic cardiomyopathy: Anatomic validation from mitral valve specimen," *Circulation*, vol. 88, no. 2, pp. 548-555, 1993.
101. F. A. Duck, "Thermal Properties of Tissue," in *Physical Properties of Tissues*, 1990, pp. 12-46.

102. C. Gabriel, A. Peyman and E. H. Grant, "Electrical conductivity of tissue at frequencies below 1 MHz," *Physics in Medicine and Biology*, vol. 54, pp. 4863-4878, 2009.
103. S. Gabriel, R. W. Lau and C. Gabriel, "The dielectric properties of biological tissues: III. Parametric models for the dielectric spectrum of tissues," 1996.
104. A. M. Qadri, N. J. Y. Chia and E. H. Ooi, "Effects of saline volume on lesion formation during saline-infused radiofrequency ablation," *Applied Mathematical Modeling*, pp. 360-371, 2017.
105. F. A. Duck, "Electrical Properties of Tissue," in *Physical Properties of Tissues*, 1990, pp. 167-217.
106. D. Kumar, S. Singh and K. N. Rai, "Analysis of classical Fourier, SPL and DPL heat transfer model in biological tissues in presence of metabolic and external heat source," *Heat and Mass Transfer*, vol. 52, no. 6, pp. 1089-1107, 15 6 2016.
107. R. Rosencranz, "Clinical Laboratory Measurement of Serum, Plasma, and Blood Viscosity," 2006.
108. K. N. Rai and S. K. Rai, "Effect of metabolic heat generation and blood perfusion on the heat transfer in the tissues with a blood vessel," 1999.
109. J. Moreno, J. G. Quintanilla, R. Molina-Morua, M. J. Garcia-Torrent, M. J. AnguloHernandez, C. Curiel-Llamazares, J. Ramiro-Bargueno, P. Gonzalez, A. J. Caamano, N. Perez-Castellano, J. Rojo-Alvarez, J. Perez-Villacastin and C. Macaya, "Morphological and Thermodynamic Comparison of Lesions Created by 4 Open-Irrigated Catheters in 2 Experimental Models," *Journal of Cardiovascular Electrophysiology*, vol. 25, no. 12, pp. 1391-1399, December 2014.

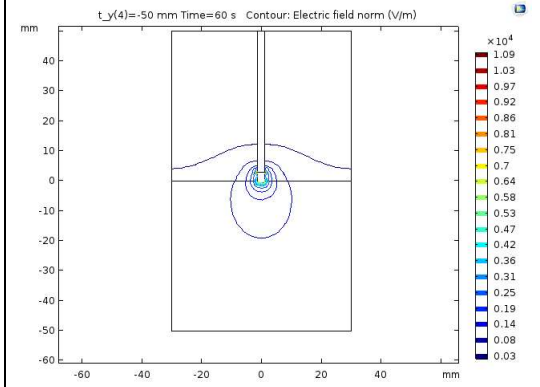
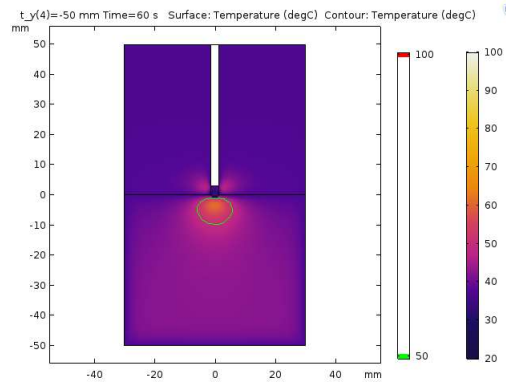
110. D. Dillon-Murphy, D. Marlevi, B. Ruijsink, A. Qureshi, H. Chubb, E. Kerfoot, M. D. O'Neill, D. Nordsletten, O. Aslanidi and A. de Vecchi, "Modeling Left Atrial Flow, Energy, Blood Heating Distribution in Response to Catheter Ablation Therapy," *Frontiers in Physiology*, vol. 9, 14 12 2018.
111. A. Fyrenius, L. Wigstrom, T. Ebbers, M. Karlsson, J. Engvall and A. F. Bolger, "Three dimensional flow in the human left atrium," *Heart*, vol. 86, pp. 448-455, 2001.
112. P. Liu, J. Liu and H. Duan, "Thermal modelling for endocardiac radiofrequency ablation: comparison of hyperbolic bioheat equation and Pennes bioheat equation with finite element method"
113. M. K. JAIN, G. TOMASSONI, R. E. RILEY and P. D. WOLF, "Effect of Skin Electrode Location on Radiofrequency Ablation Lesions: An In Vivo and a Three-Dimensional Finite Element Study," *Journal of Cardiovascular Electrophysiology*, vol. 9, no. 12, pp. 1325-1335, 1 12 1998.

APPENDICES

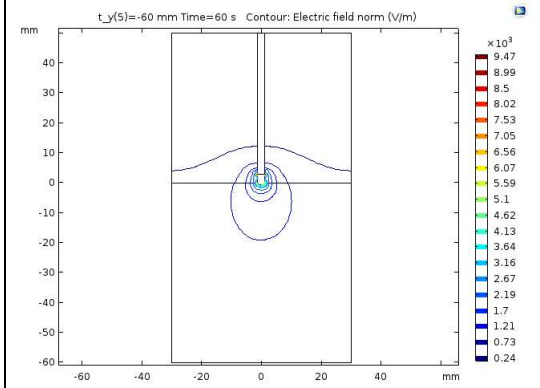
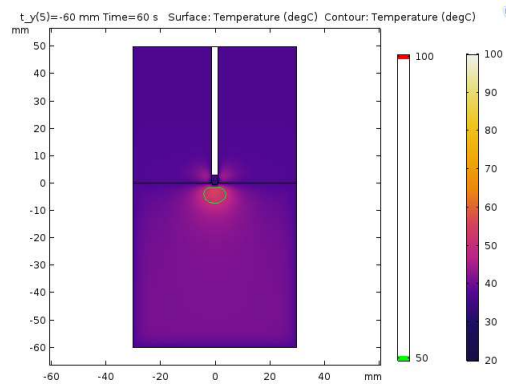
Appendix A. Convergence Testing on Tissue Depth of Simplified Verification Models.



50 mm



60 mm



Appendix B. Fusion 360 Left Atrial Model

Several computer aided modeling platforms were trialed to generate the left atrial geometry needed for this study. Initial modeling was performed in Fusion 360®, a modeling environment from the makers of AutoCAD® and other digital rendering software. Fusion 360® creates geometries with classic CAD functions, but also has a GUI and tools to sculpt organic geometries. Using anatomical illustrations and CT data stacks, rough initial sketches were produced of different views of the left atria and adjacent anatomy. To better visualize the CT stack, the 3D Viewer plugin of ImageJ was utilized to provide a rough rendering and greater positional information.

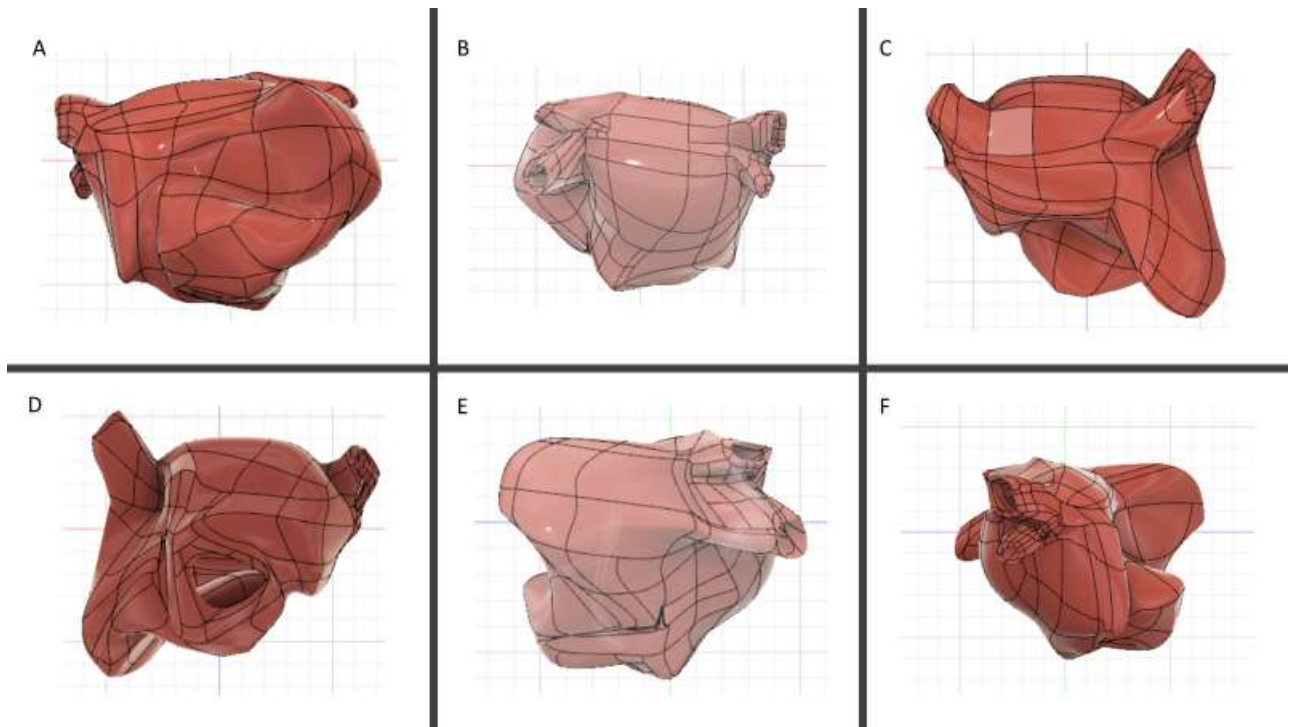


Figure 41. Fusion 360 Left Atrial Model.

A) Anterior view, B) posterior view, C) superior view, D) inferior view, E) left view, F) right view of left atrium. Critical aspects include: pulmonary veins, mitral valve annulus, and left atrial appendage.

To sculpt the left atrium, an obloid rectangle was manually molded in repositioning nodes, boundaries, and faces to resemble the left atrial anatomy. This model included the septum, atrial vestibule, left atrial appendage, pulmonary veins, and the mitral valve opening.

A key advantage of this model was anatomical fidelity. The major issues with this modeling format were

- (1) poor reproducibility,
- (2) no customizability of specific regions/dimensions,
- (3) high computational burden, and
- (4) exceedingly long construction times by the modeler.

Appendix C. COMSOL Multiphysics® CAD Left Atrial Model.

The next attempt was a simplified version of the left atrium as modeled with the shape “primitives” and operations of COMSOL’s native modeling environment. For this model, hollow cylinders were attached to a hollow flattened hemisphere to represent the pulmonary veins and atria body. A mitral valve opening was formed by differencing away an elliptical cylinder from the posterior aspect of the atria body. This entire geometry was then embedded in a block to create domains within the enclosed boundaries. Everything beyond the atrial walls was considered a generic external tissue volume, whereas everything within the atria was designated as blood volume.

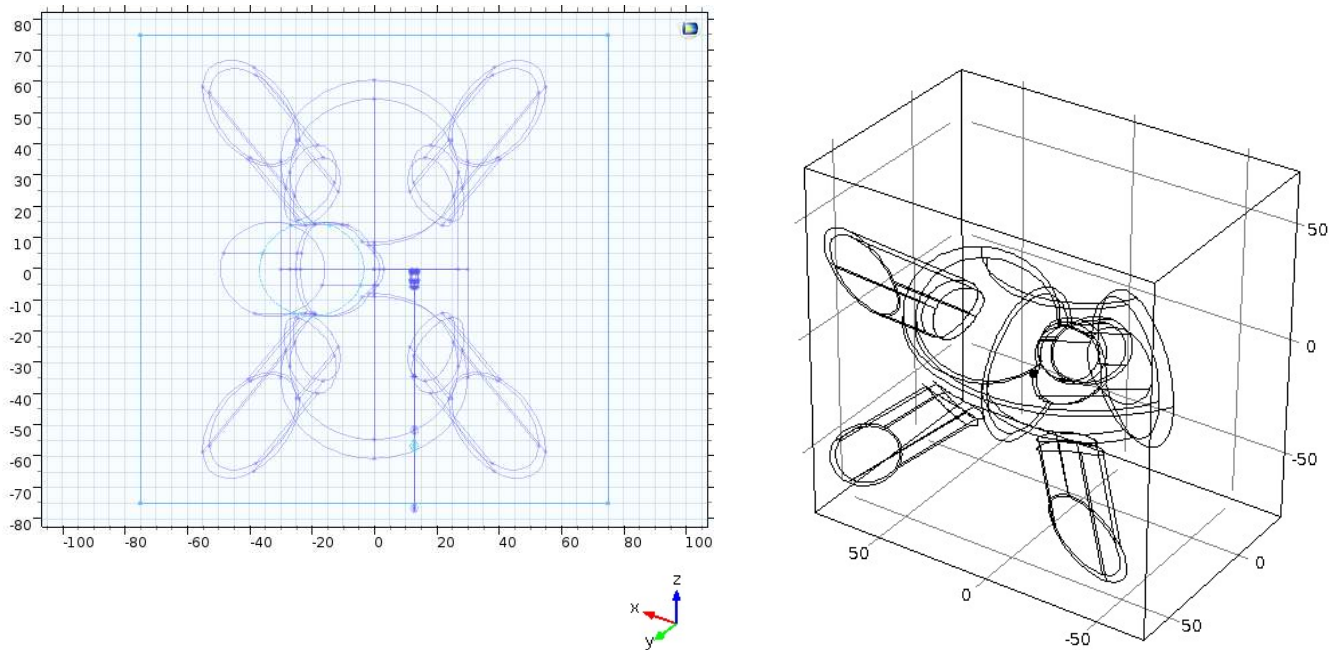


Figure 42. “COMSOL CAD” Left Atrial Model.

A) Wireframe drawing of head-on mitral valve view. B) 3D wireframe model of the left atria including collateral tissue block and defined blood volume. All dimensions in mm.

This geometry was exceedingly difficult to mesh due to the sharp joins at of the pulmonary veins with the atria, as highlighted in the image below [Figure 43Figure].

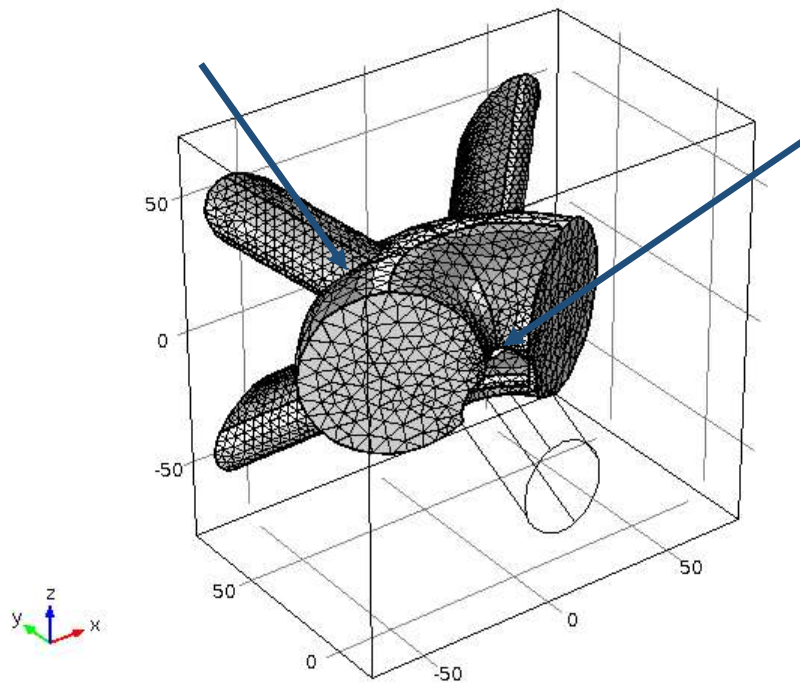


Figure 43. Mesh of COMSOL CAD Left Atrial Model.

Sharp interfaces and highly curved geometry led to meshing problems (arrows) that could not be resolved with finer meshing. Mesh implemented had tetrahedral shaped elements, with dimensions pre-defined by COMSOL under the “Extremely Coarse” element parameter settings.

Appendix D. Early SolidWorks® Left Atrial Models

Shown below are a series of initial atrial models. The main atrial body was created by creating lofts between sketched profiles, then shelling the resulting solid. Pulmonary veins were added after. The main reason these models were not used for the final assembly was that they could not be imported into COMSOL Multiphysics® without an excessive degree of geometry errors. Regardless of filetype, those lofted boundaries which made up the exterior of the main atrial boundary were treated as discontinuous or intersecting surfaces by COMSOL. While efforts were made to address those geometry errors, it was determined that reworking the design in SolidWorks® was easier and a more effective use of time than trying to resolve the errors with COMSOL's limited solid modeling tools.

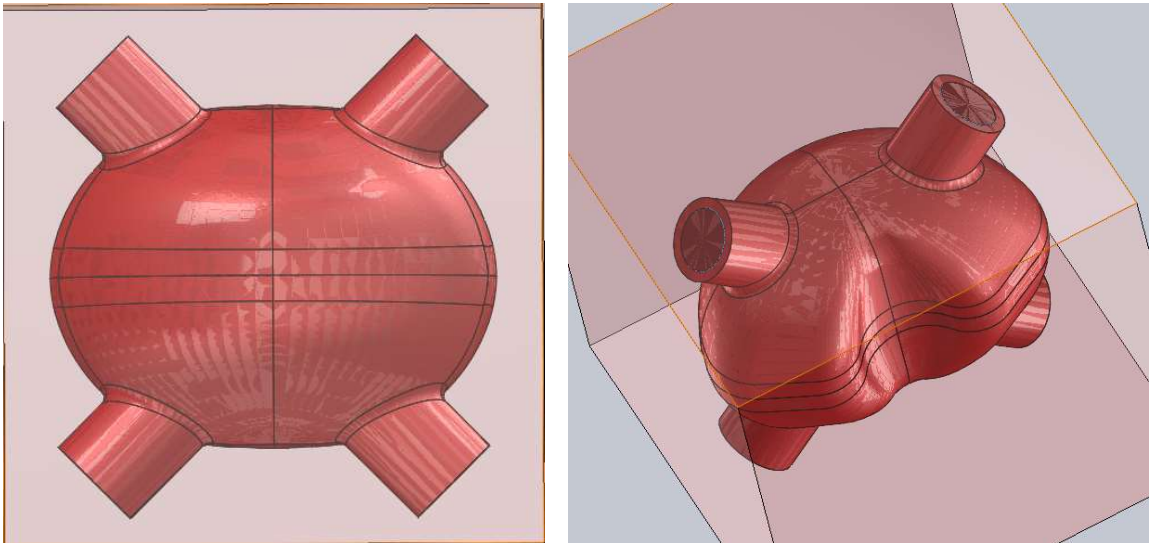


Figure 44. Early Atrial Models with 2 Planes of Symmetry.

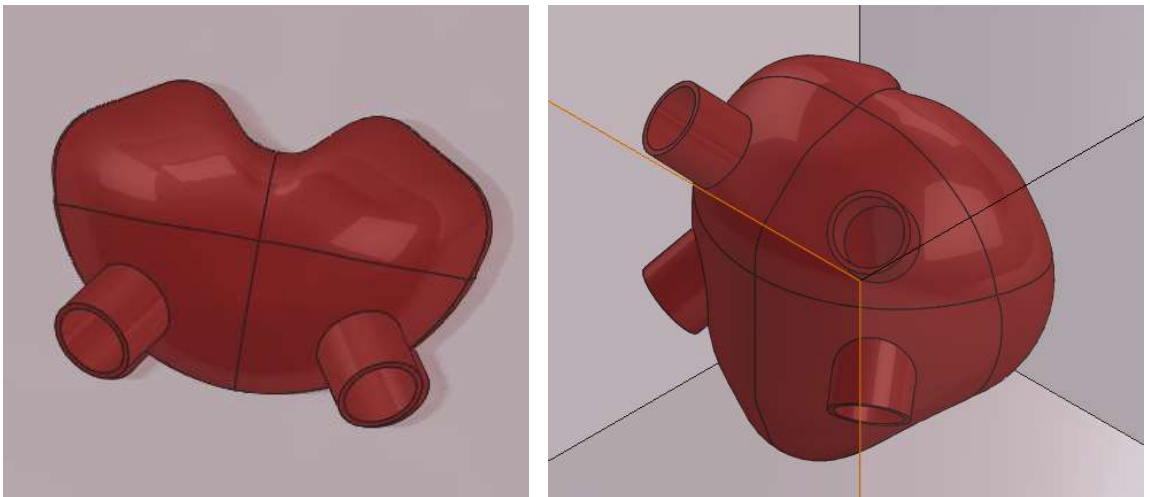


Figure 45. Early SolidWorks Model with 1 Plane of Symmetry.

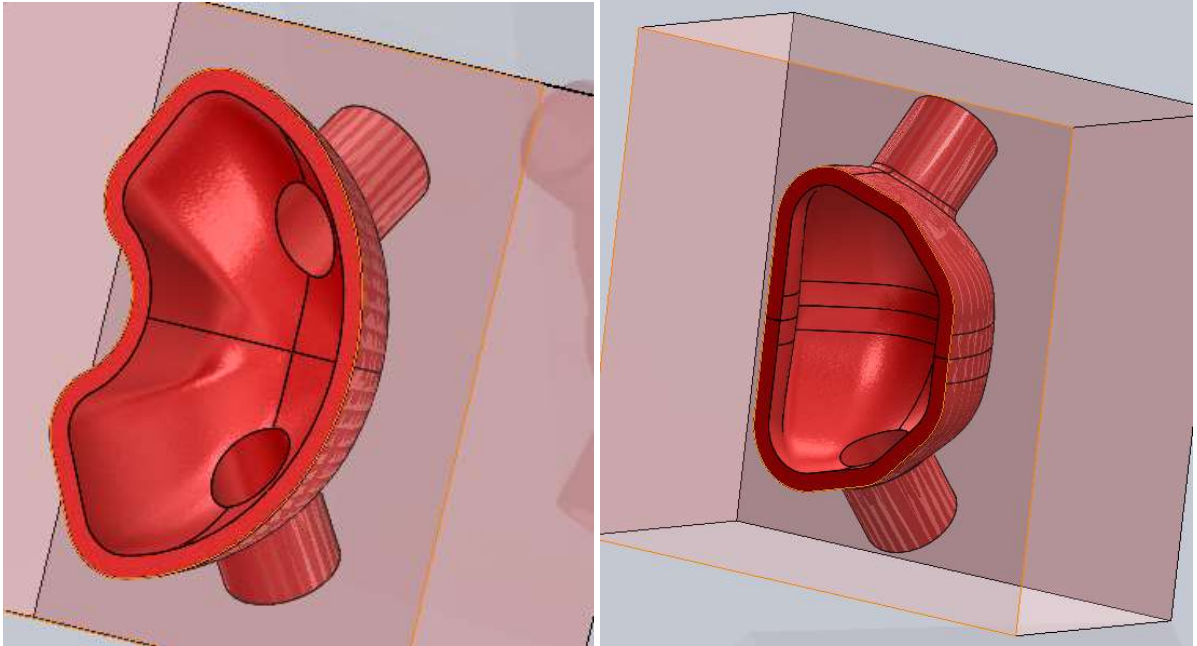


Figure 46. Interior View of Early Atrial Models with 2 Planes of Symmetry.

Appendix E. Final Left Atrial SolidWorks® Model

The following images contain critical dimensions and several views of the left atrial assembly developed in SolidWorks®.

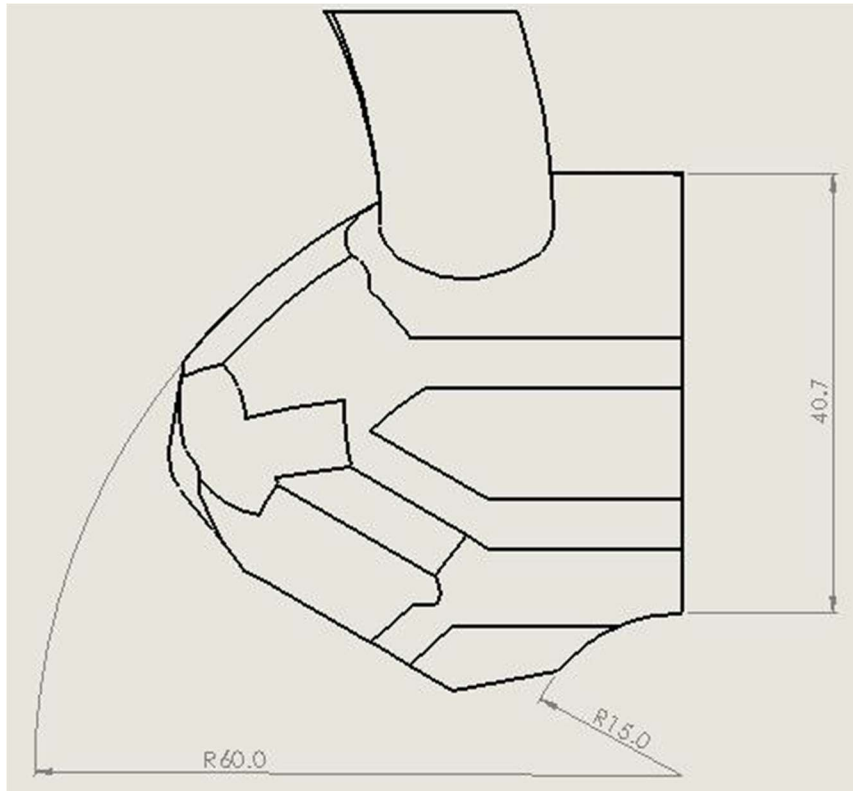


Figure 47. Dimensioned Top View of Left Atrial Model.

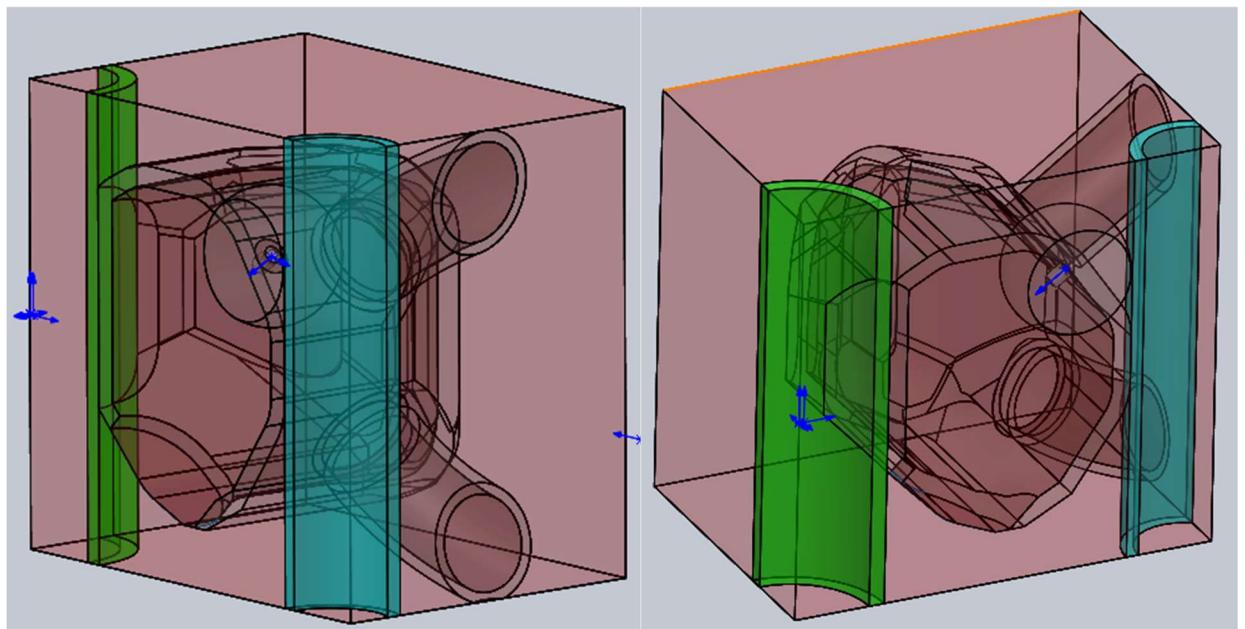


Figure 48. Alternate Views of Left Atrial Assembly.

Views taken from the left posterior perspective (left) and left anterior perspective (right).

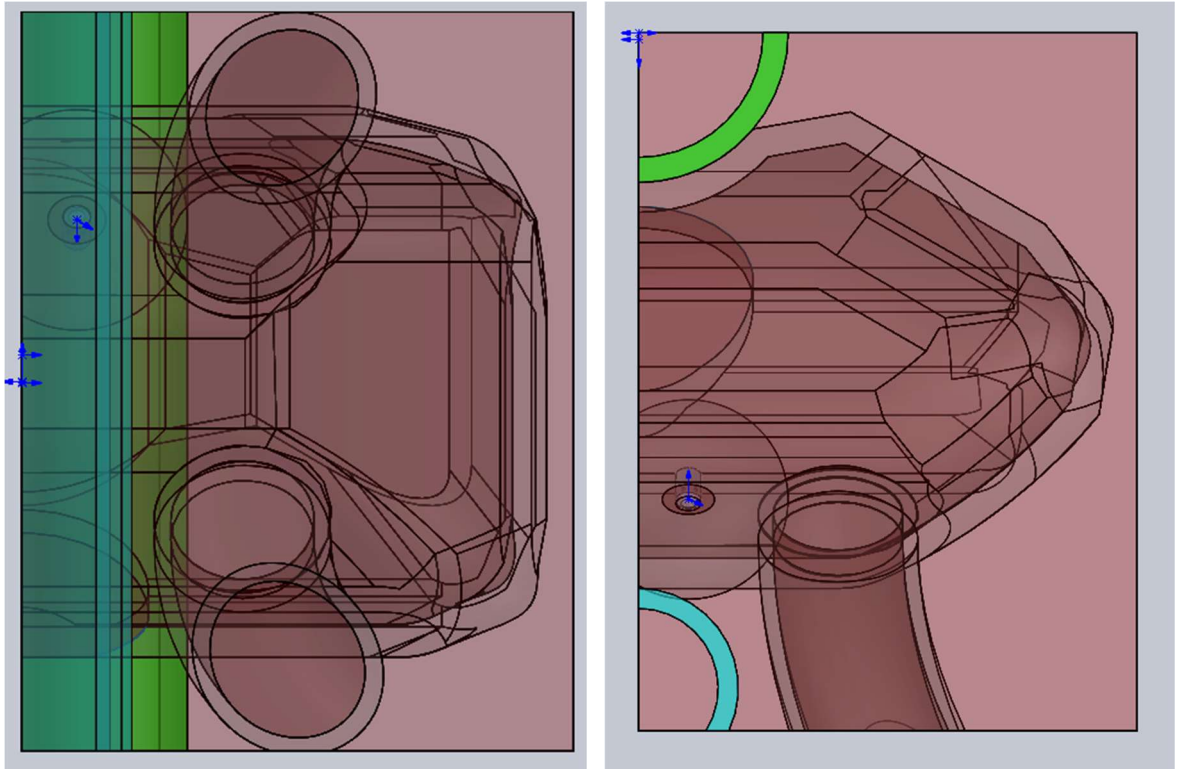


Figure 49. Posterior (left) and Inferior (right) Views of Left Atrial Assembly

Appendix F. Protocol for Pre-processing and Transfer of Complex Geometric Models from SolidWorks to COMSOL.

Catheter Design Addition

1. If adding a catheter tip design to the model, import it into the assembly and position first using the Mate tools. It will be a lot easier to do this in SolidWorks than in COMSOL.

Defeaturing and Geometry Checks

1. As much as possible, merge small faces to form larger curved surfaces using the “Delete Faces” tool in SolidWorks.
2. Run Geometry Analysis to identify any short edges, knife angles, etc. are in each part. Resolve these in SolidWorks.

Exporting the Assembly from SolidWorks®

1. Once the assembly is ready to be moved over to COMSOL, export it as a Parasolid binary (.x_b) file type. (Note: The filetypes that seemed to have the greatest chances of transfer success are .x_b, .x_t, .stl).

Importing the Assembly to COMSOL

1. Use the “Import” tool to import in the assembly files. Specify appropriate dimension scale in “Geometry” model tree settings.

Building the Mesh

1. If error messages about thin element sizes come up during the message process, the merge tools of the “Virtual Operations” toolbar can be particularly useful.

Appendix G. Material Domain Definitions in Left Atrial Model.

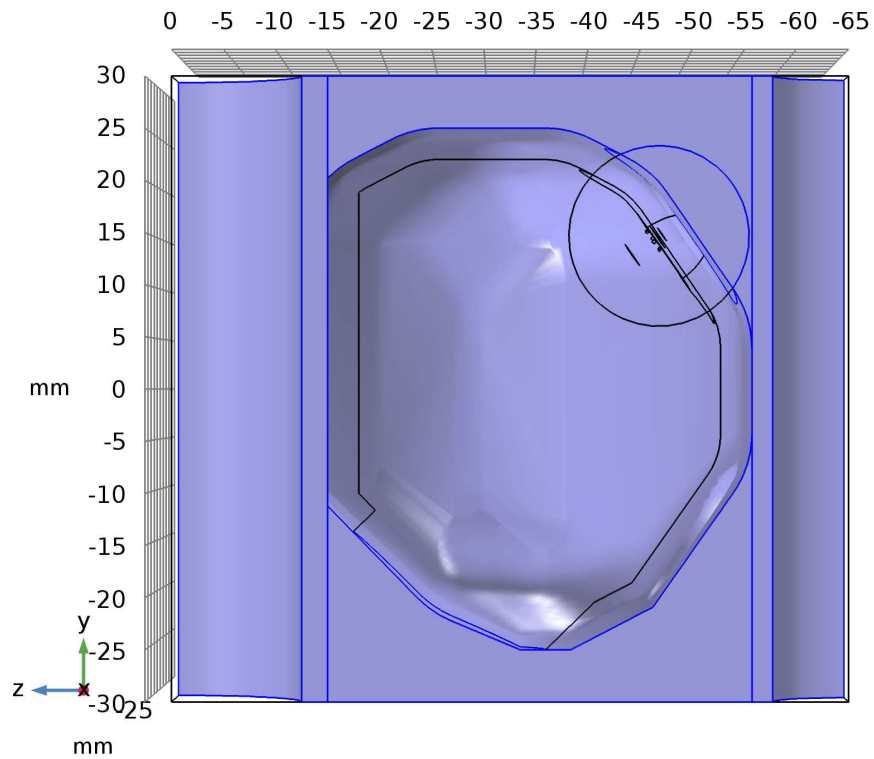


Figure 50. "Generic Tissue" Domain in Full Model.

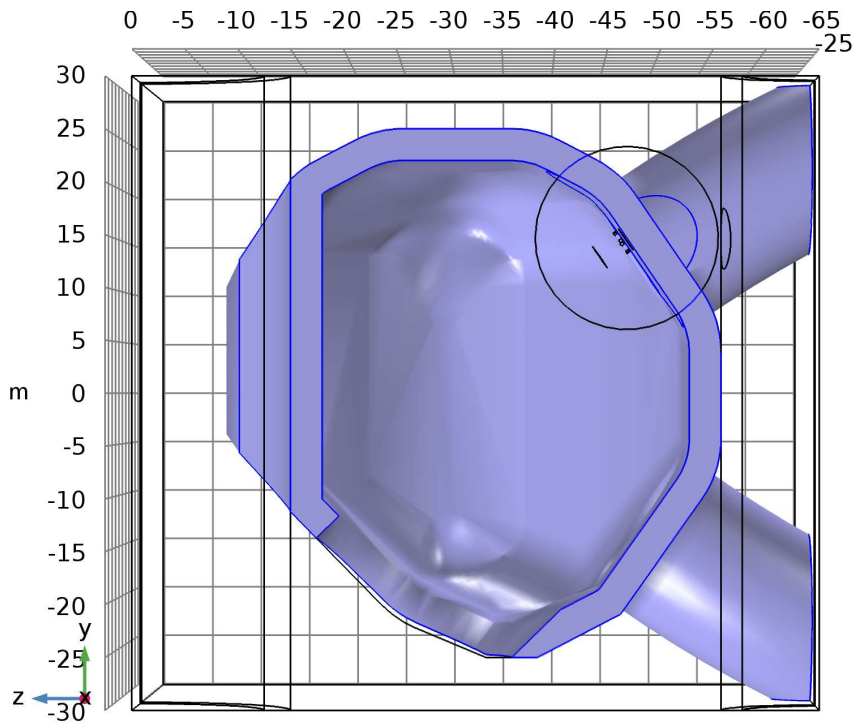


Figure 51. Myocardium Domain in Full Model.

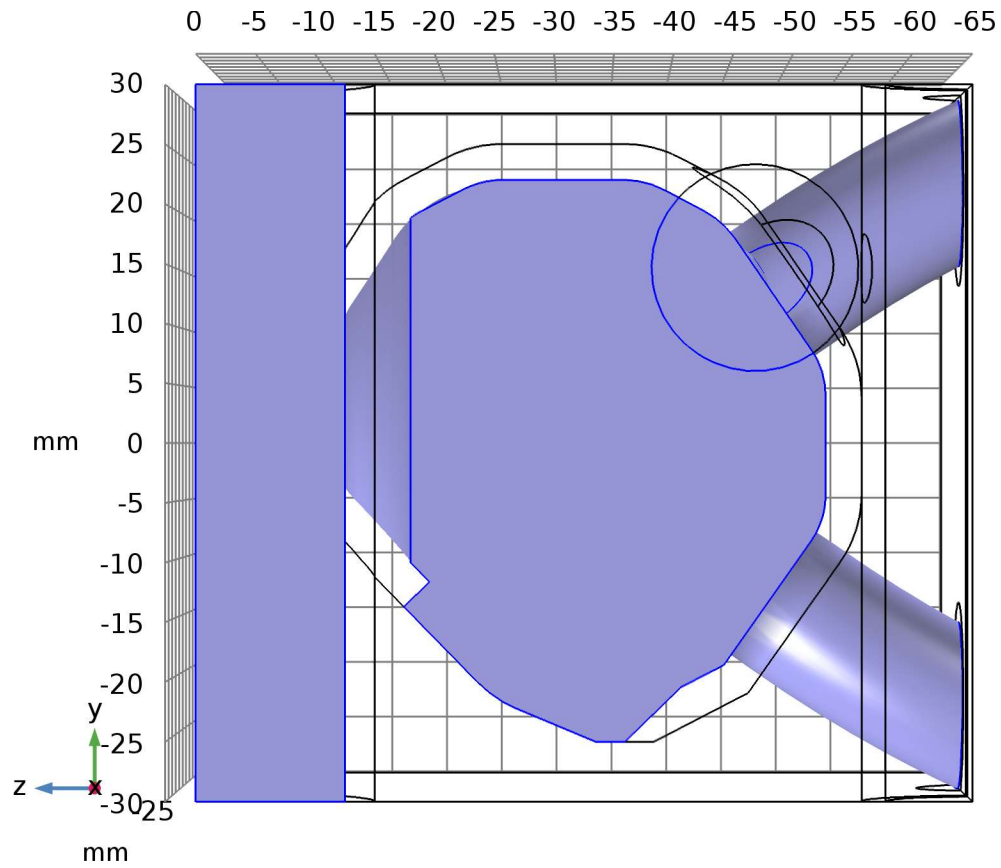


Figure 52. Blood Domains in Full Model.

To simplify the solution, the aortal blood volume was removed as a domain from the simulations, and a 37 °C boundary condition was placed on the interior surface of the aorta.

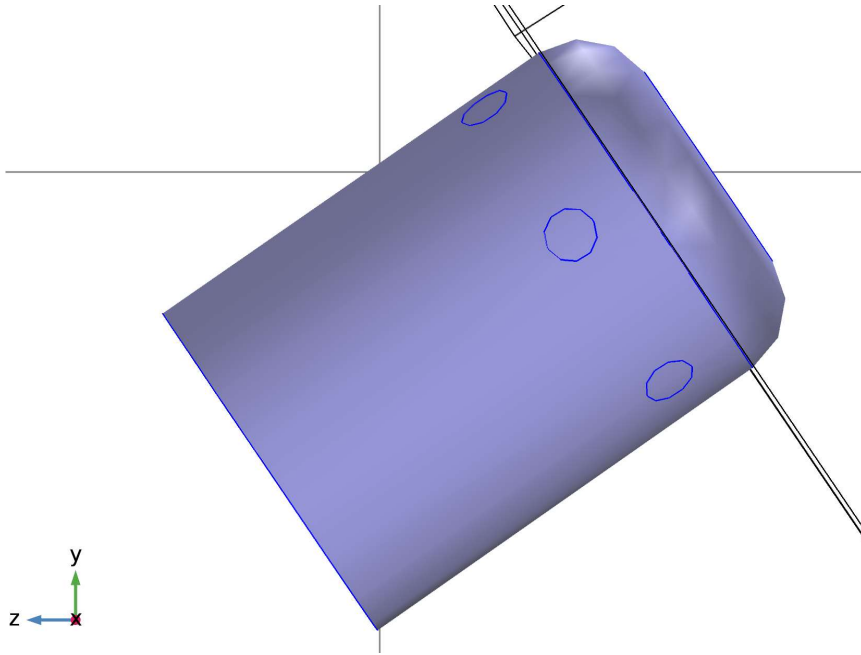


Figure 53. Catheter Tip in COMSOL Model

Appendix H. Physics Verification Studies: Effect of Blood Flow, Saline Irrigation, and Temperature-Dependent Properties

Effect of Blood Flow on Lesion Morphology

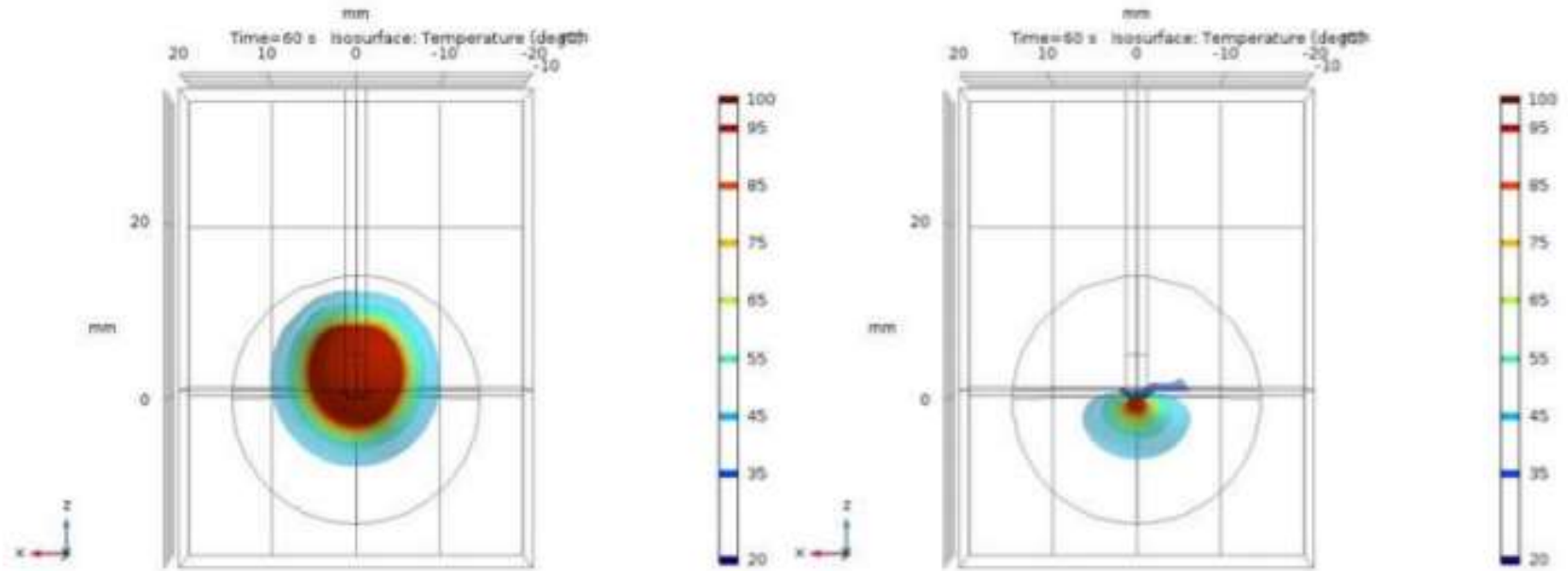


Figure 54. Lesion Morphology in Simulations with and without Blood Flow.

Effect of Irrigation on Lesion Production

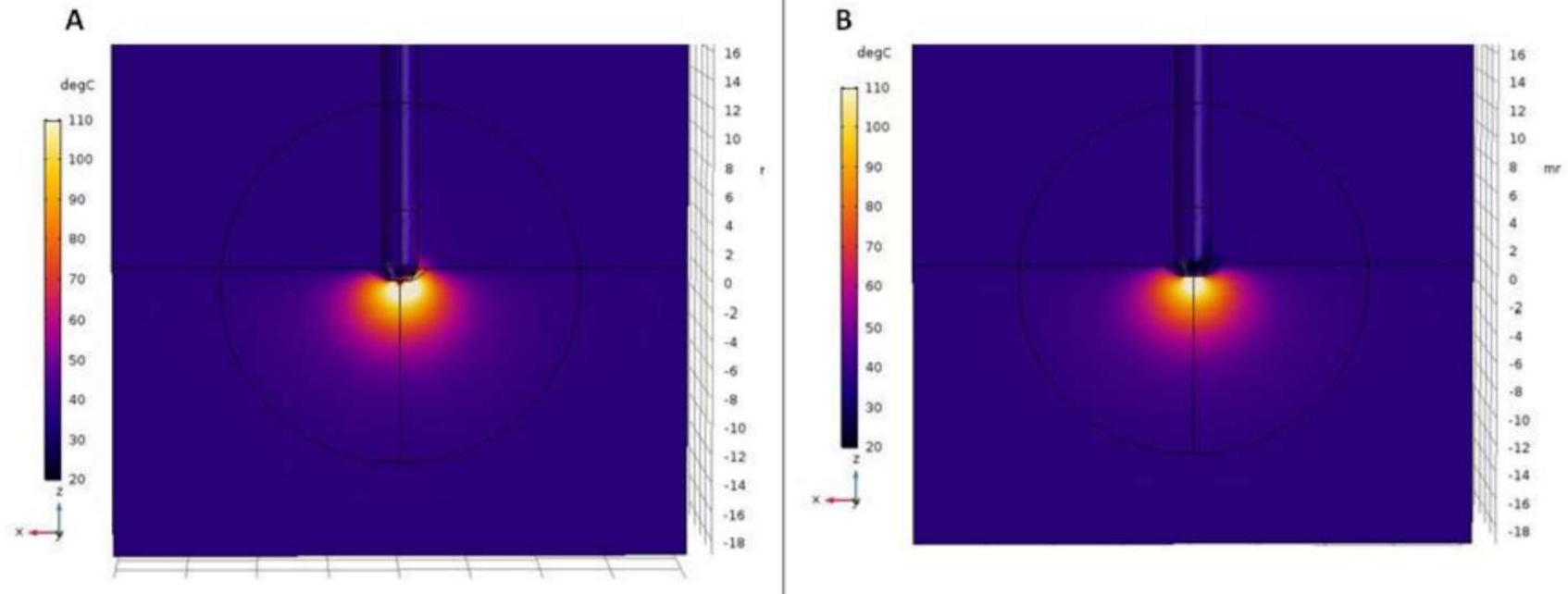


Figure 55. Temperature Distribution after 60s of 50V Constant Voltage Ablation Without Irrigation (A), and With Irrigation of 30 mL/min (B).

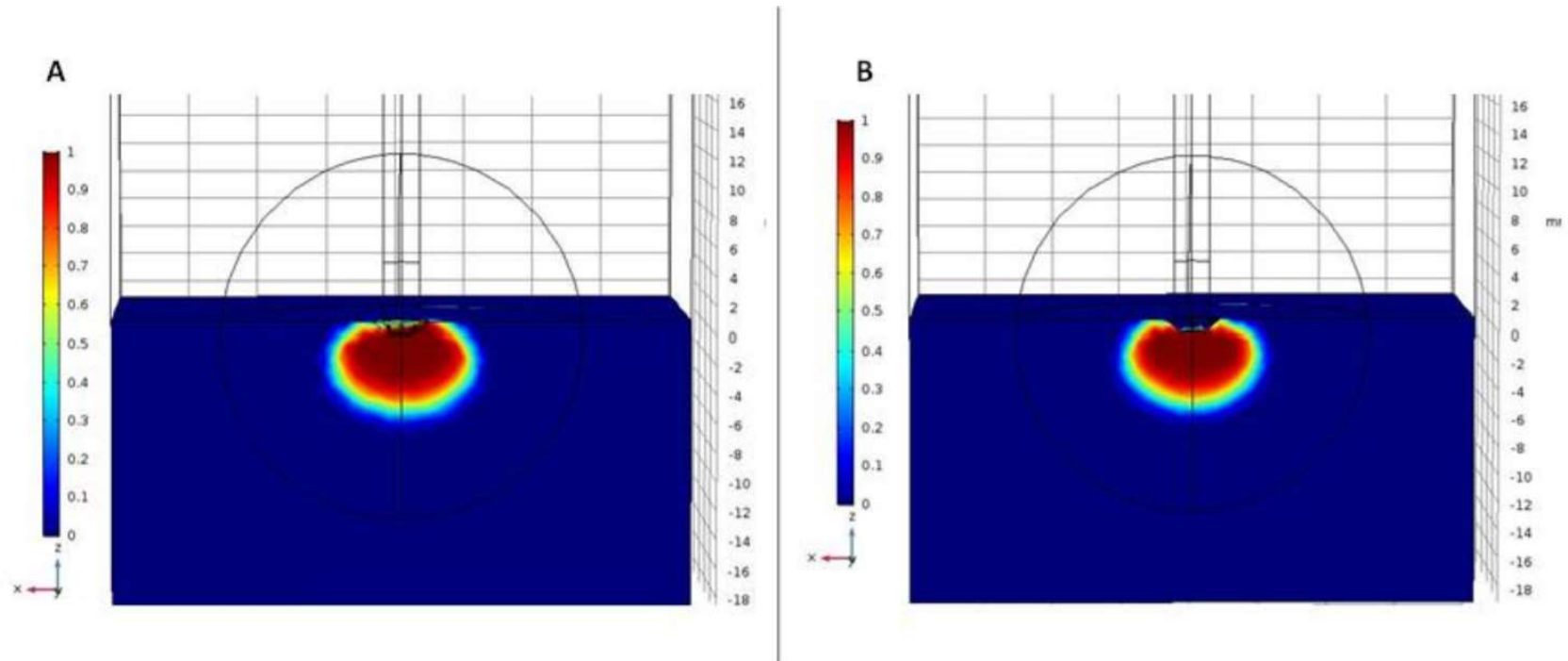


Figure 56. Damage Distribution after 60s of 50V Constant Voltage Ablation Without Irrigation (A), and With Irrigation of 30 mL/min (B).

Static Material Properties vs Temperature Dependent Material Properties

As expected, implementation of rudimentary temperature dependence of material properties produced a smaller lesion size than the static case, as depicted in [Figure 57]. The maximum depth and diameter of the temperature dependent lesion case was 5.6 mm and 8.0 mm, respectively. On the other hand, the static material properties predicted a lesion with a max depth of 6.9 mm, and a max diameter of 11.1 mm.

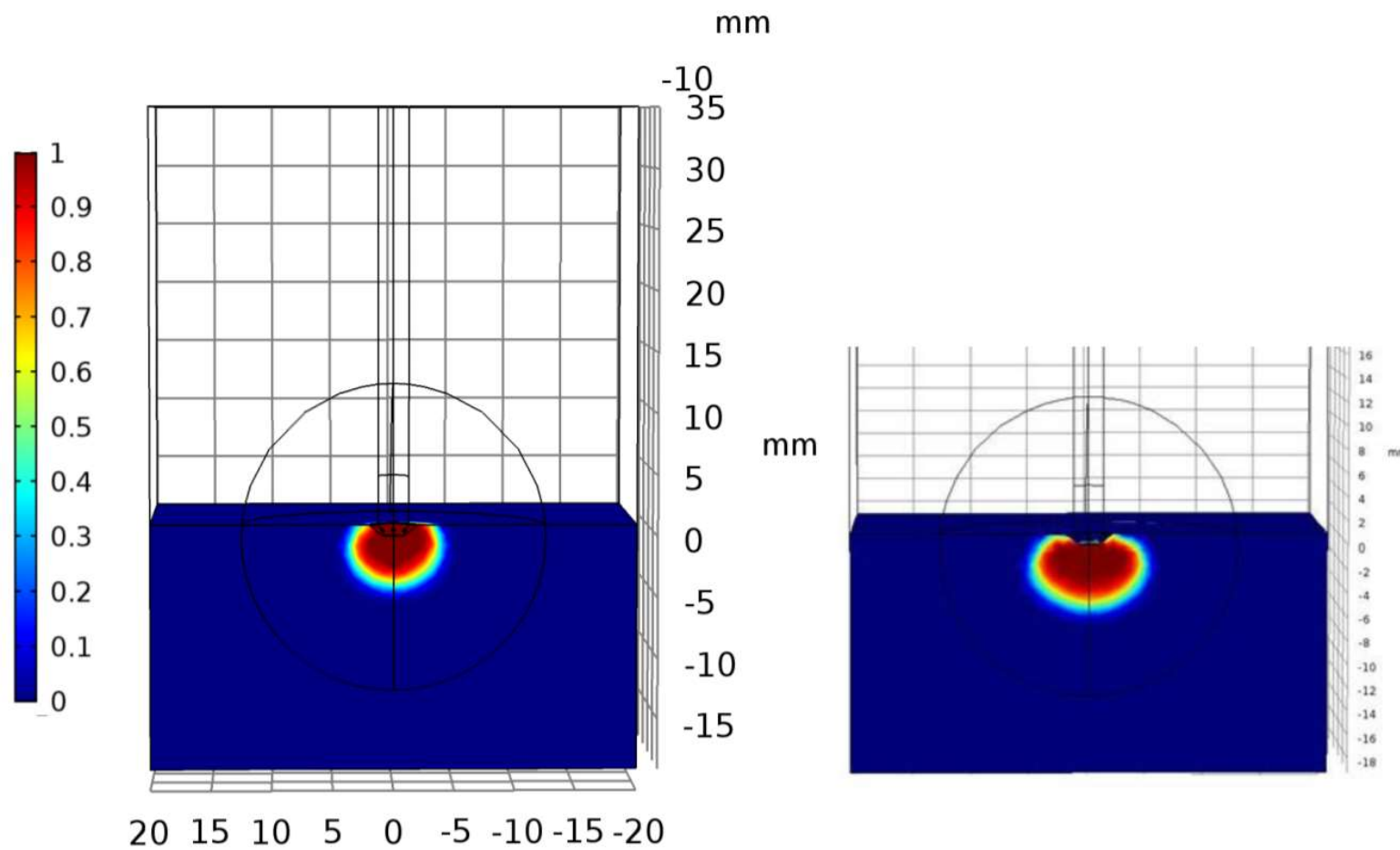


Figure 57. Effect of Temperature Dependent Properties on Lesion Production.
Damage plotted to show extent of lesion propagation.

Appendix I. Preliminary Flow Studies in the Left Atrial Model.

While realistic flow patterns were not deemed critical to model success for this thesis, selected velocity measurements were used to check the suitability of the PV inflow condition. Average blood velocity and transmitral flow velocity were sampled using domain and boundary averaging methods, respectively. These values were compared against blood velocities of patients with AF determined by Doppler electrocardiography, the results of which are summarized in the table below [Table 10].

Table 10. Simulated Blood Flow vs Clinical Velocities from Doppler Echocardiography.

Parameter	Literature Value	Integrated Transmitral Flow Value	Large Model % Difference
Blood Flow Velocity (Entire R-R Interval)	0.13 ± 0.02 m/s	0.082 m/s	-36.9%
Transmitral Flow Velocity	0.30 ± 0.10 m/s	0.211 m/s	-29.8%

Based on the sampled velocity values, it appeared that the 0.2 m/s velocity condition set on the PV inlets was too low to achieve adequate overall flow velocity.

Initial modeling with the 0.20 m/s inflow condition on the pulmonary veins produced velocities that were not consistent with those observed in clinic for AF patients. To address this, a parametric study was performed on PV inflow velocity with values ranging from 0.2 – 0.8 m/s. When compared with the target average velocity and transmitral flow, 0.3 m/s generated percent differences of 8.5% and 1.2% respectively [Table 11].

Table 11. Parametric Study on Inlet Velocities to Match Clinical Data for AF Patients.

Values of transmitral and average left atrial blood velocities determined by Doppler echocardiography [105]

PV Inlet Velocity [m/s]	Transmitral Flow [m/s]	Target, Transmitral Velocity	% Difference from Target	Average LA Velocity, [m/s]	Target, Avg LA Velocity	% Difference from Target
0.2	0.21	0.30	-29.8%	0.08	0.13	-36.9%
0.3	0.30	0.30	1.2%	0.12	0.13	-8.5%
0.4	0.39	0.30	31.1%	0.16	0.13	19.4%
0.5	0.48	0.30	60.5%	0.19	0.13	47.3%
0.6	0.57	0.30	89.5%	0.23	0.13	75.1%
0.7	0.65	0.30	118.0%	0.26	0.13	102.8%
0.8	0.74	0.30	146.2%	0.30	0.13	130.6%

But while the overall velocity profiles were closer to physiologic values with this modification, the lesion dimensions were at least 15% smaller than the previous flow case [Table 8]. This decrease in lesion size with higher flow rates was expected, with faster flow corresponding with greater convective cooling.

Table 12. Lesion Dimension Comparison with Different PV Velocities.

All velocities reported in [m/s].

	Lesion Max Depth [mm]	Lesion Max Width [mm]
Moreno et al	9.3 ± 1.4	10.3 ± 1.5
0.20 m/s	1.040	3.993
0.30 m/s	0.879	3.042

More importantly, none of these flow cases resulted lesion dimensions commensurate with the experimental dimensions.

Appendix J. Exploratory Characterization of Activation Energy Value Effect on Damage Quantification.

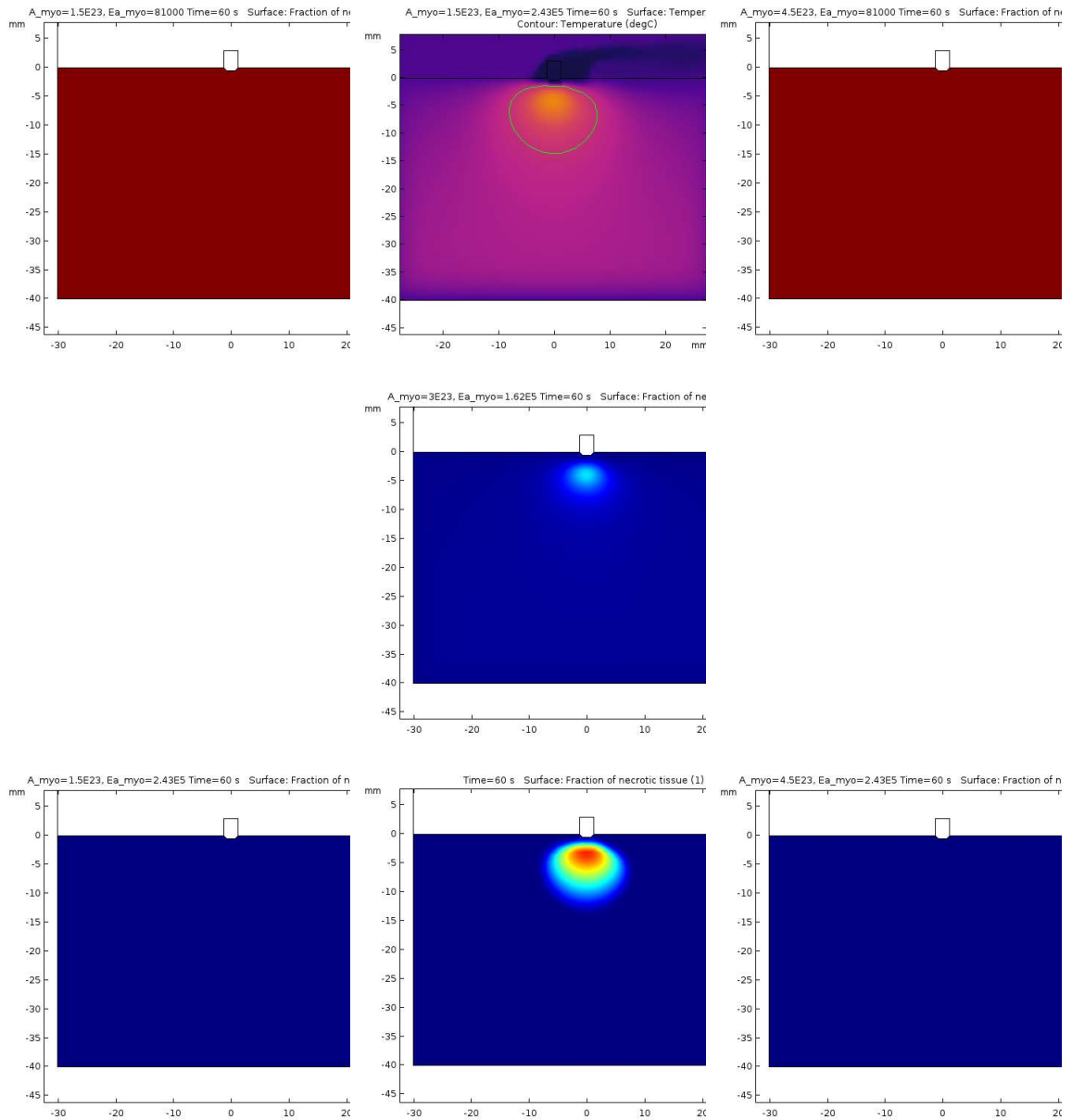


Figure 58. Damage Evaluation Comparison, with Parametric Sweep of Activation Energy.